Title: Average miniature post-synaptic potential size is inversely proportional to membrane capacitance across neocortical pyramidal neurons of different sizes

Author Names and Affiliations: Martynas Dervinis[1], Guy Major[1]

[1]: Cardiff University, Cardiff, Wales, CF10 3AT, UK

Corresponding author email address: martynas.dervinis@gmail.com

Number of pages: 56

Number of figures: 12

Abstract: 237

Body text excluding Materials and Methods: 5022 (1180 + 3842)

Conflict of interest statement: The authors declare no competing financial interests.

Acknowledgements: Cardiff University (GM, MD), The Medical Research Council of the UK (MD PhD scholarship). Neural activity simulations and minis' distribution fitting were performed on the Cardiff School of Biosciences' Biocomputing Hub HPC/Cloud infrastructure.

Abstract

In chemical synapses of the central nervous system (CNS), information is transmitted via the presynaptic release of a vesicle (or 'quantum') of neurotransmitter, which elicits a postsynaptic electrical response with an amplitude termed the 'quantal size'. Measuring amplitudes of miniature postsynaptic currents (mPSCs) or potentials (mPSPs) at the cell soma is generally thought to offer a technically straightforward way to estimate quantal sizes, as each of these miniature responses (or minis) is generally thought to be elicited by the spontaneous release of a single neurotransmitter vesicle. However, in large highly-branched neurons, a somatically recorded mini is typically massively attenuated compared with at its input site, and a significant fraction are indistinguishable from (or cancelled out by) background noise fluctuations. Here, using a new software package (also) called 'minis', we describe a novel quantal analysis method that estimates the 'electrical size' of the synapse by comparing events detected in somatic recordings from the same neuron of (a) *real* minis and (b) background noise (with minis blocked pharmacologically) with *simulated* minis added by a genetic algorithm. The estimated minis' distributions reveal a striking inverse dependence of mean excitatory mPSP amplitude on total cell membrane capacitance (proportional to cell size, or more exactly, extracellular membrane surface area) suggesting that, in rats at least, the average charge injected by single excitatory synapses (ca. 30 fC) is conserved across neocortical pyramidal neurons of very different sizes (across a more than three-fold range).

41 # Abbreviations

42 ABF – Axon Binary File

43 aCSF – artificial cerebrospinal fluid

44 AMPA – α-amino-3-hydroxy-5-methyl-4-isoxazolepropionic acid

45 AMPAR – α-amino-3-hydroxy-5-methyl-4-isoxazolepropionic acid receptor

46 ANN – artificial neural network

47 AP – action potential

48 CGP55845A – selective competitive antagonist of $GABA_B$ receptors (thus slow K^+ dependent IPSPs)

49 CPP – (*RS*)-3-(2-carboxypiperazin-4-yl)-propyl-1-phosphonic acid (potent selective competitive
50 glutamate NMDA receptor antagonist, thus depolarization-dependent, slow component of EPSPs)

51 EPSC – excitatory postsynaptic current

52 EPSP – excitatory postsynaptic potential

53 GA – genetic algorithm

54 GABA – gamma-aminobutyric acid (inhibitory neurotransmitter)

55 IC50 – concentration blocking half of the receptors

56 IPSC – inhibitory post-synaptic current

57 IPSP – inhibitory post-synaptic potential

58 MAD – maximum absolute deviation

59 mEPSC– miniature excitatory post-synaptic current

60 mEPSP– miniature excitatory post-synaptic potential

61 mIPSP– miniature inhibitory post-synaptic potential

62 mPSC – miniature post-synaptic current

63 mPSP – miniature post-synaptic potential

64 NBQX – 2,3-dioxo-6-nitro-1,2,3,4-tetrahydrobenzo[*f*]quinoxaline-7-sulfonamide (potent selective

65 competitive antagonist of AMPA (and kainate) glutamate receptors, thus fast component of EPSPs)

66 NMDA – N-methyl-D-aspartate

67 NMDAR - N-methyl-D-aspartate receptor

68 R_{ser} – series resistance

69 SAD – sum of absolute deviations

70 SD – standard deviation

71 smEPSP – simulated mEPSP

72 SSD – sum of signed deviations

73 SSE – sum of squared errors

74 TTX – tetrodotoxin (potent selective competitive antagonist of Na^+ channels, thus action potentials)

75 V_m – transmembrane potential

76

Introduction

Synaptic transmission in the CNS occurs in 'quanta' (Forti et al., 1997; Hardingham et al., 2010; Isaacson and Walmsley, 1995; Jonas et al., 1993; Kraszewski and Grantyn, 1992; Kullmann and Nicoll, 1992; Kuno, 1964; Larkman et al., 1991; Sahara and Takahashi, 2001; Stern et al., 1992; Wall and Usowicz, 1998), usually thought to each correspond (for the most part at least) to the release of a single neurotransmitter vesicle (Heuser et al., 1979). The amplitude of the postsynaptic response to a quantum of transmitter, the quantal size, is a key parameter defining the efficacy of synaptic transmission (Katz, 1969; Vere-Jones, 1966) and, therefore, an important determinant of neural computation. For example, how many synapses, on average, does it take to fire a cell?

Quantal size measurements in the CNS are difficult, due to multi-synaptic contacts (multiple synapses per connection between a particular pair of neurons, and multiple release sites/postsynaptic densities/receptor 'rafts' for some synapses), limited accessibility, significant quantal variance (both within and between synapses of a given connection), temporal non-stationarity of synaptic properties (e.g. receptor desensitisation or internalisation, and depletion of glutamate from presynaptic vesicles), and low signal-to-noise ratios of somatic electrophysiological recordings of quantal events (Bekkers, 1994; Farsi et al., 2021; Korn and Faber, 1991). For these reasons classical quantal analysis as done at the neuromuscular junction often runs into problems in central synapses, where most of the minis do not 'stand out' from the noise. More recent methods such as noise deconvolution, Variance-Mean analysis, and optical quantal analysis have not fared much better (Biró et al., 2005; Clamann et al., 1991; Clements, 2003; Clements and Silver, 2000; Edwards et al., 1976; Enoki et al., 2009; Jack et al., 1981; Liu et al., 2022; Oertner et al., 2002; Peled and Isacoff, 2011; Redman, 1990; Reid and Clements, 1999; Silver, 2003; Yuste et al., 1999), or suffer from potential selection biases (e.g. paired recordings typically require cells close together whose

synapses may be a non-representative sub-population, differing from the overall population of synapses).

A complementary method of assessing synaptic function is to measure properties of mPSCs. Miniature PSC amplitude measurements are often taken as quantal size estimates across the population of active synapses onto a neuron, as the mPSC (under voltage clamp) or mPSP (under voltage recording) likely corresponds (in most cases) to the response to a spontaneous release of a single neurotransmitter vesicle (Brown et al., 1979; del Castillo and Katz, 1954; Fatt and Katz, 1952; Isaacson and Walmsley, 1995; Wall and Usowicz, 1998) and, therefore, if performed accurately, can be used as the basis for constructing a relatively straight-forward quantal analysis method (of the population of synapses onto a given neuron). Measurements of mPSC amplitudes are routine in the literature. However, they are likely overestimates due to small amplitude events being difficult to detect and largely being missed or lost in the noise.

The use of voltage clamp can be a major reason why mPSCs 'go missing'. Theoretical studies (Jonas et al., 1993; Major, 1993; Rall and Segev, 1985; Spruston et al., 1993) predicted, and experimental findings (Williams and Mitchell, 2008) confirmed that somatic voltage clamp fails to space clamp extended dendrites, and to capture all (or even most of) the current (thus charge) flowing in at electrically remote synapses (which instead spreads out over the entire cell membrane capacitance). Amplitude attenuation can also be caused if series resistance (R_{ser}) is not adequately compensated (Major, 1993; Williams and Mitchell, 2008). These issues can be somewhat sidestepped by switching to voltage recording, at the cost of (a little) more temporal integration by the membrane (thus overlap between minis). Although some charge is inevitably going to escape by leaking across the dendritic membrane no matter the recording method, charge escape through the relatively low membrane conductance is a much slower process than charging of the neuronal membrane via the far larger axial cytoplasmic conductance (Jonas et al., 1993; Major, 1993). In fact, it is so slow,

127 relatively, that just about all the synaptic current would be integrated onto the membrane
128 capacitance and, thus, most of the synaptic charge is 'captured' by the voltage recording (current
129 clamp), as the PSP peak amplitude, before then leaking out slowly via membrane ion channels.
130
131 However, during voltage *clamp*, most mPSCs go undetected because of the electrophysiology of the
132 neuron itself. Distal minis leak some charge via the dendritic membrane, but a far more significant
133 amplitude attenuation, 40-fold or more, is inflicted by charging the membrane capacitance of the
134 entire dendritic arbour (Larkum et al., 2009; Major et al., 2013; Nevian et al., 2007; Stuart and
135 Spruston, 1998; Williams and Mitchell, 2008; Williams and Stuart, 2002). Such amplitudes, at the
136 soma (approximately 80 µV, on average, but as small as 30 µV, in layer 5 pyramidal neurons under
137 *current* clamp (Nevian et al. 2007), detected via simultaneous dendritic whole-cell recordings) are
138 often indistinguishable from noise fluctuations. Recording from thin dendrites close to synaptic input
139 sites is technically extremely challenging – a tour de force beyond most labs. Therefore, a reliable
140 yet widely accessible quantal analysis method, based on standard somatic whole-cell patch
141 recording, would require taking account of the background noise in addition to measuring putative
142 mPSPs (or mPSCs).
143
144 Here we describe such a method, based on recording excitatory mPSPs (mEPSPs) in the presence of
145 background physiological noise ('noise with minis') then noise alone, from the same cell, after
146 blocking mEPSPs pharmacologically. To detect mEPSP-like events in these recordings, we used a
147 newly developed algorithm called 'minis' which is described in our companion article (Dervinis and
148 Major, 2024). Because of small potentials being 'overshadowed' by larger minis, either by
149 summating with them on rising phases, or having their amplitudes reduced on decaying phases
150 (analysed and discussed in detail in our companion article (Dervinis and Major, 2024)), events
151 detected in the 'noise-alone' recording cannot be used to remove the noise component in the 'noise
152 with minis' recording simply by subtracting their two distributions. Instead, we adopted the

153 approach of using simulated minis, superimposing them on the 'noise-alone' recording and varying
154 their parameters until the amplitude and rise time distributions of events *detected* in the 'noise with
155 simulated minis' voltage trace closely matches those detected in the 'noise with real minis'
156 recording, with identical detection parameters. Therefore, we augmented our 'minis' software with
157 a genetic optimisation algorithm (GA) that automatically adjusts amplitudes, rise times and
158 frequencies (rates) of simulated minis until a statistically indistinguishable match is achieved. This
159 novel quantal analysis method produced an unbiased 'upper limit' average quantal mEPSP amplitude
160 for each neuron, which unexpectedly turned out to be inversely proportional to membrane
161 capacitance. This in turn allowed us to obtain a population 'average quantal charge' estimate for
162 excitatory neocortical synapses in the rat of approximately 31 pC. This was conserved across
163 pyramidal neurons of all sizes in (somatosensory) cortical layers 2/3 and 5, across a more than 3-fold
164 range. 'Minis' thus provides an experimentally straightforward 'quantal analysis' method (in the
165 broadest sense) for detecting mPSPs (or indeed mPSCs) in somatic recordings, and (in aggregate)
166 'separating' the smaller of these events from similar-sized background noise fluctuations.
167

168 Materials and Methods

169 **Animals and electrophysiology**

170 All experimental procedures were carried out in accordance with the UK Animals (Scientific
171 Procedures) Act 1986. The full description is provided in our companion article (Dervinis and Major,
172 2024). Coronal somatosensory neocortical slices obtained from 19- to 27-day old Wistar rats
173 (RRID:RGD_13508588; n = 11) were used to obtain whole-cell voltage recordings (n = 14) of mEPSPs
174 in the background of physiological (and other) noise ('noise with minis' condition), by superfusing
175 artificial cerebrospinal fluid (aCSF) containing blockers of action potentials (APs) and inhibitory
176 postsynaptic potentials (IPSPs). Excitatory postsynaptic potential (EPSP) blockers were then added
177 ('noise-alone' condition, with all glutamatergic, GABAergic and AP-dependent synaptic potentials

178 blocked, i.e. the vast majority of fast synaptic inputs in the neocortex), and background noise traces
179 were recorded from each cell, while maintaining stability of the whole-cell recording (as judged by
180 numerous criteria, below).
181
182 Passive membrane time constant, total membrane capacitance, input resistance, and bridge balance
183 (R_{ser} compensation) error were estimated by injecting current pulses as described in (G. Major et al.,
184 1993).
185
186 **Methodology**
187 The goal of the study was to design an experimentally straightforward quantal analysis method
188 based on standard somatic recordings of minis, as opposed to far more challenging recordings from
189 sub-micron diameter input dendrites closer to (a few of) the synapses. Due to their low signal-to-
190 noise ratio, *simulated* minis were used to infer the signal (mEPSP) component and to eliminate (in
191 aggregate) the noise component in these recordings.
192
193 The experimental design of this study was similar to the one described in the preceding companion
194 article (Dervinis and Major, 2024). As described in the previous section, whole-cell recordings were
195 obtained where first mEPSPs were recorded in the background of physiological and other noise
196 followed by blocking EPSPs pharmacologically to record 'pure' noise in the absence of minis.
197 Simulated mEPSPs (smEPSPs) were then randomly added to the noise traces (Figure 1) and the
198 'minis' algorithm was applied to this 'noise with simulated minis' voltage trace. The resulting
199 distribution of detected events (in terms of their amplitudes and 10-90% rise times) was compared
200 to the equivalent distribution based on the 'noise with real minis' recording, detected with the same
201 parameters (such as amplitude detection threshold, baseline duration and maximum rise time gap
202 till each peak). The discrepancy between the two distributions was used to inform the GA, which
203 would then adjust the distribution of smEPSPs and generate new 'noise with simulated minis'

204 voltage traces and compare them again to the equivalent distribution detected with the same
205 parameters from the 'noise with real minis' recording. This procedure was repeated multiple times
206 (of the order of tens to hundreds of generations with 260 examples per generation; 10 examples per
207 each parameter optimised by the GA) until the two distributions were closely matched, within the
208 bounds of chance statistical errors (details below). At the end of this process the minis distribution
209 used for simulating the closely matched recording was deemed to be the inference of the true minis
210 distribution underlying the 'noise with real minis' recording (or at least compatible with it).
211
212 **Detection of miniature postsynaptic potentials**
213 Detection of real and simulated mEPSPs was carried out using our 'minis' software. The detailed
214 description of this detection algorithm is provided in the companion article (Dervinis and Major,
215 2024). We used the same detection algorithm parameters as described in that article except for the
216 amplitude range, which was set to 0.02-10 mV.
217
218 **Selection of recordings for fitting distributions of detected real minis-like events**
219 Prior to carrying out any estimation of the distribution of minis, segments of 'noise with real minis'
220 and 'noise-alone' recordings were carefully selected. Segments containing unusual amount of noise
221 or V_m glitches were rejected. Parts of recording showing instability or drift of recording parameters
222 (or excessive movement of the recording pipette relative to the soma) were also rejected, to ensure
223 that only good quality data were used. Data analysis performed at this preprocessing/selection stage
224 were built into our 'minis' software.
225
226 As part of the preprocessing stage, 'minis' produced seven graphs showing the evolution of various
227 recording parameters across the entire duration of a single recording. An example (from the longest
228 recording obtained) is provided in Figure 2, showing these graphs as individual panels. Figure 2A
229 shows the evolution of V_m from the very beginning of the recording obtained in the regular aCSF

230 with APs present (in this case) to the very end of the recording, where APs, mIPSPs and mEPSPs were
231 all blocked for some time ('noise-alone'). The data is shown after removing V_m segments containing
232 responses to regularly injected current pulses and has a total duration of 8520 s. Throughout the
233 entirety of this recording the baseline V_m varied between –70 and –67 mV and, thus remained
234 relatively stable.
235
236 There are three time markers that extend across all figure panels marking the time when the aSCF
237 containing TTX, gabazine, and CGP55845A was infused to block APs and IPSPs (the first marker), the
238 time when APs were observed to cease (the second marker), and the time when the aCSF containing
239 NBQX and CPP was infused to block remaining EPSPs (the third marker). The recording segment
240 between the second and the third markers constituted the 'noise with minis' recording, while the
241 segment following the third marker *after* mEPSPs were eventually blocked constituted the 'noise-
242 alone' recording. The darker yellow shaded regions that also extend across all panels of Figure 2
243 mark files (epochs) that were selected for subsequent minis distribution fitting.
244
245 The remaining panels of Figure 2 were used to guide data selection. The standard deviation (SD) of
246 the V_m (Figure 2B) was useful in determining the transitions between different pharmacological
247 conditions. Stable prolonged decreases in SD reliably indicated when APs or minis were effectively
248 blocked. Sudden brief increases in SD flagged problematic recording segments containing higher
249 levels of noise or V_m glitches. Gradual increases in SD suggested gradual deterioration of recording
250 quality.
251
252 Similar information was also provided by the evolution of the biggest 10% of amplitudes of all
253 detected minis-like events in a single sweep (Figure 2C). Prolonged drop in the amplitudes marked
254 transitions between recording conditions, while sudden jumps were indicative of V_m instabilities.
255 Finally, effective decay time constants of biggest 10% of detected events (Figure 2D) could be used

256 as an indicator for the presence/absence of minis. Blocking minis resulted in time constants
257 becoming large and fluctuating unstably, indicating that only noise fluctuations were being detected
258 that did not possess the typical decay dynamics common to EPSPs.
259
260 Further insights into the recording quality over time were provided by V_m responses to brief current
261 pulses. Passive membrane time constant measurements over time (Figure 2E) were expected to
262 remain stable. Deviations from this could signal a change in passive membrane properties due to
263 degradation in the recording quality. Total membrane capacitance (Figure 2F) was also expected to
264 be stable over time. Change in the capacitance could indicate membrane tearing, patch-resealing or
265 pipette movement or clogging, loss of membrane or part of the cell or some substantial uncontrolled
266 destabilisation of the recording. Finally, change in input resistance (detected from a change in the
267 bridge balance error; Figure 2G) was not permitted to exceed the balance error estimated offline at
268 the beginning of the recorded data by more than two-fold. Violation of this rule of thumb indicated a
269 deterioration in the recording quality potentially resulting from debris accumulating in the recording
270 pipette, movement of the pipette tip or the recorded cell body, partial formation of a membrane
271 'tube' (similar to what would happen in the process of producing an outside-out patch by slowly
272 retracting the pipette), or other reasons.
273
274 We obtained the seven longitudinal recording state/quality indicators described above for all our
275 recordings. Multi-panelled graphs showing these indicators for each individual recording separately
276 are provided in Supplementary Figures 1-13.
277
278 **Simulations**
279 *Simulating distributions of miniature excitatory postsynaptic potentials with a range of amplitudes*
280 *and rise times*

All simulations were carried out using our 'minis' software, developed in Matlab (Mathworks; RRID:SCR_001622), and performed on the Cardiff School of Biosciences' Biocomputing Hub HPC/Cloud infrastructure. Simulation of minis-like events was based on an analytical solution to the passive cable equation for a transient current (Rall, 1977) using 100 lumped terms with a double exponential synaptic current with τ_1= 0.15-3 ms (optimised in each instance/iteration) and τ_2 = 2 ms (G. Major et al., 1993). The detailed description of how arbitrary shape PSPs were obtained is provided in our companion article (Dervinis and Major, 2024).

A pool of simulated events was generated combining four bivariate (two-dimensional: amplitude and 10-90% rise time) normal distributions. Six parameters described each distribution: amplitude mean μ_X and standard deviation σ_X, 10-90% rise time mean μ_Y and standard deviation σ_Y, a correlation (or rotation) factor ρ, and a (relative frequency or number) scale factor n:

$$f(x,y) = \frac{n}{2\pi\sigma_X\sigma_Y\sqrt{1-\rho^2}} e^{-\frac{1}{2(1-\rho^2)}\left(\left(\frac{x-\mu_X}{\sigma_X}\right)^2 - 2\rho\left(\frac{x-\mu_X}{\sigma_X}\right)\left(\frac{y-\mu_Y}{\sigma_Y}\right) + \left(\frac{y-\mu_Y}{\sigma_Y}\right)^2\right)}.$$

All distribution parameters were controlled by the GA.

Fitting distributions of detected real mini-like events

The Matlab ga() function was used to control 24 parameters describing Four (rotated) bivariate normal distributions (6 parameters per distribution). Additional controlled parameters were the synaptic rise time constant τ_1 which ranged between 0.15 and 3 ms and the passive membrane time constant τ_m. The range for the latter constant was taken to be between 0.9 times and 1.1 times the initial estimate based on the averaged waveform of all minis-like events detected in the 'noise with real minis' recording. Thus, there were 26 parameters in total, controlled by the GA.

The GA would start by generating multiple distributions of simulated minis or smEPSPs (i.e. 'individuals'; we used 260 individuals per 'generation' with 10 individuals per parameter optimised

by the GA; see a single run structure in Figure3A). Events would be drawn pseudo-randomly from a distribution and then simulated events of the chosen shapes (in terms of amplitude and 10-90% rise time) would be added to the 'noise-alone' recording at times that were also chosen pseudo-randomly (Figure 1). For generating the initial set of individuals ('population'), the GA chose parameters pseudo-randomly within prescribed ranges. For each of the four bivariate normal distributions the parameter ranges were as follows: μ_X (-0.1-1 mV), σ_X (0.01-1 mV), μ_Y (-1-10 ms), σ_Y (0.25-10 ms), ρ (-1 to 1), and n (0-10,000 for the first distribution and –10,000 to 10,000 for the remaining three distributions; negative counts were used for 'sculpting' the base distribution). Any negative count bins within the resulting final distribution were zeroed out. Any events with negative rise times or amplitudes below the simulation threshold (varying non-negative value) were excluded.

Next, the GA assessed the 'fitness' of each individual in the generation by using the cost function (explained in the next subsection). The top 5% of the most fit individuals survived to the next generation without change, while individual 'crossover' ('recombination'), genetic migration, and other GA parameters were set to default values of the Matlab ga() function. A new evolved generation of individuals was then created, which then served as the basis for yet another generation and so on. This process (a single run in Figure 3A) was repeated until an 'individual' was created with the lowest cost (highest fitness value) possible, or there was no improvement in the fitness for 100 consecutive generations, or the number of generations reached 1000 (Figure 3A).

In cases where the GA terminated without converging on the highest fitness value, the distribution fitting procedure was reinitiated using the most fit individual as a seed (Runs 2 and 3 in Figure 3B). The population genetic diversity was reset by setting the GA-controlled parameter ranges to ±25% of the original ranges relative to the seed parameter values, to explore the space around the current best seed values. The re-running of distribution fitting was repeated until the GA converged to an 'apparently fittest possible individual' (or the 'best fit possible/achievable'; defined in the next

332 subsection), or otherwise an 'acceptable' level of fitness was reached (also defined in the next
333 subsection), or there was no improvement in fitness compared to the previous run for two
334 consecutive runs while an 'acceptable' fit was not yet attained (Figures 3B and C). In the latter case,
335 the entire distribution fitting procedure was reinitiated starting with a high simulated amplitude
336 lower limit (e.g., 200 μV), with the limit being gradually lowered until the 'best possible' or
337 'acceptable' fit was attained (Figure 3D). This 'backwards' ('downwards') fitting procedure was
338 required for several recordings having a large mean amplitude which, when we started with a low
339 simulated amplitude lower limit, failed to converge to an acceptable fit.
340
341 If the most fit individual was within acceptable levels of fitness values, the lower threshold on
342 smEPSP amplitude was increased by 10 μV (Figures 3B and C) (or lowered during the 'backwards' i.e.
343 'downwards' fitting procedure if no 'acceptable' fit was obtained; Figure 3D) and the entire fitting
344 step was re-run. This was repeated until the GA stopped converging (or started converging during
345 the 'backwards'/'downwards' fitting procedure) on a solution with acceptable fitness values.
346
347 The reason for attempting to push up the lower limit of the amplitudes of the smEPSPs is that it
348 became obvious that GA-generated solutions were not unique. Given an acceptable fit, matching the
349 histograms of events detected from the 'noise with real minis' recording can generally be achieved
350 by using distributions with a larger number of smaller amplitude smEPSPs, which get 'lost' in the
351 noise or summate with other smEPSPs, although the distribution of bigger smEPSPs is more tightly
352 constrained. (Indeed, one can also often (but not always) achieve acceptable fits with *fewer* small
353 amplitude smEPSPs (Supplementary Figure 14)). There is a large number of such distributions with
354 ever-decreasing amplitudes of smEPSPs (in theory, all the way down to events resulting from brief
355 single AMPA receptor (AMPAR) or NMDA receptor (NMDAR) channel sub-conductance state
356 openings, injecting undetectably small amounts of charge – rare as these may be at ambient low
357 background glutamate concentrations (Trussell and Fischbach, 1989) and resting membrane

358 potential (Ascher and Nowak, 1988)). Therefore, the GA with the thresholding procedure described
359 above has no guaranteed way of arriving at the *true* distribution of minis, only at a distribution giving
360 an approximate *upper bound* on the *mean* (or median) mini amplitude – unless further biological
361 constraints or assumptions are imposed (e.g. about background/extra-synaptic AMPAR or NMDAR
362 channel activation or minimum numbers of glutamatergic ionotropic receptor channels per
363 synapse). However, this should not be confused with the inability to 'capture' all (or most of) the
364 postsynaptic charge, as is the case with the voltage clamp method of recording, applied to big,
365 electrically distributed (non-isopotential) cells. This is rather an empirical observation of the fact that
366 our method currently has a (poorly constrained) resolution limit on the lower end of the amplitude
367 distribution of estimated minis, which may be further addressed (constrained) in future iterations.
368
369 *Cost function*
370 The goal of the minis distribution fitting procedure was to match 'noise with simulated minis' and
371 'noise with real minis' recordings as closely as possible, in terms of the distribution of amplitudes
372 and 10-90% rise times of detected mini-like events in the two types of V_m recording traces
373 ('simulated' vs. 'real' distributions), in the process 'cancelling out' any systematic errors in
374 amplitudes or shapes introduced by the detection algorithm or the summation or superposition of
375 events. This was achieved by minimising the cost function using the GA. The cost function was
376 composed of four types of components: *shape constraints* on the *simulated* minis distribution, *sums*
377 of *absolute* deviations (SADs) between 'simulated' and 'real' distributions, *sums* of *signed* deviations
378 (SSDs) between 'simulated' and 'real' distributions, and *maximal absolute* deviations (MADs)
379 between 'simulated' and 'real' distributions (Figures 4A and B). We avoided using the sum of
380 squared errors (SSE) because it is sensitive to outliers (giving them undue weight).
381
382 We calculated the typical ranges of SADs and MADs for each of the 14 recordings by taking the
383 individual 'noise with real minis' recording and dividing it into smaller files (range was 15-606 files),

each the duration of a single recording sweep (20 s, typically). Each file in this set was subjected to the minis detection procedure resulting in a set of 'real' (detected mini-like events) distributions. These were then subtracted from each other, in all pairwise combinations, and the corresponding SAD (sum of absolute deviations) and MAD (maximum absolute deviation) scores were calculated for each of the possible n*(n-1)/2 file pairings (range 105 to 183315, corresponding to 15 to 606 available files, respectively). Six SAD- and six MAD-based scores were calculated based on: distributions of amplitudes of (1) *all* detected events, (2) the largest 50%, (3) the largest 10% and (4) the largest 2% of detected events, (5) distribution of all 10-90% rise times, and (6) a joint amplitude and 10-90% rise time distribution. Three different SSD (sum of signed deviations)-based scores were calculated based on the amplitudes of (1) the largest 50%, (2) the largest 10%, and (3) the largest 2% of detected events. These latter scores constrained high-amplitude (but low count) tails of 'simulated' distributions to have sufficient counts to avoid negative distribution deviations ('simulated' – 'real').

To ensure good fits to *all* portions of the histograms, and to prevent 'dilution' or 'swamping' effects on the high amplitude (but low event frequency) tail by the low amplitude, high frequency 'hump', the smallest 'global' percentile (same for every measure) was estimated, that guaranteed to include *half* of all single-sweep file pairings (real vs. real data) with *all* their 15 respective SAD, MAD, and SSD score values falling below this percentile threshold *simultaneously* ('15-score combined 50th centile'; Figure 5 and Tables 1 and 2). This centile estimate was used to determine cut-off values for all these 15 different scores, to construct the optimisation cost function. The 'global' centile value from single sweep file comparisons was then used with SAD and MAD scores from longer files during the GA-controlled fitting procedure (typically 5 recording sweep-long files to match the size of the 'noise-alone' recording files, 100 s typically).

409 The cost function was constructed of 6 types of SAD scores and 6 types of MAD scores estimated
410 using the '15-score combined 50th centile' procedure and 3 types of SSD scores. These 15 scores
411 were used to evaluate how close the 'simulated' distribution was to the single selected 'real'
412 distribution that was deemed to be of the best quality by a human observer (Figures 4A and B).
413 Typically, it was a file close to the *end* of the 'noise with minis' recording epoch, therefore, being the
414 most similar file, in terms of recording quality parameters, to the 'noise-alone' recording epoch
415 (which was generally the *first* good-quality epoch safely *after* pharmacological blockade of
416 neurotransmission was deemed complete). An additional corresponding 15 'envelope deviation'
417 scores (same as SADs, MADs, and SSDs but comparing to the envelope or lower and upper range
418 limits of superimposed all available data distributions within that pharmacological epoch) were
419 calculated assessing how much each 'real' or 'simulated' distribution deviated from the full set
420 consisting of all the remaining 'real' distributions and the single 'simulated' distribution (Figures 4C
421 and D). The 'simulated' distribution was expected to have lower deviation scores than the worst
422 performing (most discrepant from the others) 'real' distribution (so the simulated distribution would
423 not be picked as the 'worst outlier' by a double-blind observer).
424
425 'Simulated' distributions were further penalised if their underlying source 'simulated minis'
426 distribution was non-unimodal, had a 10-90% rise time mean larger than 5 ms, or it violated a 10-
427 90% rise time skewness constraint that the mean 10-90% rise time of simulated minis should exceed
428 the median at least by a quarter of the standard deviation, as seen for the real minis (with noise)
429 distributions (range of 0.25 to 0.39 standard deviations). Finally, 'simulated' distributions were also
430 penalised if their underlying 'simulated minis' amplitude distribution had a sharp cliff at its lower
431 end. Hence, together with the four shape constraints there were 34 fitness components in total (15
432 + 15 + 4 = 34).
433

If all SAD, MAD, SSD, deviation scores, and shape constraints for comparing the 'simulated' distribution to the 'real' distributions were satisfied (≤ 15-score 50th centile SAD and MAD cutoff values and ≥0 SSD values) at the end of the fitting procedure, the fit was deemed to be the 'best possible' (a 'very good match', by all criteria). Alternatively, the fit could also be deemed 'acceptable' if all amplitude SAD, MAD, and SSD scores, as well as the distribution unimodality constraint were satisfied (excluding 10-90% rise time scores, all 'envelope deviation' scores, and the distribution skewness and 'cliff' constraints). The 'best' and 'acceptable' fits comprised the set of 'good enough' fits in terms of their GA-optimised 'fitness' which, however, did not guarantee a statistically acceptable fitness.

Final test for distribution acceptance or rejection

The notion of a 'good enough' fit is somewhat arbitrary, so far. Once the fitting procedure was completed, we set out to check whether the final fit was objectively acceptable using statistical tests. We divided the full available length of the 'noise with real minis' recording condition (epoch) into smaller files of the same length as the selected 'noise-alone' recording file and constructed a *set* of (independent) 'real' ('noise with real minis') distributions (histograms) by running the 'minis' detection algorithm on all these files (which we term the 'real distribution set'). We then compared these individual 'real' distributions to each other, pairwise, by subtracting their marginal ('1-D') amplitude and 10-90% rise time distributions from each other, taking the absolute value of the differences, and summing over all bins (bin sizes of 10 µV and 0.5 ms; bin counts were normalised by the average bin count over all 'real' distributions to increase the weight of distribution tails). So we ended up with amplitude (Figure 6A) and 10-90% rise time (Figure 6B) sets of SAD scores for each distribution (individual file) within the 'distribution set' (the 'real-real SAD score sets'; there is an amplitude and a rise time 'real-real SAD score set' for each distribution within the 'distribution set' corresponding to individual lines in Figures 6A and B). The number of SAD scores in each 'real-real SAD score set' corresponded to the number of possible comparisons between the distribution (file)

of interest and the rest of the distributions (files) = n - 1 (given n different files). Finally, we selected the 'worst' ('most discrepant') and the 'best' ('least discrepant' compared to the others) 'real' reference distributions (files; the top and the bottom rows of SAD score matrices in Figures 6A and B, respectively), in terms of their median SAD scores (median over all SADs in the 'real-real SAD score set' for that distribution). Therefore, we were left with only two sets: The 'worst real-real SAD set' and 'the best real-real SAD set'.

We also compared the 'good enough so far' ('work-in-progress') 'noise with simulated minis' distribution to all the non-reference 'real' ('noise with *real* minis') distributions. The comparison yielded another set of SAD scores: the 'simulated-real SAD score set' (Figures 6C and D). The median of this was then compared to the medians of the 'worst real-real SAD score set' and the 'best real-real SAD score set' using the non-parametric Wilcoxon signed-rank paired samples test. If the median score of the 'simulated-real SAD score set' was significantly larger than the median score of the '*worst* real-real SAD score set', (i.e. if the distributions actually were identical, that discrepancy or more would only have occurred purely by chance less than 5% of the time; Bonferroni-corrected for a requirement to simultaneously satisfy both amplitude and 10-90% rise time tests), the 'simulated' distribution was deemed to be an inadequate fit and, was therefore rejected and the fitting procedure continued. (By contrast, if the median score of the 'simulated-real SAD score set' was significantly *smaller* than the median score of the '*best* real-real SAD score set', the 'simulated' distribution was deemed likely to be an "excellent" fit; however, 'passing' this test was not strictly required and was used only for guidance). The 'work-in-progress' 'good enough' fit was ultimately accepted if the median of the 'simulated-real SAD score set' was *not* significantly larger than the median of the 'worst (most discrepant) real-real SAD score set'. Intuitively, this corresponds (roughly) to a double-blind observer not being able to pick out that (simulated minis with real noise) distribution (histogram) from the (real minis with real noise) data distributions (histograms): it was not (obviously) the 'most discrepant' histogram.

486

487 **Statistical analyses**

488 Parametric inferential statistics tests were used for incidence rates of minis (frequencies minis/s),
489 mean amplitudes, and total cell membrane capacitances, as quantile-quantile ('Q-Q') plots indicated
490 that these measures were normally distributed. Sums of absolute distribution bin deviations (SADs)
491 were often not normally distributed as assessed by Q-Q plots, and therefore were tested using the
492 corresponding non-parametric paired samples Wilcoxon signed-rank test.

493

494 **Data accessibility**

495 All data analysed in this study are publicly available (Dervinis, 2024a, 2024b). The available data
496 include 'noise with minis' and 'noise-alone' whole-cell patch membrane potential recordings that
497 were used in computer simulations and minis' distribution fitting, as well as GA distribution fitting
498 results. All electrophysiological recordings were stored in Axon Binary File (ABF) format.

499

500 **Code accessibility**

501 All analyses were carried out in Matlab and the analysis code is publicly available on GitHub
502 (Dervinis, 2024c). The code is complete with instructions on how to reproduce figures reported in
503 this study.

504

505 **Software accessibility**

506 The present study reported the use of a novel quantal analysis method that is part of 'minis'
507 software available on GitHub (Dervinis, 2024d).

508

509 # Results

510 *Estimating quantal size by direct subtraction of noise component*

511 We have analysed ‘noise with minis’ recordings and ‘noise-alone’ recordings with the ‘minis’
512 detection algorithm. Detected mEPSP-like events had an amplitude and 10-90% rise time
513 distributions that resembled log-normal or gamma distributions (Figure 7), left skewed with a long
514 tail on the right. In the amplitude domain, the lower end of the distribution contains a mixture of
515 real minis and noise fluctuations that were misidentified as real events (but also missing small minis
516 cancelled out by noise, summating with larger minis, or failing to be detected due to being on a
517 decay phase of a big preceding mini – the ‘overshadowing’ effect).
518
519 We initially tested whether the noise component (in ‘noise with minis’ recordings) could be reliably
520 estimated based on the corresponding ‘noise-alone’ recording (where synaptic activity has been
521 pharmacologically blocked), simply by directly subtracting the detected ‘noise-alone’ events
522 distribution from the ‘noise with minis’ distribution, to yield an estimate of the pure minis’
523 component. Figure 7A shows both ‘noise with minis’ and ‘noise-alone’ detected event amplitude
524 distributions superimposed. After subtracting the ‘noise-alone’ distribution from the ‘noise with
525 minis’ distribution there appear negative low amplitude bins in the resulting distribution (indicated
526 by an arrowhead in Figure 7A). These missing low amplitude events are caused by a greater number
527 of small false positive mini-like detections in the noise-alone traces, and larger minis overshadowing
528 smaller minis and small amplitude noise fluctuations in the ‘noise with minis’ recording (we have
529 discussed this phenomenon in more detail in our companion article (Dervinis and Major, 2024)).
530 Therefore, the direct subtraction approach can only provide a relatively crude ‘first order’, high-end
531 upper limit on the mean of the mini amplitude distribution. Nevertheless, this over-estimate is more
532 reliable than a highly subjective approach of simply estimating the mean amplitude based on events
533 detected using a high amplitude threshold, or worse still, detected manually, by what could, perhaps
534 uncharitably, be termed a “beauty contest” method (rather arduous, slow, subjective, and prone to
535 human error/bias).
536

Estimating quantal size by simulating excitatory postsynaptic potential source distributions

An alternative and more reliable way of estimating the quantal size in our recordings is to estimate the minis component directly using simulations. This relies on the 'minis' optimisation algorithm (GA) being able to closely match a 'noise with simulated minis' voltage trace (Figure 3) with the 'noise with real minis' recordings in terms of amplitude and 10-90% rise time distributions of minis-like events detected within these traces. We were able to successfully do that for all our recordings (see Figure 8 and Supplementary Figures 15-27). In the example shown in Figure 8, the overall amplitude SAD of the 'simulated' distribution was not significantly larger than the worst-performing 'real' distribution (unidirectional 'underfit' test: Is 'simulated' median SAD significantly > worst-performing 'real' median SAD? Wilcoxon signed-rank paired samples test statistic W (n = 16) = 105, p = 0.058 (Bonferroni-corrected due to comparing once on amplitudes and once on rise times); a high W statistic indicates a high absolute distance between the two medians, irrespective of its sign/direction, while p < 0.025 would indicate fit rejection, due to a fit SAD score being larger than the worst SAD score than would be expected by chance alone, at that significance level; downward arrow indicates 'simulated' median SAD < 'real' median SAD relationship in Figure 8) and was not outperforming the best 'real' distribution ('simulated' median SAD < best-performing 'real' median SAD Wilcoxon signed-rank paired samples unidirectional 'overfit' test W(16) = 135, p = 1; upward arrow indicates 'simulated' median SAD > 'real' median SAD relationship in Figure 8). Similarly, the 'simulated' 10-90% rise time distribution was also neither an underfit ('simulated' median SAD > worst-performing 'real' median SAD unidirectional 'underfit' test W(16) = 0, p = 1) nor an overfit ('simulated' median SAD < best-performing 'real' median SAD unidirectional 'overfit' test W(16) = 117, p = 1).

All simulations produced 'good enough' matches showing amplitude and 10-90% rise time distributions of detected minis-like events being within the range of (and thus indistinguishable from) amplitude and 10-90% rise time count values measured in sets of 'real event' distributions

563 (Supplementary Figures 15-27). None of the fits performed significantly worse than the worst-
564 performing 'real' distribution, qualifying them as 'good enough' (accepted) fits. All resulting minis
565 source distributions are displayed in Figure 9 and Supplementary Figures 28-40. An example in
566 Figure 9 shows that the 'real minis' source distribution likely has a log-normal or gamma-like shape
567 in both amplitude and rise time domains.
568
569 Incidence rates (frequencies of minis per second) estimated based on simulated minis source
570 distributions ranged roughly between 10 and 100 minis/s (a mean of 27.3 ± 2.4 minis/s and a range
571 of 6.8 to 58.1 minis/s; Figure 10). This estimate is an order of magnitude higher than the one based
572 on the literature (3.6 minis/s; (Dervinis and Major, 2024)) and significantly higher than the one based
573 on the direct subtraction method (15.9 ± 0.9 minis/s; $t(13) = 3.51$, $p = 0.004$) and also higher than
574 the estimate based on amplitudes higher than a (deliberately chosen) unrealistically high detection
575 threshold of 0.8 mV (14.3 ± 0.9 minis/s; $t(13) = 3.69$, $p = 0.003$). It is precisely within the range
576 predicted in our companion article (Dervinis and Major, 2024). However, this range is possibly still
577 somewhat of an underestimate, as mini source distributions were often generated using a lower
578 limit on simulated amplitudes to constrain the distribution non-uniqueness, as discussed in the
579 Methods subsection on the distribution fitting (also see Supplementary Figure 14).
580
581 Mean amplitudes of minis derived using simulations ranged between 53 and 182.9 μV (overall mean
582 of 114.1 ± 5.5 μV, layer 2/3 mean of 133.1 ± 9.9 μV, and layer 5 mean of 95.1 ± 11.2 μV; Figure 11A).
583 When compared to capacitance estimates (or 1/capacitance), there was a strong (very tight)
584 correlation between each cell's mean mEPSP amplitude and the inverse of its capacitance (which is
585 proportional to cell size, assuming capacitance per unit area is more or less a biological constant for
586 each cell class/type of membrane/density of channels with charged gates moving within the
587 membrane (Gentet et al., 2000); $r = 0.96$, $p = 7.1 \times 10^{-8}$, $R^2 = 0.92$). That is, the larger the cell, the
588 smaller the amplitude of its somatically detected minis and vice-versa. This relationship is predicted

589 by the theory of capacitors (C = Q/V, where C stands for capacitance, Q stands for charge, and V
590 stands for voltage across the cell's membrane), and it is a direct demonstration of an attenuating
591 effect of cell's capacitance on the amplitude of somatically detected minis. If a direct line was drawn
592 through the data and the origin of the axes in Figure 11A, the slope of this line would provide a
593 quantal size estimate for excitatory synapses in the CNS in terms of 'injected' charge (Q = ΔV/
594 Δ(1/C)) which is approximately equal to 31.3 fC, for these data. The fact that the least square fitted
595 line to the data (y = 30.6x + 2.76), with a negligibly small intercept term (2.76), roughly coincided
596 with the line through the origin fitted to the data (y = 31.3x) indicated that no obvious 'proactive'
597 mechanism *varying with cell size* was in place to compensate for the attenuation of the average
598 minis' amplitude due to the size of the cell.
599
600 Another notable observation was that the mean amplitude estimates derived either by noise
601 subtraction or by minis source distribution simulation were highly correlated ($r = 0.84$, $p = 1.49 \times 10^{-4}$,
602 $R^2 = 0.71$ Figure 11B). The equation of the line (y = 1.37x – 65.9) fitted to this data provides a
603 possible "shortcut" method to approximate the mean amplitude of fitted minis' source distribution
604 by inserting the mean estimated using 'naïve' noise subtraction directly into this equation.
605
606 *Generic miniature excitatory postsynaptic potential distribution in neocortex*
607 To construct a generic mEPSP distribution, we normalised amplitudes of simulated minis' source
608 distributions shown in Figure 9 and Supplementary Figures 28-40 by dividing them by their
609 respective means, taking the total average, and then scaling the amplitudes to the overall mean
610 (114.1 ± 5.5 μV). The resulting combined (amplitude and 10-90% rise time) distribution is shown in
611 Figures 12A and B. The corresponding marginal amplitude and 10-90% rise time distributions are
612 shown in Figures 12C and D, respectively. Both marginal distributions have left-skewed log-normal-
613 like or gamma-like distributions. This may be useful in neural network simulations, or to potentially

614 speed up (and constrain) fitting of simulated minis on noise to real minis with noise, using the GA
615 (e.g., limit the source distribution to one 2-D 'rotated' log-normal or gamma distribution).
616

617 Discussion

618 We report two major scientific advances. First, a novel quantal analysis method based on sequential
619 somatic recording, from a given neuron, of a) mEPSPs (after blockade of action potential-mediated
620 neurotransmission, and all inhibitory neurotransmission, including mIPSPs) on a background of other
621 physiological noise, and b) subsequent recordings from the same cell of noise alone, after additional
622 pharmacological blockade of mEPSPs (all glutamatergic ionotropic excitatory neurotransmission).
623 The latter type of recording provides a means to estimate the properties of the noise component
624 which can then be used to take into account noise fluctuations in the combined minis and noise
625 recording. However, this was done not by a direct subtraction of the histogram of amplitudes
626 (and/or rise times) detected from the noise-alone recordings, but rather by the simulation of the
627 underlying minis component and repeatedly superimposing (at random) the waveforms of simulated
628 minis onto the noise trace, varying source distribution parameters until the histograms detected
629 from the 'noise with simulated minis' voltage trace closely matched those detected from the 'noise
630 with real minis' recording. The key tool for achieving this match was a genetic algorithm that
631 optimised the parameters of the 2-dimensional simulated minis distribution in terms of amplitudes
632 and 10-90% rise times (and rate, i.e. minis per second), simultaneously, to best fit the experimental
633 data distributions.
634

635 The second major advance was the application of our novel quantal analysis method, that
636 successfully measured the mean 'electric charge injected' size of excitatory synapses of cortical
637 pyramidal cells, which was shown to be approximately 31.3 fC, across the entire sample of
638 neocortical pyramidal neurons recorded. This number was inferred from the slope of the line which

639 tightly fitted mean mEPSP amplitude vs. 1/total cell capacitance, in accordance with the theory of
640 capacitors. The fact that this line had an intercept at the origin of the axes indicated that there was
641 no biological compensation (other than *number* of synapses) for the amplitude attenuation of minis
642 due to cell size (i.e., total capacitance). Indeed, cell capacitance played a major role affecting the
643 *voltage* amplitude of mEPSPs, resulting in a large proportion of mEPSPs being otherwise
644 indistinguishable from noise (as independently found in numerous other studies, e.g. (Major et al.,
645 2013; Nevian et al., 2007), summarised in (Major et al., 2013)). The number of these 'missed' minis
646 was so high that the estimated minis' incidence rate (frequency) was in the order of 10-100 minis/s:
647 an order of magnitude higher than typically reported in the synaptic physiology literature (with the
648 notable exception of (Nevian et al., 2007), which predicted this result, by simultaneous dual somatic
649 and basal dendritic whole-cell patch recordings of mEPSPs, with dendritic detection, and
650 simultaneous somatic measurement). Finally, both the amplitude and 10-90% rise time distributions
651 of minis had a left-skewed log-normal- or gamma-like shape.
652
653 These findings have some major implications. First, the method, as used for estimating the mEPSP
654 distributions in cortical layers 2/3 and 5 of cells of various size, and then using these distributions to
655 arrive at the electrical size of excitatory synapses, serves as a proof of principle that it can be
656 successfully used to estimate PSP distributions of various types in the CNS. The next logical step of
657 this method is to extend its application to the estimation of amplitude and rise time distributions of
658 mIPSPs generated by different types of inhibitory synapses and, as a result, their 'electrical sizes'.
659 Moreover, the ability to obtain relatively accurate 'quantal' size estimates unobscured by
660 physiological noise is important for constraining synaptic parameters in physiologically realistic
661 simulations of neural activity. For example, now we should be able to better estimate how many
662 active synapses are needed to generate an NMDA spike within a single dendritic segment (Major et
663 al., 2013). The importance of these number estimates is not restricted to the domain of
664 physiologically realistic simulations but also extends to more abstract computations that use NMDA

665 spike-like mechanisms as coincidence detectors in the latest cortically inspired/constrained models
666 of artificial intelligence (Hawkins et al., 2019). Accurate estimates of synaptic transmission
667 parameters thus have very wide-reaching ramifications.
668
669 These findings also draw attention to some possible methodological issues in the field of synaptic
670 physiology. As discussed in our companion article (Dervinis and Major, 2024), the reported incidence
671 rates ('frequencies') for mEPSCs are generally well below 10 minis/s. Even if one doubts the
672 incidence rates we arrived with simulations, in the range of 10-100 minis/s, the rates given by 'naïve'
673 direct subtraction of the distribution of events detected in the 'noise-alone' recording from the
674 distribution based on the 'noise with minis' recording are still within 5.9 to 26.7 minis/s, which we
675 know to be an underestimate. Therefore, reported mini incidence rates below 10 minis/s are almost
676 certainly underestimates. This may have multiple causes, including lower slice temperatures in the
677 majority of studies (we used physiological, ca. 37 °C), and a significant temperature dependence of
678 synaptic release, as well as differences in slice health and slicing angle (which can affect branch and
679 local circuit 'amputations'). Another big cause could be the (inappropriate) use of voltage clamp,
680 especially if the R_{ser} is not compensated fully, as this would shrink and low-pass filter mPSCs,
681 obscuring the smaller ones. As discussed earlier, these estimates could be improved by switching to
682 voltage *recording* instead of using voltage clamp (Major, 1993; Rall and Segev, 1985; Spruston et al.,
683 1993; Williams and Mitchell, 2008), but at the price of somewhat slower decay times of minis
684 (Major, 1993), thus more temporal overlap/integration and consequent difficulties detecting peaks.
685 But more importantly, a strong association between cell capacitance (i.e. surface area) and the
686 extent to which somatically recorded minis' amplitudes are attenuated, indicates that special care
687 must be taken to account for the effect of background noise fluctuations on the amplitude
688 measurements - as we have done here. This association is yet more evidence supporting
689 experimental observations of massive mini amplitude attenuation as the PSP spreads from its
690 dendritic source location to the soma, and beyond (Larkum et al., 2009; Major et al., 2013; Nevian et

al., 2007; Stuart and Spruston, 1998; Williams and Mitchell, 2008; Williams and Stuart, 2002), especially in cells with large dendritic (or axonal) arbours, hence large surface areas and overall membrane capacitance. The apparent conservation of average synaptic charge may correspond to the observation that dendritic spines and post-synaptic densities (the specialised regions opposite release sites, containing high densities of synaptic receptors, with a substantial fraction tethered to the cytoskeleton) are not grossly different in size between different classes of pyramidal neurons in the neocortex, although differences exist between cortical layers, cortical areas, and, particularly, species (Yuste, 2010).

It is also worth noting that understanding the link between cell capacitance and somatically recorded average mini amplitudes, as well as knowing actual shapes of mini distributions in terms of their amplitudes and rise times, allows us to generate artificial data where the 'ground truth' is known. Such labelled data could perhaps be used to train artificial neural networks (ANNs) which could then be used to develop 'next generation' quantal analysis methods allowing detection of minis directly in mixed 'noise with minis' recordings. We are not the first to suggest the application of ANNs to this issue (see (Pircher et al., 2022) and (Wang et al., 2024)). However, we are not aware of attempts to use realistic mini distributions for this purpose.

Even though the novel 'quantal analysis' method we present here is an important advance, it nevertheless has limitations. One of them is the need for (relatively) long duration recordings using different pharmacological agents at various stages. However, the somatic recording set up is not as complicated and high-skill as an alternative multisite 2-photon targeted dendritic recording set up would be (Nevian et al., 2007), a heroic technique which has not to our knowledge been fully reproduced in other labs. Experiments themselves could be further streamlined, as we did in some cases, by pre-blocking action potentials before obtaining the whole-cell recordings and using high solution perfusion rates. This is particularly useful for smaller cells which are more prone to osmotic

overloading or shrinkage and resulting recording instability after a few tens of minutes (the pipette solution cannot exactly reproduce the cytoplasm, as it contains no proteins or other macromolecules, and is missing many common metabolites). Moreover, the distribution fitting procedure involving the GA can be lengthy and computationally intensive. However, the 'minis' software is parallelised at the PSP detection level, as well as at the GA optimisation level, making it particularly suitable to be executed on multi-core computing clusters. Although our 'minis' software combined with two-stage recordings offers unprecedented control for the background physiological noise, provided recording stability is very good throughout, we understand that many researchers may not be persuaded to adopt it themselves. The possibility of misleading fits if the recording noise became substantially worse between 'noise with minis' and 'noise-alone' recording phases needs to be vigilantly excluded. Nevertheless, our 'minis' software should still be useful for detecting mini-like events without recording independent noise, or fitting simulated to real distributions, if there is some other credible cut-off or separation method that can be used to distinguish between small or partially cancelled minis and mini-like noise. We anticipate, indeed, that, realistically, this scenario is likely to be its most popular use.

Some researchers may be critical of a method that does not simply rely on a direct measurement of minis but rather on an approximation via indirect means, using simulations. This is a valid criticism that could (perhaps) be addressed in the future by using a method of repeatedly subjecting a voltage recording to the minis detection procedure with an increasingly lower threshold while subtracting detected events from the voltage recording, or perhaps compensating for the 'exponential-like' decay phases of recent, temporally integrated, detected mini-like events. Some combination of these approaches could potentially recover most of the smaller minis that are 'overshadowed' by the larger ones (the so called 'negative bins' problem illustrated in Figure 7A), providing the waveforms were reasonably stereotyped in shape (not the case under voltage clamp, in neurons with large or extended or highly-branched dendritic arbours (Major, 1993; Jonas et al., 1993).

743 Furthermore, other researchers may question the ability to pharmacologically isolate the
744 background physiological noise. Our 'noise with minis' recordings may contain random openings of
745 individual AMPAR or NMDAR channels (possibly extra-synaptic), although background glutamate
746 levels are likely too low to significantly open AMPAR channels (Trussell and Fischbach, 1989), and
747 NMDAR channels would mostly be closed by Mg^{2+} block at resting membrane potential (Ascher and
748 Nowak, 1988); it is also possible (in principle), but unlikely in practice, that our 'noise-alone'
749 recordings may have failed to fully eliminate all AMPAR and NMDAR channel openings in the
750 presence of quantal release of neurotransmitter (we used high AMPAR and NMDAR blocker doses,
751 well above IC50s' (Lehmann et al., 1987; Randle et al., 1992) and rapid slice perfusion, to achieve
752 quick wash-in times, and checked for stationarity of the blockade by comparing multiple measures
753 from consecutive traces: see Supplementary Figures 1-13). Background/physiological/electrical noise
754 itself may also be drifting between two such (hypothetical) conditions, with the presence or absence
755 of mEPSP pharmacological blockers. Occasionally, we rejected recordings (or epochs) with suspicious
756 or obvious instabilities. These factors are unlikely to have affected the results significantly, due to
757 the small amplitudes of any remaining membrane potential variations from these potential (but
758 unlikely) causes in the fitted cells. Two largely independent analyses of the same data by the two
759 authors separately yielded similar results and conclusions (albeit with somewhat different data
760 selection, sweep lengths, and tests of goodness of fits: the 'first pass', not presented here, relied
761 more on 'double-blind' visual inspection of multiple real minis with noise data distributions from the
762 same cell superimposed on the simulated minis with noise fit distribution: if the latter 'stood out
763 obviously from the crowd', it was rejected).
764
765 Finally, researchers may be reluctant to switch from the more commonly used voltage clamp
766 recording method to unclamped voltage recording and, thus, would question whether our method
767 captures postsynaptic currents in their full totality without distortions. We accept that there are
768 experimental settings where the use of the voltage clamp may be preferred, like recording from

769 small electrically compact granule cells in the cerebellum. 'minis' is not limited only to applications
770 involving postsynaptic potentials and can equally well be used in detecting and analysing
771 postsynaptic *currents* (indeed we have done so for several of the cells reported here, unpublished
772 observations). However, as we argued throughout this article, the benefits of unclamped voltage
773 recording in large cells are striking. Unlike voltage clamp, voltage recording offers a near-full capture
774 of postsynaptic charge in these cells (when estimated from the PSP peak amplitude). Current leak
775 through the membrane is relatively low, to first order, during the fast EPSP rising phase (i.e. during
776 rapid axial charge redistribution; Major et al. 1993a), and recording of 'noise with minis' and 'noise-
777 alone' combined with optimised simulations offers an unprecedented ability to estimate the actual
778 minis population distribution and the upper limit on their average amplitudes. When care is taken to
779 block other synaptic currents (as we did), then (in these neurons, at least) any
780 boosting/sculpting/shunting impact of other active membrane channels can be ignored, reasonably
781 safely, to first order, at the resting V_m, as somatic (and dendritic) pulse responses scale relatively
782 linearly within ca. 10 mV transients in this V_m range (Nevian et al., 2007). Voltage *recording* is also
783 more resilient to small changes in R_{ser} and the compensation thereof, which under voltage *clamp*
784 could substantially affect noise. Under voltage clamp, the noise recorded during the minis epoch
785 may be different than during the noise-alone epoch, if (say) R_{ser} were to creep up a little. In part, this
786 is because the clamp currents are directly proportional to compensated series conductance (Guy
787 Major et al., 1993), so under voltage clamp, small changes in R_{ser} could differentially affect minis
788 (with 'their' noise) and noise recorded later, following any non-stationarities.
789
790 Despite some of the limitations discussed above, the method and its application to neocortical
791 excitatory connections presented in this article provide a useful advance in the field of synaptic
792 physiology. Logical next steps could include the application of this novel quantal analysis method to
793 establish the properties of other types of excitatory synapse, and various types of inhibitory synapse,

794 in both neocortex and hippocampus, and in other species, and to investigate whether average

795 synaptic ‘size’ (injected charge) is more widely conserved within different cell classes.

References

Ascher P, Nowak L. 1988. The role of divalent cations in the N-methyl-D-aspartate responses of mouse central neurones in culture. *J Physiol* **399**:247–266. doi:https://doi.org/10.1113/jphysiol.1988.sp017078

Bekkers JM. 1994. Quantal analysis of synaptic transmission in the central nervous system. *Curr Opin Neurobiol* **4**:360–365. doi:https://doi.org/10.1016/0959-4388(94)90097-3

Biró ÁA, Holderith NB, Nusser Z. 2005. Quantal Size Is Independent of the Release Probability at Hippocampal Excitatory Synapses. *The Journal of Neuroscience* **25**:223–232. doi:10.1523/JNEUROSCI.3688-04.2005

Brown TH, Wong RKS, Prince DA. 1979. Spontaneous miniature synaptic potentials in hippocampal neurons. *Brain Res* **177**:194–199. doi:https://doi.org/10.1016/0006-8993(79)90931-4

Clamann HP, Rioult-Pedotti MS, Luscher HR. 1991. The influence of noise on quantal EPSP size obtained by deconvolution in spinal motoneurons in the cat. *J Neurophysiol* **65**:67–75. doi:10.1152/jn.1991.65.1.67

Clements JD. 2003. Variance–mean analysis: a simple and reliable approach for investigating synaptic transmission and modulation. *J Neurosci Methods* **130**:115–125. doi:https://doi.org/10.1016/j.jneumeth.2003.09.019

Clements JD, Silver RA. 2000. Unveiling synaptic plasticity: a new graphical and analytical approach. *Trends Neurosci* **23**:105–113. doi:10.1016/S0166-2236(99)01520-9

del Castillo J, Katz B. 1954. Quantal components of the end-plate potential. *J Physiol* **124**:560–573. doi:https://doi.org/10.1113/jphysiol.1954.sp005129

Dervinis M. 2024a. https://gin.g-node.org/dervinism/minis-benchmarking-data2. *GIN*. doi:10.12751/g-node.mvsy4j

Dervinis M. 2024b. https://gin.g-node.org/dervinism/minis-quantal-analysis-data. *GIN*. doi:10.12751/g-node.32m2ge

Dervinis M. 2024c. https://github.com/dervinism/minis-quantal-analysis. *GitHub*. doi:10.5281/zenodo.14288653

Dervinis M. 2024d. https://github.com/dervinism/minis. doi:10.5281/zenodo.14573132

Dervinis M, Major G. 2024. A novel method for reliably measuring miniature and spontaneous postsynaptic potentials/currents in whole-cell patch clamp recordings in the central nervous system. *bioRxiv*. doi:10.1101/2022.03.20.485046

Edwards FR, Redman SJ, Walmsley B. 1976. Statistical fluctuations in charge transfer at Ia synapses on spinal motoneurones. *J Physiol* **259**:665–688. doi:https://doi.org/10.1113/jphysiol.1976.sp011488

Enoki R, Hu Y, Hamilton D, Fine A. 2009. Expression of Long-Term Plasticity at Individual Synapses in Hippocampus Is Graded, Bidirectional, and Mainly Presynaptic: Optical Quantal Analysis. *Neuron* **62**:242–253. doi:10.1016/j.neuron.2009.02.026

833 Farsi Z, Walde M, Klementowicz AE, Paraskevopoulou F, Woehler A. 2021. Single synapse glutamate
834 imaging reveals multiple levels of release mode regulation in mammalian synapses. *iScience* **24**.
835 doi:10.1016/j.isci.2020.101909

836 Fatt P, Katz B. 1952. Spontaneous subthreshold activity at motor nerve endings. *J Physiol* **117**:109–
837 128.

838 Forti L, Bossi M, Bergamaschi A, Villa A, Malgaroli A. 1997. Loose-patch recordings of single quanta at
839 individual hippocampal synapses. *Nature* **388**:874–878. doi:10.1038/42251

840 Gentet LJ, Stuart GJ, Clements JD. 2000. Direct Measurement of Specific Membrane Capacitance in
841 Neurons. *Biophys J* **79**:314–320. doi:https://doi.org/10.1016/S0006-3495(00)76293-X

842 Hardingham NR, Read JCA, Trevelyan AJ, Nelson JC, Jack JJB, Bannister NJ. 2010. Quantal Analysis
843 Reveals a Functional Correlation between Presynaptic and Postsynaptic Efficacy in Excitatory
844 Connections from Rat Neocortex. *The Journal of Neuroscience* **30**:1441–1451.
845 doi:10.1523/JNEUROSCI.3244-09.2010

846 Hawkins J, Lewis M, Klukas M, Purdy S, Ahmad S. 2019. A Framework for Intelligence and Cortical
847 Function Based on Grid Cells in the Neocortex. *Front Neural Circuits* **12**.
848 doi:10.3389/fncir.2018.00121

849 Heuser JE, Reese TS, Dennis MJ, Jan Y, Jan L, Evans L. 1979. Synaptic vesicle exocytosis captured by
850 quick freezing and correlated with quantal transmitter release. *Journal of Cell Biology* **81**:275–
851 300. doi:10.1083/jcb.81.2.275

852 Isaacson JS, Walmsley B. 1995. Counting quanta: Direct measurements of transmitter release at a
853 central synapse. *Neuron* **15**:875–884. doi:10.1016/0896-6273(95)90178-7

854 Jack JJ, Redman SJ, Wong K. 1981. The components of synaptic potentials evoked in cat spinal
855 motoneurones by impulses in single group Ia afferents. *J Physiol* **321**:65–96.
856 doi:https://doi.org/10.1113/jphysiol.1981.sp013972

857 Jonas P, Major G, Sakmann B. 1993. Quantal components of unitary EPSCs at the mossy fibre
858 synapse on CA3 pyramidal cells of rat hippocampus. *J Physiol* **472**:615–663.
859 doi:https://doi.org/10.1113/jphysiol.1993.sp019965

860 Katz B. 1969. The Release of Neural Transmitter Substances. Liverpool: Liverpool Univ. Press.

861 Korn H, Faber DS. 1991. Quantal analysis and synaptic efficacy in the CNS. *Trends Neurosci* **14**:439–
862 445. doi:https://doi.org/10.1016/0166-2236(91)90042-S

863 Kraszewski K, Grantyn R. 1992. Unitary, quantal and miniature gaba-activated synaptic chloride
864 currents in cultured neurons from the rat superior colliculus. *Neuroscience* **47**:555–570.
865 doi:https://doi.org/10.1016/0306-4522(92)90165-X

866 Kullmann DM, Nicoll RA. 1992. Long-term potentiation is associated with increases in quantal
867 content and quantal amplitude. *Nature* **357**:240–244. doi:10.1038/357240a0

868 Kuno M. 1964. Quantal components of excitatory synaptic potentials in spinal motoneurones. *J*
869 *Physiol* **175**:81–99. doi:https://doi.org/10.1113/jphysiol.1964.sp007504

870 Larkman A, Stratford K, Jack J. 1991. Quantal analysis of excitatory synaptic action and depression in
871 hippocampal slices. *Nature* **350**:344–347. doi:10.1038/350344a0

Larkum ME, Nevian T, Sandler M, Polsky A, Schiller J. 2009. Synaptic Integration in Tuft Dendrites of Layer 5 Pyramidal Neurons: A New Unifying Principle. *Science (1979)* **325**:756–760. doi:10.1126/science.1171958

Lehmann J, Schneider J, McPherson S, Murphy DE, Bernard P, Tsai C, Bennett DA, Pastor G, Steel DJ, Boehm C. 1987. CPP, a selective N-methyl-D-aspartate (NMDA)-type receptor antagonist: characterization in vitro and in vivo. *Journal of Pharmacology and Experimental Therapeutics* **240**:737–746.

Liu Z, Lu X, Villette V, Gou Y, Colbert KL, Lai S, Guan S, Land MA, Lee J, Assefa T, Zollinger DR, Korympidou MM, Vlasits AL, Pang MM, Su S, Cai C, Froudarakis E, Zhou N, Patel SS, Smith CL, Ayon A, Bizouard P, Bradley J, Franke K, Clandinin TR, Giovannucci A, Tolias AS, Reimer J, Dieudonné S, St-Pierre F. 2022. Sustained deep-tissue voltage recording using a fast indicator evolved for two-photon microscopy. *Cell* **185**:3408-3425.e29. doi:10.1016/J.CELL.2022.07.013

Major G. 1993. Solutions for transients in arbitrarily branching cables: III. Voltage clamp problems. *Biophys J* **65**:469–491. doi:10.1016/S0006-3495(93)81039-7

Major G., Evans JD, Jack JJ. 1993. Solutions for transients in arbitrarily branching cables: I. Voltage recording with a somatic shunt. *Biophys J* **65**:423–449. doi:10.1016/S0006-3495(93)81037-3

Major Guy, Evans JD, Jack JJB. 1993. Solutions for transients in arbitrarily branching cables: II. Voltage clamp theory. *Biophys J* **65**:450–468. doi:https://doi.org/10.1016/S0006-3495(93)81038-5

Major G, Larkum ME, Schiller J. 2013. Active Properties of Neocortical Pyramidal Neuron Dendrites. *Annu Rev Neurosci* **36**:1–24. doi:10.1146/annurev-neuro-062111-150343

Nevian T, Larkum ME, Polsky A, Schiller J. 2007. Properties of basal dendrites of layer 5 pyramidal neurons: a direct patch-clamp recording study. *Nat Neurosci* **10**:206–214. doi:10.1038/nn1826

Oertner TG, Sabatini BL, Nimchinsky EA, Svoboda K. 2002. Facilitation at single synapses probed with optical quantal analysis. *Nat Neurosci* **5**:657–664. doi:10.1038/nn867

Peled ES, Isacoff EY. 2011. Optical quantal analysis of synaptic transmission in wild-type and rab3-mutant Drosophila motor axons. *Nat Neurosci* **14**:519–526. doi:10.1038/nn.2767

Pircher T, Pircher B, Feigenspan A. 2022. A novel machine learning-based approach for the detection and analysis of spontaneous synaptic currents. *PLoS One* **17**:1–16. doi:10.1371/journal.pone.0273501

Rall W. 1977. Core Conductor Theory and Cable Properties of Neurons In: Kandel ER, Brookhardt JM, Mountcastle VM, editors. Handbook of Physiology, Cellular Biology of Neurons. Bethesda, MD: American Physiological Society. pp. 39–97.

Rall W, Segev I. 1985. Space-clamp problems when voltage clamping branched neurons with intracellular microelectrodes In: T. G. Smith Jr, Lecar H, Redman SJ, Gage P, editors. Voltage and Patch Clamping with Microelectrodes. Bethesda, MD: American Physiological Society. pp. 191–215.

Randle JCR, Guet T, Cordi A, Lepagnol JM. 1992. Competitive inhibition by NBQX of kainate/AMPA receptor currents and excitatory synaptic potentials: importance of 6-nitro substitution. *Eur J Pharmacol* **215**:237–244. doi:https://doi.org/10.1016/0014-2999(92)90033-Z

Redman S. 1990. Quantal analysis of synaptic potentials in neurons of the central nervous system. *Physiol Rev* **70**:165–198. doi:10.1152/physrev.1990.70.1.165

Reid CA, Clements JD. 1999. Postsynaptic expression of long-term potentiation in the rat dentate gyrus demonstrated by variance-mean analysis. *J Physiol* **518**:121–130. doi:https://doi.org/10.1111/j.1469-7793.1999.0121r.x

Sahara Y, Takahashi T. 2001. Quantal components of the excitatory postsynaptic currents at a rat central auditory synapse. *J Physiol* **536**:189–197. doi:https://doi.org/10.1111/j.1469-7793.2001.00189.x

Silver RA. 2003. Estimation of nonuniform quantal parameters with multiple-probability fluctuation analysis: theory, application and limitations. *J Neurosci Methods* **130**:127–141. doi:https://doi.org/10.1016/j.jneumeth.2003.09.030

Spruston N, Jaffe DB, Williams SH, Johnston D. 1993. Voltage- and space-clamp errors associated with the measurement of electrotonically remote synaptic events. *J Neurophysiol* **70**:781–802. doi:10.1152/jn.1993.70.2.781

Stern P, Edwards FA, Sakmann B. 1992. Fast and slow components of unitary EPSCs on stellate cells elicited by focal stimulation in slices of rat visual cortex. *J Physiol* **449**:247–278. doi:https://doi.org/10.1113/jphysiol.1992.sp019085

Stuart G, Spruston N. 1998. Determinants of Voltage Attenuation in Neocortical Pyramidal Neuron Dendrites. *The Journal of Neuroscience* **18**:3501–3510. doi:10.1523/JNEUROSCI.18-10-03501.1998

Trussell LO, Fischbach GD. 1989. Glutamate receptor desensitization and its role in synaptic transmission. *Neuron* **3**:209–218. doi:10.1016/0896-6273(89)90034-2

Vere-Jones D. 1966. Simple Stochastic Models for the Release of Quanta of Transmitter from a Nerve Terminal. *Australian Journal of Statistics* **8**:53–63. doi:https://doi.org/10.1111/j.1467-842X.1966.tb00164.x

Wall MJ, Usowicz MM. 1998. Development of the quantal properties of evoked and spontaneous synaptic currents at a brain synapse. *Nat Neurosci* **1**:675–682. doi:10.1038/3677

Wang N-S, Marino M, Malinow R. 2024. Detecting unitary synaptic events with machine learning. *Proceedings of the National Academy of Sciences* **121**:e2315804121. doi:10.1073/pnas.2315804121

Williams SR, Mitchell SJ. 2008. Direct measurement of somatic voltage clamp errors in central neurons. *Nat Neurosci* **11**:790–798. doi:10.1038/nn.2137

Williams SR, Stuart GJ. 2002. Dependence of EPSP Efficacy on Synapse Location in Neocortical Pyramidal Neurons. *Science (1979)* **295**:1907–1910. doi:10.1126/science.1067903

Yuste R. 2010. Dendritic Spines. The MIT Press. doi:10.7551/mitpress/9780262013505.001.0001

Yuste R, Majewska A, Cash SS, Denk W. 1999. Mechanisms of Calcium Influx into Hippocampal Spines: Heterogeneity among Spines, Coincidence Detection by NMDA Receptors, and Optical Quantal Analysis. *The Journal of Neuroscience* **19**:1976–1987. doi:10.1523/JNEUROSCI.19-06-01976.1999

Figures

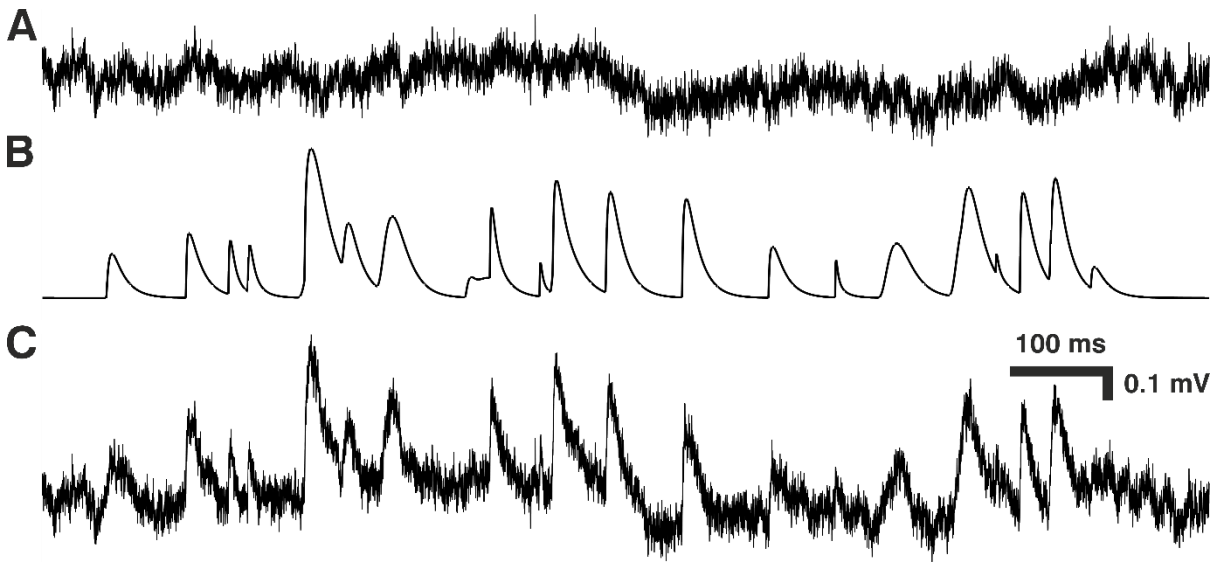

Figure 1: Constructing 'noise with simulated minis' voltage trace.

(A) Segment of 'noise-alone' voltage recording (from cortical layer 2/3 pyramidal neuron p131a).

(B) Simulated mEPSPs that were randomly added to the noise-alone trace in (A) to produce the 'real noise with simulated mEPSPs' voltage trace in (C).

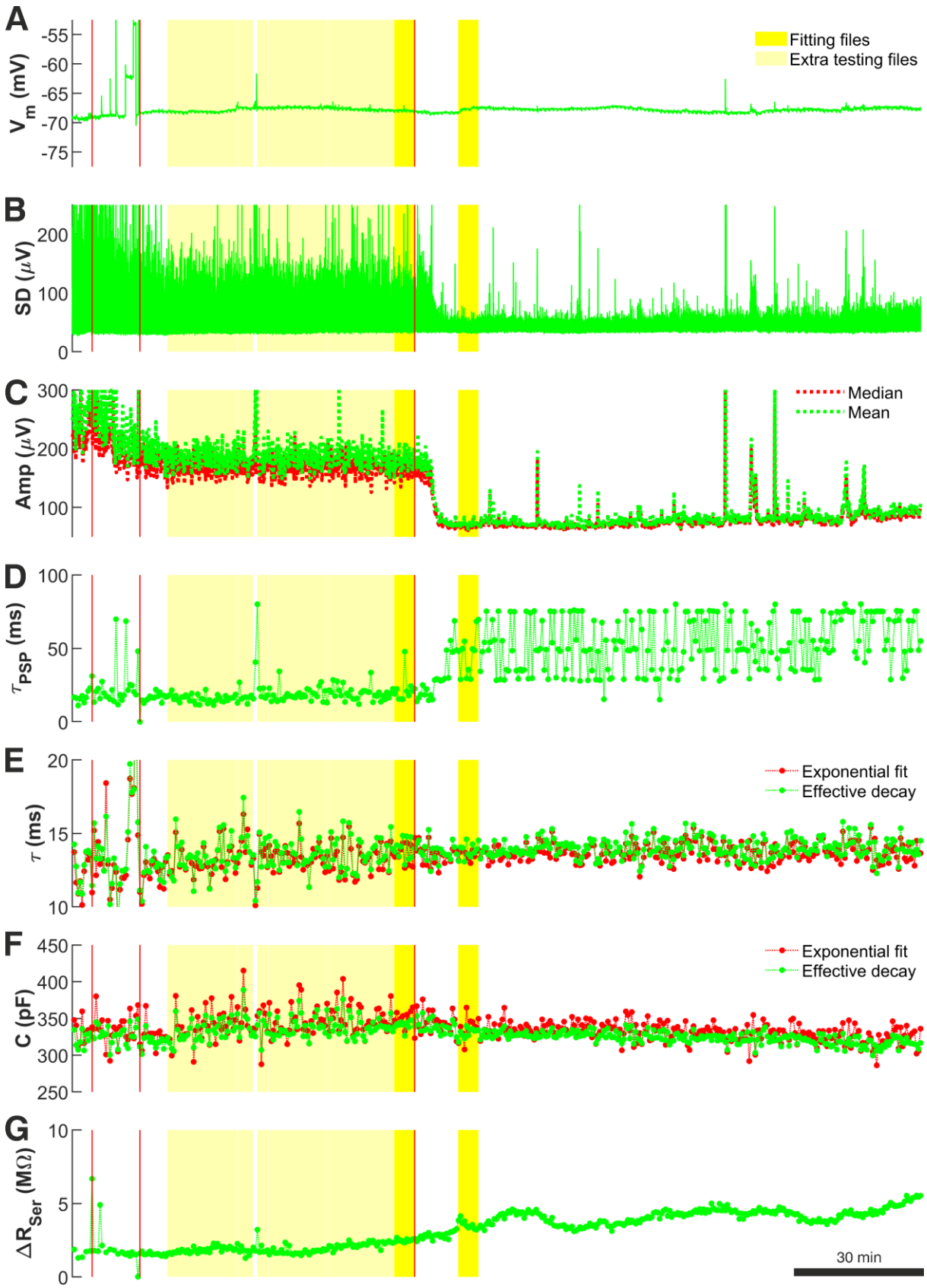

Figure 2: Recording quality measures used during the data preprocessing stage to select 'noise with

962 minis' and 'noise-alone' recording sweeps for further data analysis for recording p103a (layer 5
963 'burster' with tuft and thick trunk).
964 (A) Baseline V_m across the entire recording session. Stimulation pulses were excluded from the
965 display. The total recording duration (excluding pulse periods) was 8520 s. The first red vertical line
966 marks the time when pharmacological blockade of APs was initiated. The second red vertical line
967 marks the time when no more APs were observed in the recording. The third red vertical line marks
968 the time when pharmacological blockade of mEPSPs was initiated. Bright yellow periods mark 'noise
969 with minis' and 'noise-alone' recording segments selected as the main comparison files for the
970 distribution fitting. Light yellow marks all the remaining good quality 'noise with minis' recording
971 sweeps that were also included in the distribution fitting procedure for estimating target SAD, MAD,
972 and 'deviation' scores, as well as statistical evaluation of fits (see Methods).
973 (B) V_m standard deviation measured over consecutive 15 ms windows over the same recording
974 session.
975 (C) Evolution of mean and median amplitudes of the biggest top 10% of detected events (including
976 minis and noise events), averaged over single sweeps (duration of each was 4 s).
977 (D) Effective decay time constants (time to drop to 1/e of starting value 'safely' (8 ms) after the peak
978 and upwardly convex part) of the same biggest 10% of detected events as in panel (C) averaged over
979 consecutive 20-second-long (5-sweep-long) segments across the same session. Once minis were
980 blocked pharmacologically, effective time constant of detected events, (now pure noise) increased,
981 and its scatter, so this is another useful indication of when the block is complete.
982 (E) Evolution of passive membrane time constant over the entire recording session. Measurements
983 were averaged over consecutive 20-second-long (5-sweep-long) segments. Measurements based on
984 exponential decay curve fit and on 'effective time constant' (time for V_m to drop to 1/e of a value
985 just after change in current (after pipette capacitance artefact and fast charge redistribution
986 components: starting at 4 ms after the end of the pulse).

987 (F) Evolution of total cell membrane capacitance across the recording session. Measurements were
988 averaged over consecutive 20-second-long (5-sweep-long) segments. Measurements based on
989 exponential decay curve fit and on effective time constant (time taken for V_m drop to 1/e of an initial
990 value of the slowest impulse response component).
991 (G) Evolution of whole-cell pipette series resistance change (bridge balance error) across the
992 recording session, calculated from any jumps at starts or ends of charging curves. Measurements
993 were averaged over consecutive 4-second-long (5-sweep-long) segments.
994

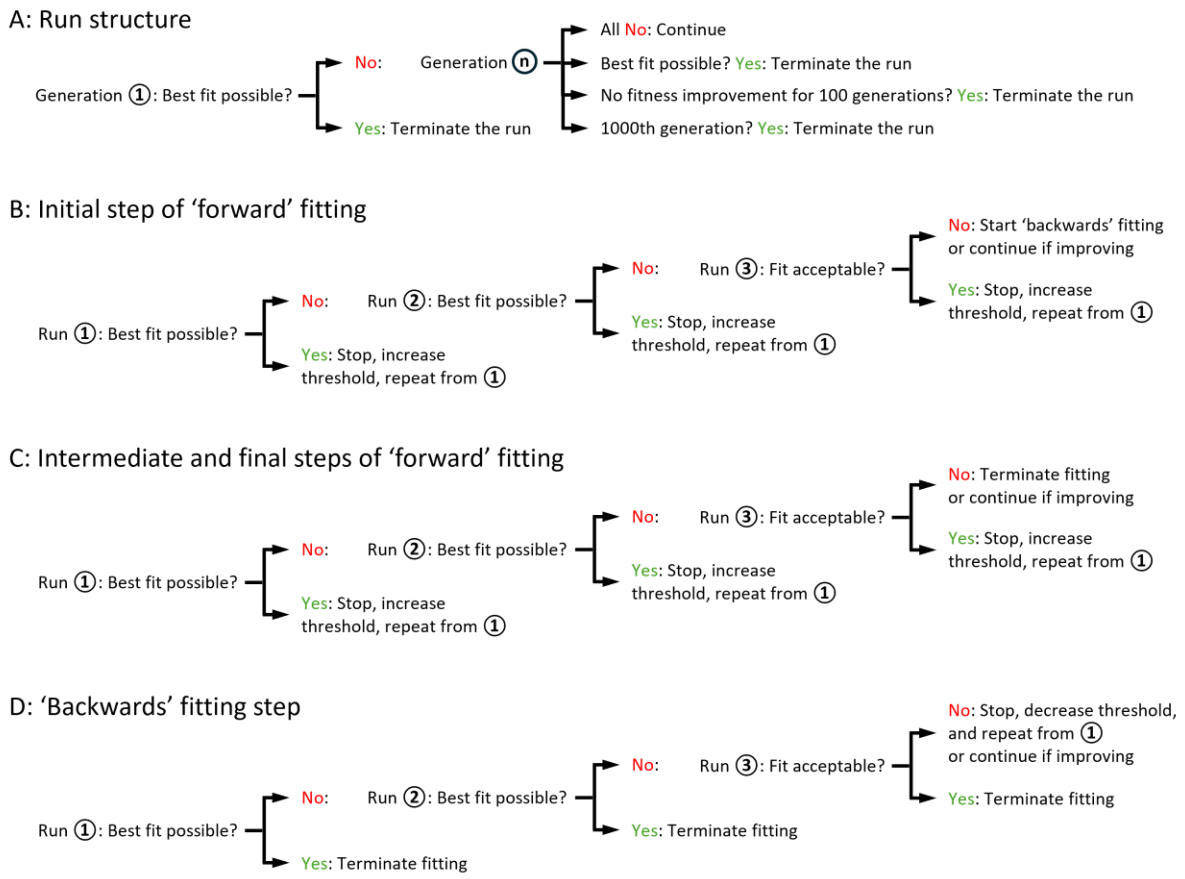

Figure 3: Schematic illustration of 'minis' genetic algorithm execution steps leading to the discovery of a minis source distribution underlying a distribution of minis-like events detected in a 'noise with minis' recording.

(A) The structure of a single GA run.

(B) The structure of the initial step of the 'forward' ('upward') fitting procedure where the lower threshold of the simulated minis amplitude is gradually raised.

(C) The structure of intermediate and final steps of the 'forward' ('upward') fitting procedure.

(D) The structure of the 'backwards' ('downwards') fitting procedure where the lower threshold of the simulated minis amplitude is gradually lowered.

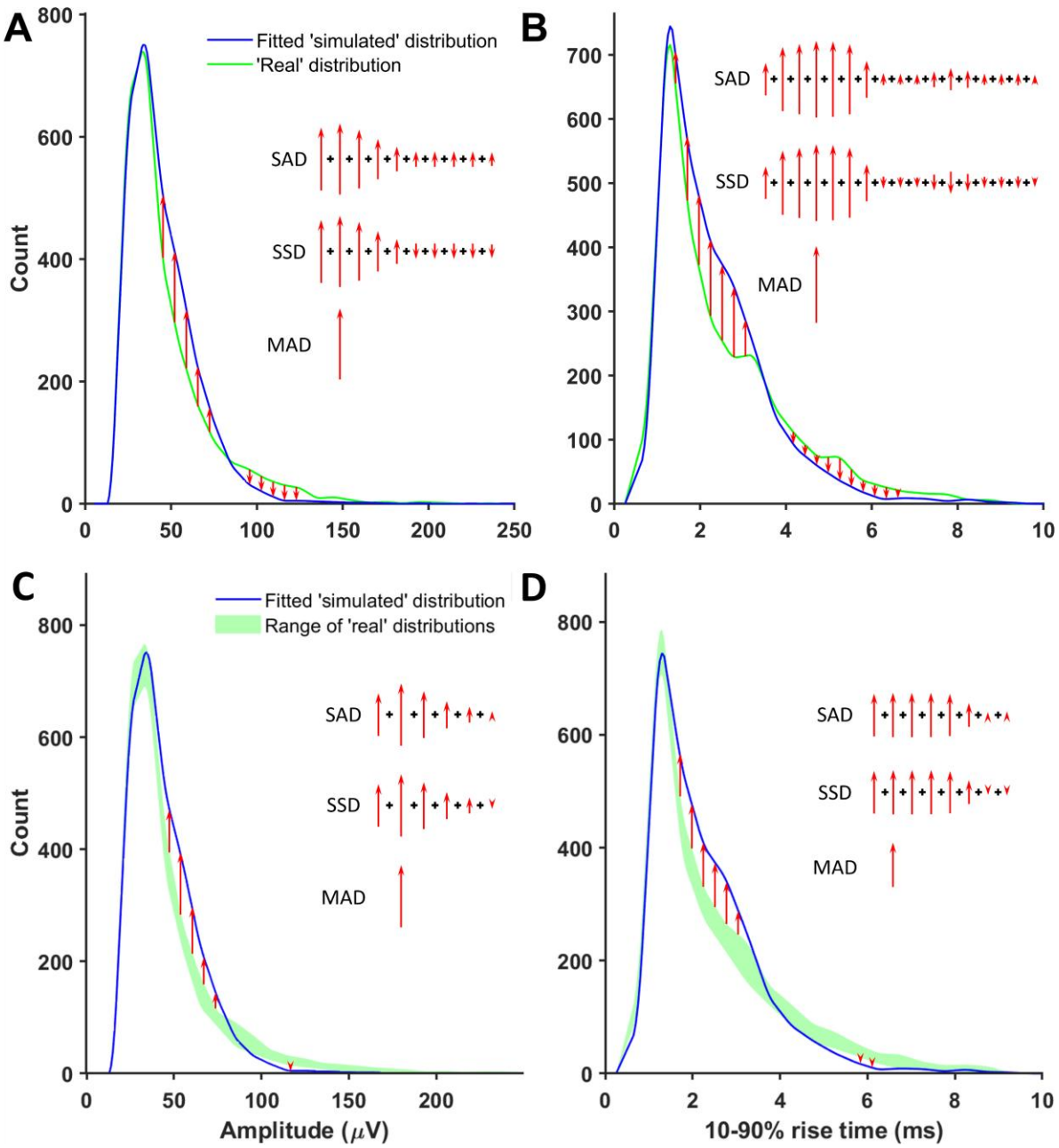

Figure 4: Non-shape components of the genetic algorithm's cost function.

(A) A schematic illustration of how amplitude SADs, MADs, and SSDs were calculated. Red arrows mark detected minis-like event count discrepancies between 'simulated' and 'real' 'noise with minis' distribution bins.

(B) A schematic illustration of how 10-90% rise time SADs, MADs, and SSDs were calculated.

(C) A schematic illustration of how amplitude 'envelope deviation' scores corresponding to SADs, MADs, and SSDs were calculated. Red arrows mark detected minis-like event count discrepancies

1014 between the ‘noise with simulated minis’ distribution and the envelope of all superimposed ‘noise

1015 with real minis’ distribution bins.

1016 (D) A schematic illustration of how 10-90% rise time ‘envelope deviation’ scores corresponding to

1017 SADs, MADs, and SSDs were calculated.

1018

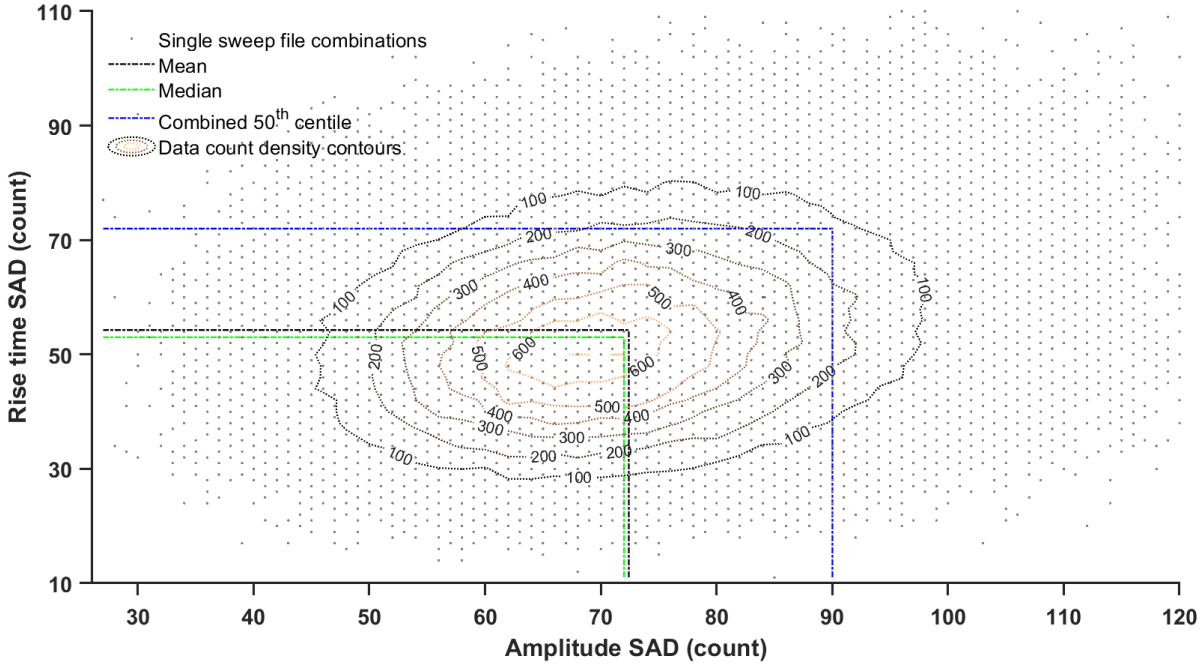

Figure 5: Amplitude and rise time scattergram (density plot) of sum of absolute deviation (SAD) scores between histograms from all possible pairs of 'noise with minis' single sweep files (4 s) from a layer 5 pyramidal neuron (p103a).

The line marking 'combined 50th centile' cutoff is based on 15 different SAD, SSD, and MAD scores as explained in Tables 1 and 2 (it extends to the remaining 13 dimensions not shown here). '15-score combined 50th centile' sets a lower (more exacting) threshold for accepting ('steering') distribution fits than the mean or the median would. This is justified because distribution fits need to satisfy all 15 SAD, SSD, and MAD scores *simultaneously* (e.g. to ensure that one of the tails of the distribution is not badly fit, as well as the remaining parts of the distribution).

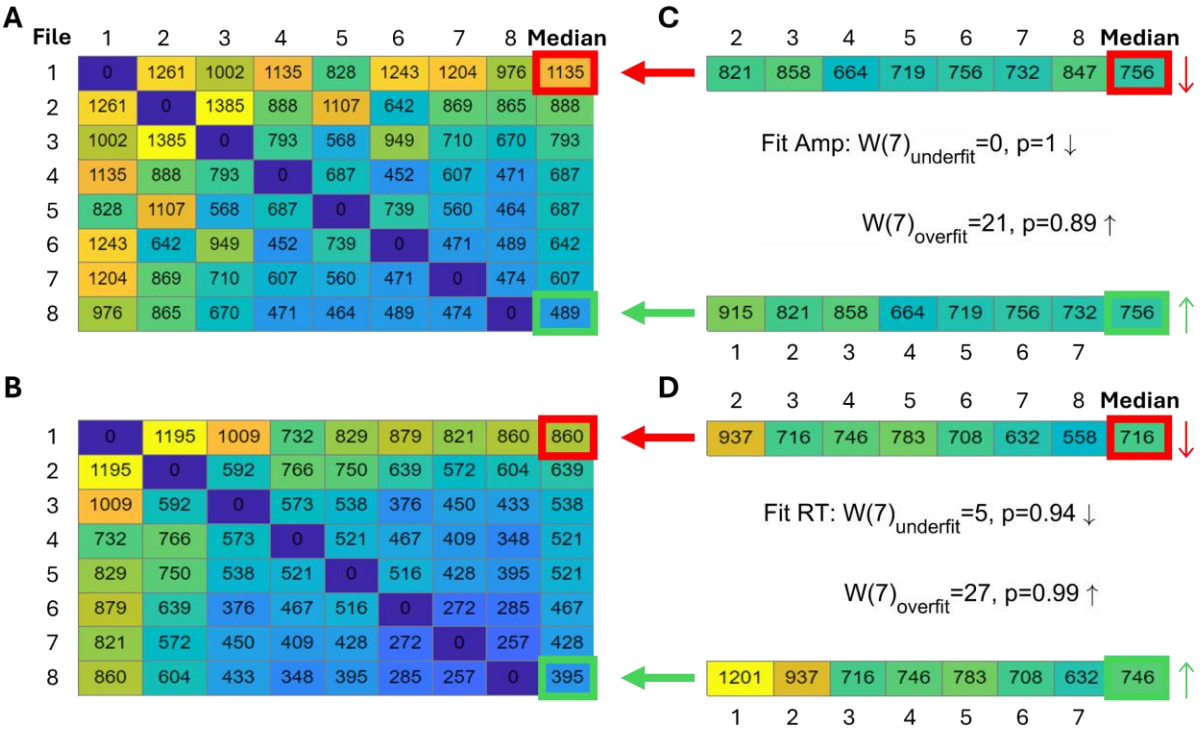

Figure 6: A schematic illustration of simulated minis distribution acceptance tests.

(A) A matrix showing amplitude SADs for all 'noise with real minis' recording file comparisons. The last matrix column shows the median SAD score for all comparisons in individual matrix rows. The matrix cell with thick red borders indicates the 'worst'-performing distribution, while the cell with thick green borders indicates the 'best'-performing distribution.

(B) A matrix showing 10-90% rise time SADs for all 'noise with real minis' recording file comparisons.

(C) Two sets of SADs for comparisons of the 'noise with simulated minis' amplitude distribution and all non-reference 'noise with real minis' amplitude distributions. The top vector contains comparisons with the same 'real' distributions/files as the top matrix row in (A) as indicated by the thick red arrow (the reference 'worst' distribution was excluded from the comparison). The thin red arrow points in the downward direction consistent with the 'simulated' median (right) being lower than the 'real' 'worst'-performing distribution's median (left). The bottom vector contains comparisons with the same 'real' distributions/files as the bottom matrix row in (A) as indicated by the thick green arrow (the reference 'best' distribution was excluded from the comparison). The thin green arrow points in the upward direction consistent with the 'simulated' median (right) being

higher than the ‘real’ ‘best’-performing distribution’s median (left). Results of the amplitude acceptance Wilcoxon signed-rank paired samples test for the simulated minis distribution are shown in the middle between the two SAD vectors. The top line tests whether the median of the SAD vector top set in (C) is larger than the median in the red-bordered cell of the matrix in (A) ($W_{underfit}$; the number of files/distributions minus the reference distribution is indicated within brackets). The downward arrow indicates that the median of the SAD vector in (C) is smaller than the red-bordered median in (A). The bottom line tests whether the median of the SAD vector bottom set is smaller than the median in the green-bordered cell of the matrix in (A) ($W_{overfit}$). The upward arrow indicates that the median of the SAD vector in (C) is larger than the green-bordered median in (A).

(D) A set of SADs and acceptance tests as in (C) but for the 10-90% rise time distribution of simulated minis.

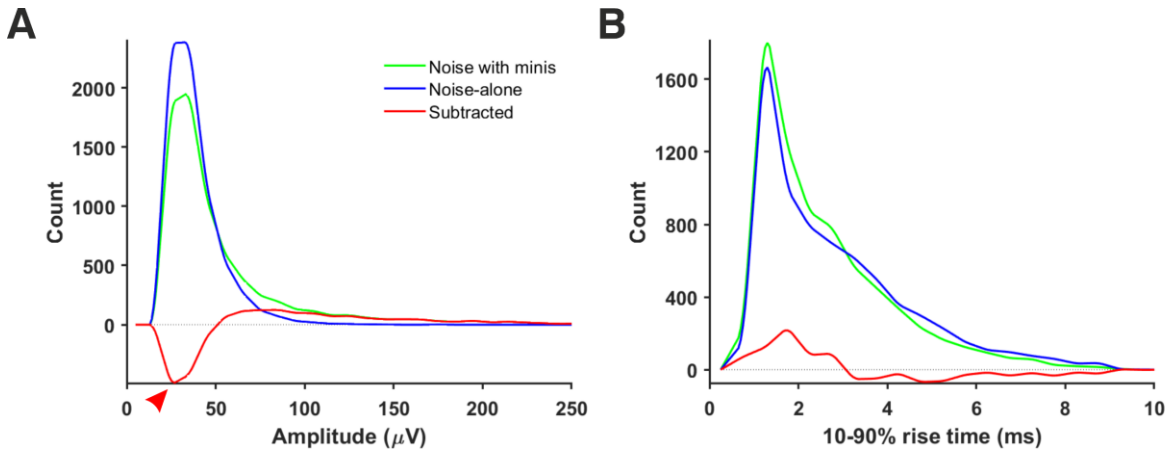

Figure 7: Amplitude and rise time distributions of detected mini-like events in 'noise with minis' and 'noise-alone' recordings.

(A) Amplitude distributions in a "thick" tufted neocortical layer 5 pyramidal neuron (p108b). Red arrowhead indicates negative bins after subtracting 'noise-alone' distribution from 'noise with minis' distribution.

(B) 10-90% rise time distributions from the same neuron.

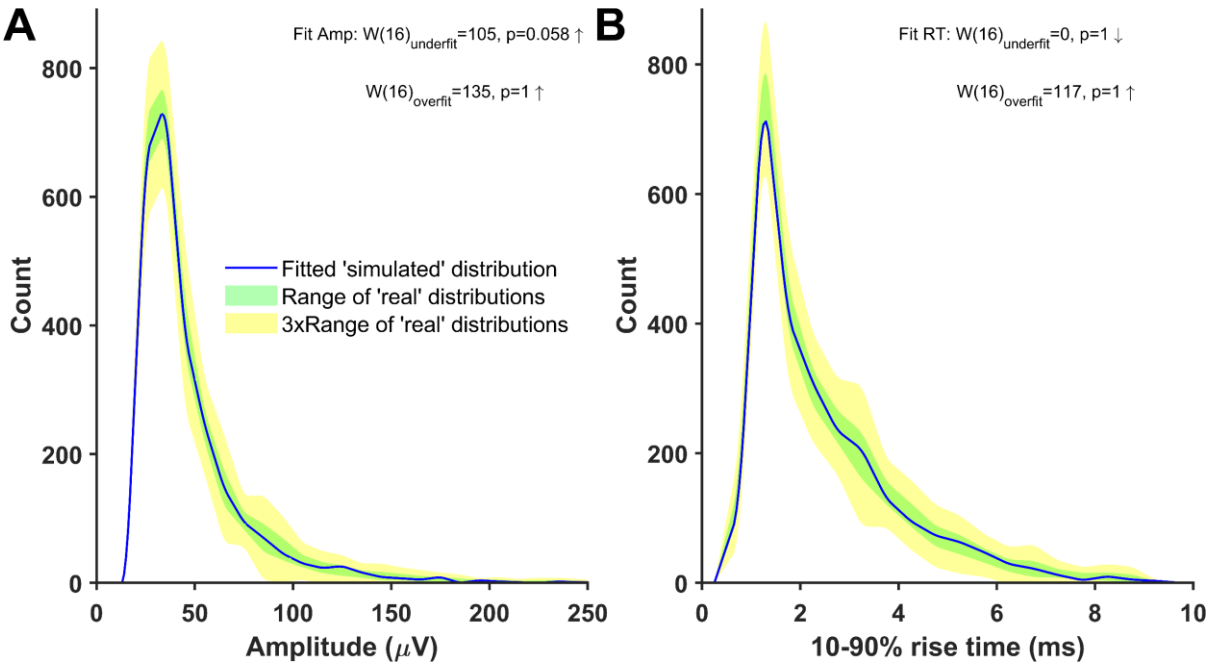

Figure 8: Distributions of mini-like events detected in a 'noise with simulated minis' voltage trace reasonably closely matching 'noise with real minis' recordings from the same cell, p106b (neocortical layer 5).

Parameters of simulated minis were controlled by the Genetic Algorithm. Up arrows indicate 'simulated' SAD > 'real' SAD; down arrows 'simulated' SAD < 'real'. The underfit test involves a comparison with the 'worst-performing' 'real' SAD (most discrepant from the others), whereas the overfit ('excellent fit') test involves a comparison with the 'best-performing' 'real' SAD (least discrepant from the others). With the underfit test (top), a fit SAD worse (bigger) than the 'real' SAD (up arrow), and $p < 0.05$ would mean the fit is rejected (not the case here: both amplitude and rise time fits (A and B) were accepted). (See Methods and Figure 6 for more details).

(A) Amplitude and (B) 10-90% rise time distributions (blue) of mini-like events detected in a 'noise with simulated minis' voltage trace, compared with 'envelopes' or bands (shaded) of all available 'real' data distributions from the neuron (taking the most extreme low and high values at each point across all the available data files recorded with both APs and IPSPs blocked).

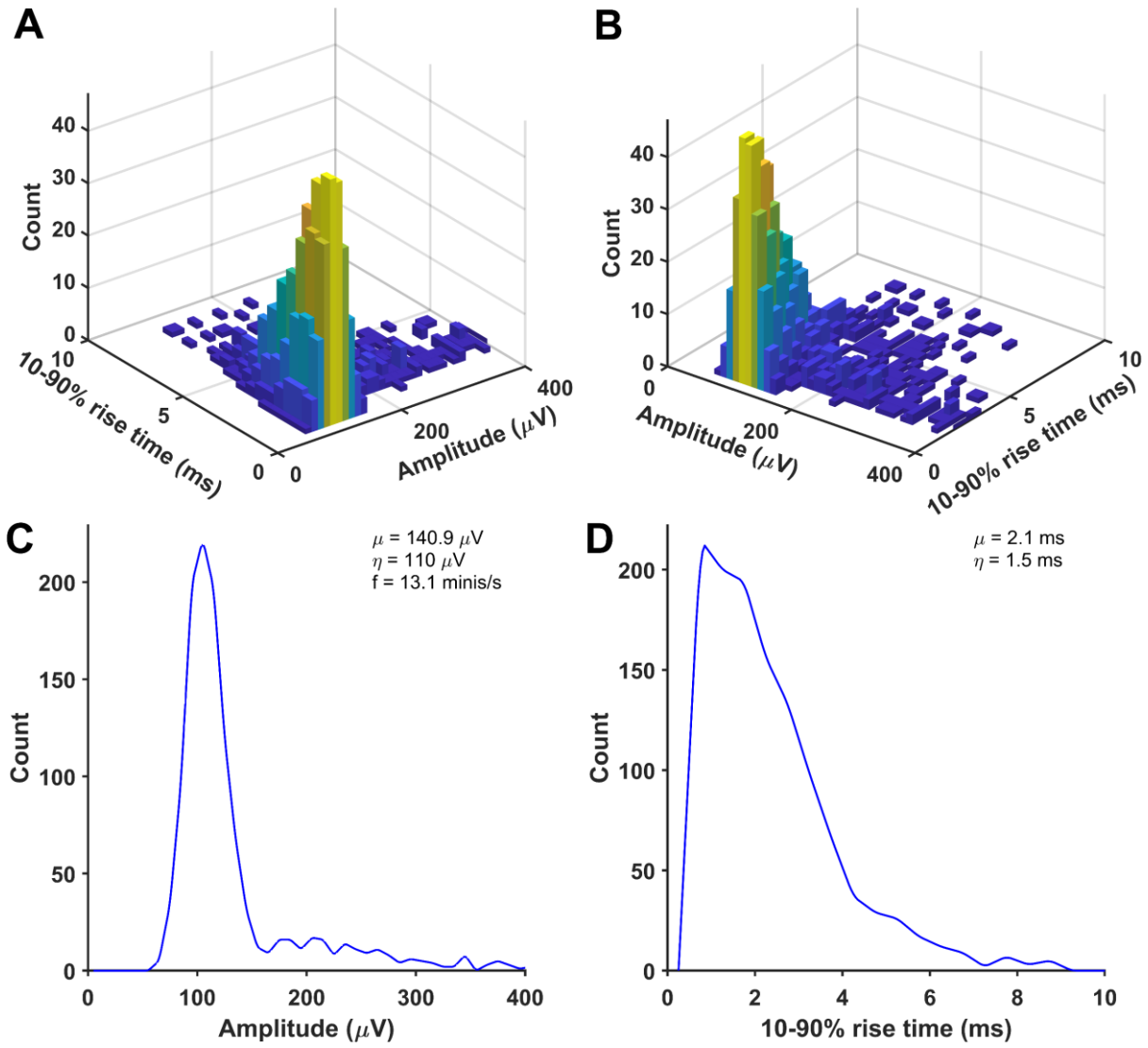

Figure 9: An example of a distribution of randomly selected simulated minis that was used to produce a close match between the distributions of detected mini-like events in a 'noise with simulated minis' voltage trace (with a 60 µV lower limit on simulated amplitudes) and a 'noise with real minis' recording, for a neocortical layer 2/3 cell (p131c).

(A) and (B) Joint amplitude and 10-90% rise time distribution of simulated minis, viewed from different angles.

(C) and (D) Corresponding 'marginal' (one-dimensional) amplitude and 10-90% rise time distributions, projected onto the axis indicated.

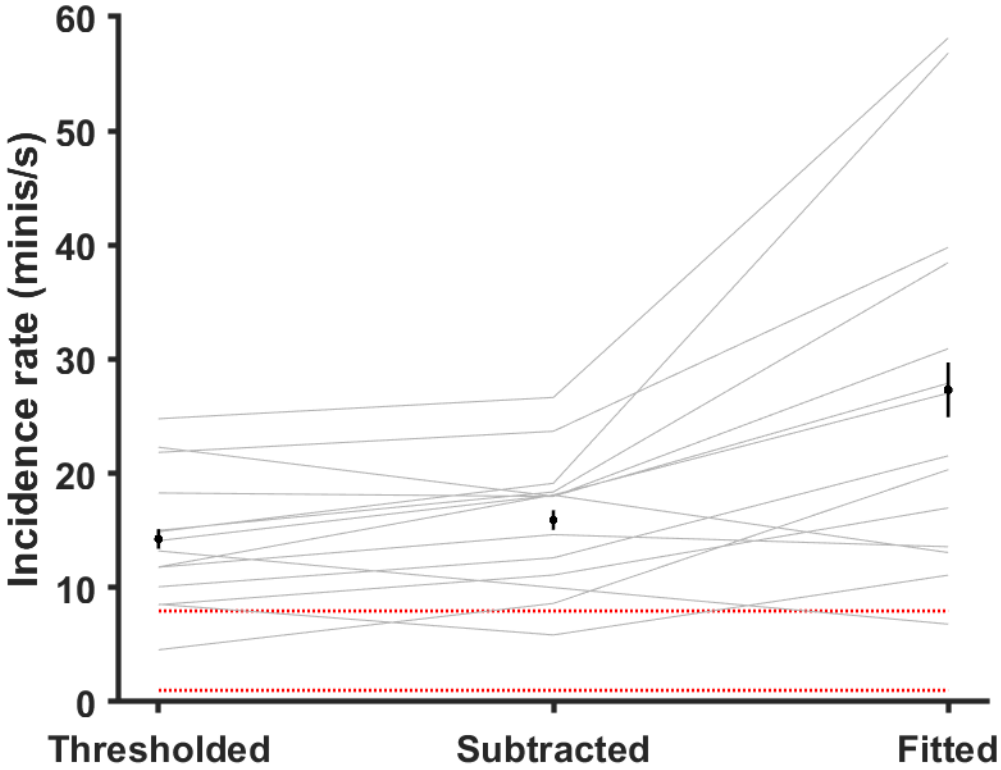

Figure 10: Estimated mEPSP incidence rates ('frequencies') using various methods (grey lines are individual cells).

'Thresholded' method: an 'unreasonably high' 80 µV detection threshold was applied to all 14 'noise with real minis' recordings so only larger events were included.

'Subtracted' method: the distribution of mini-like events in the 'noise-alone' recording was subtracted from the distribution of mini-like events in the 'noise with real minis' recording and the incidence rate estimate was based on the positive bins of the resulting distribution.

'Fitted' method: the simulated minis distribution was used to estimate a lower bound on the mEPSP incidence rate (*lowest* acceptable rate statistically consistent with the real experimental data).

Black markers and black vertical lines correspond to means and 95% confidence intervals. Red dotted lines mark the range of incidence rates typically reported in the literature; discussed in the companion article (Dervinis and Major, 2024).

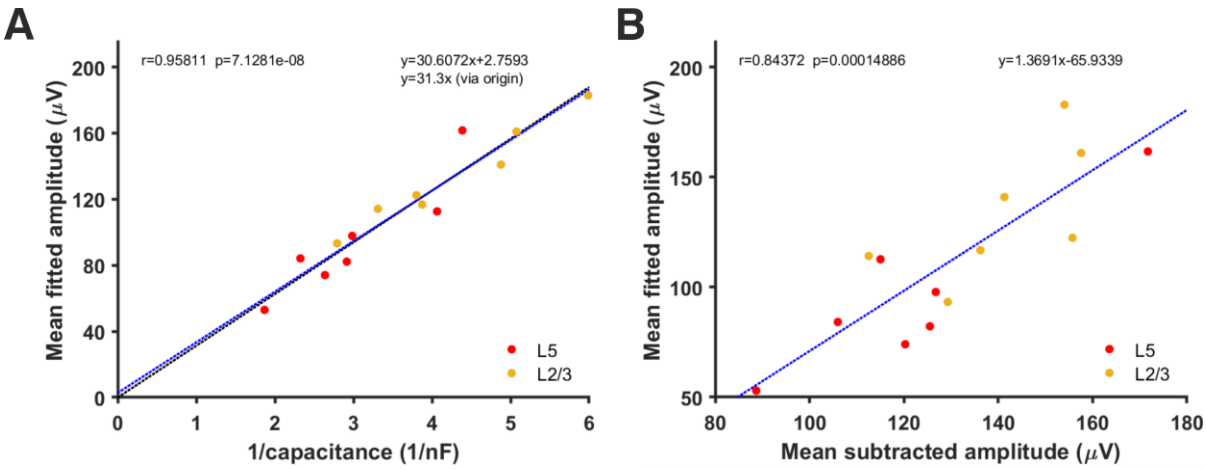

Figure 11: Relationship between each cell's inverse total membrane capacitance and its estimated mean mEPSP amplitude using simulations and fitting of minis distributions.

(A) Correlation between mean mini amplitudes from different neurons, as derived using the simulated minis distribution fitting method and the inverse of each cell's total capacitance. The blue line is the least square fit to the data while the (nearly indistinguishable) black line is the fit to the data that passes through the origin.

(B) Correlation between the mean mEPSP amplitude of each neuron estimated from 'fitting' versus 'subtracting' (the corresponding noise histogram, as in Figure 7).

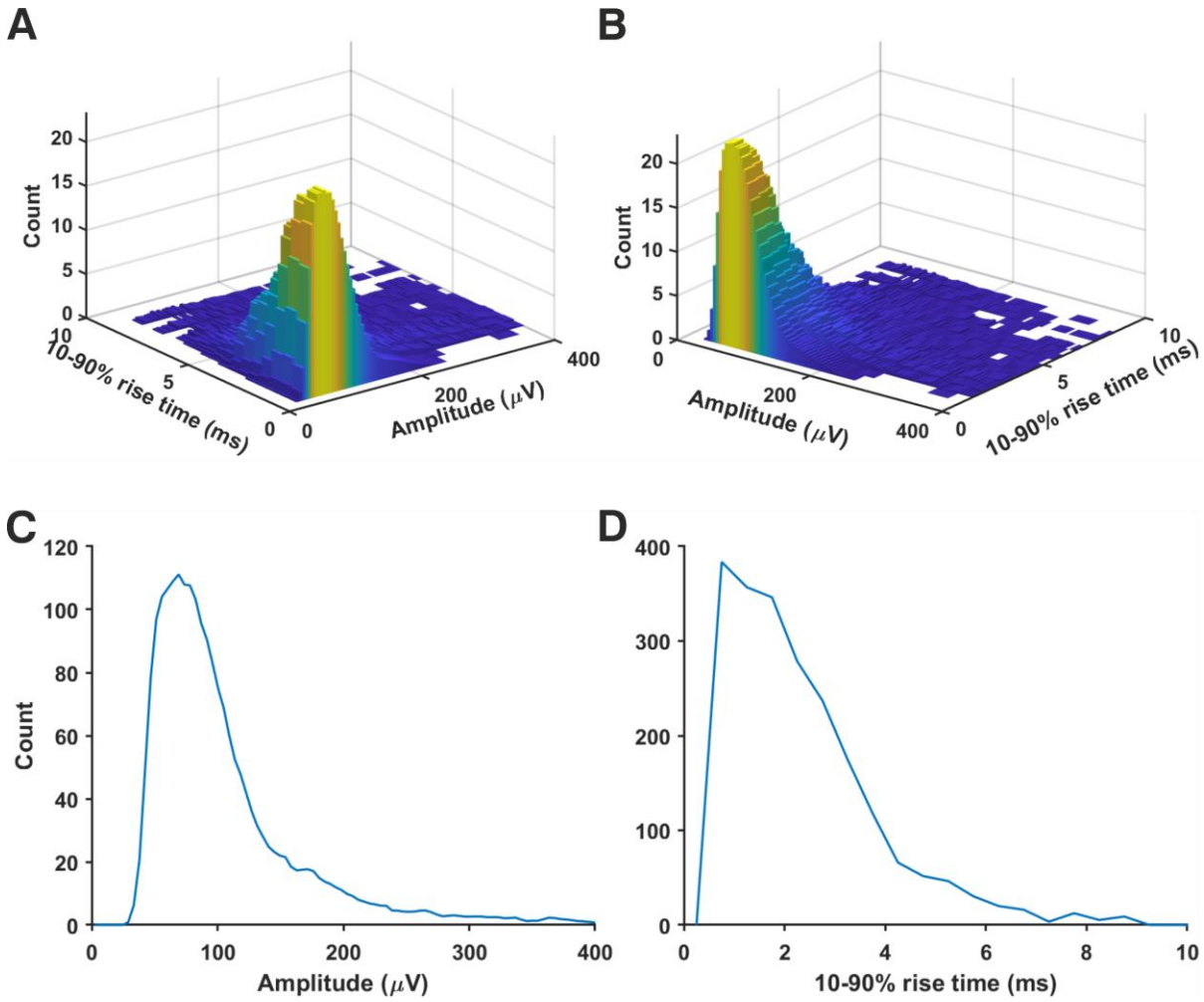

Figure 12: Generic 'averaged' mEPSP distribution from rat (somatosensory) neocortical pyramidal neurons.

Distributions resulting from all 14 recordings were averaged. All mini amplitudes were first normalised by the means of their respective source distributions, then multiplied by the average of the average amplitudes (114.1 ± 5.5 μV) across all the neurons analysed.

(A) A joint amplitude and 10-90% rise time distribution of simulated minis.

(B) The same distribution but viewed from a different angle.

(C) 'Marginal' (1-dimensional) amplitude distribution projected from the above distribution onto the amplitude axis.

(D) 'Marginal' 10-90% rise time distribution.

Tables

Amp SAD ≤56th centile?	Top 50% amp SAD ≤56th centile?	Top 10% amp SAD ≤56th centile?	Top 2% amp SAD ≤56th centile?	Top 50% amp SSD ≤0?	Top 10% amp SSD ≤0?	Top 2% amp SSD ≤0?	RT SAD ≤56th centile?	Joint SAD ≤56th centile?	Amp MAD ≤56th centile?	Top 50% amp MAD ≤56th centile?	Top 10% amp MAD ≤56th centile?	Top 2% amp MAD ≤56th centile?	RT MAD ≤56th centile?	Joint MAD ≤56th centile?
…	…	…	…	…	…	…	…	…	…	…	…	…	…	…
Yes	Yes	Yes	Yes	No	No	No	Yes	Yes	Yes	Yes	Yes	Yes	Yes	Yes
Yes	Yes	Yes	Yes	Yes	Yes	Yes	Yes	Yes	Yes	Yes	Yes	Yes	Yes	Yes
Yes	Yes	Yes	Yes	No	No	No	Yes	Yes	Yes	Yes	Yes	Yes	Yes	Yes
No	No	No	No	Yes	No	No	Yes	Yes	Yes	No	No	No	Yes	Yes
No	Yes	No	No	No	Yes	Yes	Yes	Yes	Yes	Yes	No	No	Yes	No
Yes	Yes	Yes	Yes	No	No	No	No	Yes	Yes	Yes	Yes	Yes	No	Yes
…	…	…	…	…	…	…	…	…	…	…	…	…	…	…

Table 1: Failed hypothetical attempt to use 56th centile as a basis for the combined '15-score 50th centile'.

The table shows a representative portion of a much bigger table illustrating a hypothetical scenario where the 15 SAD, SSD, and MAD scores are arranged in columns and rows corresponding to different two-file comparisons (many other comparisons are above and below those portrayed for the sake of the argument). SAD, SSD, and MAD scores are calculated by subtracting one file distribution from another (see the text for a detailed explanation). In this example, only *one* file comparison pair (green; 1/6 = 16.7%; row shaded in grey) satisfies the condition of having *all* its actual between-file SAD, SSD, and MAD values equal or below their respective 56th centile (across all comparison pairs - a unique value applying all the way down each column) – i.e. *simultaneously* in *all* columns. Therefore, the 56th percentile of each SAD, SSD, and MAD score would be too small to serve as the basis for the composite, joint or combined '15-score 50th centile': we need *half* the rows to be green, i.e. to pass the test.

Amp SAD ≤90th centile?	Top 50% amp SAD ≤90th centile?	Top 10% amp SAD ≤90th centile?	Top 2% amp SAD ≤90th centile?	Top 50% amp SSD ≤0?	Top 10% amp SSD ≤0?	Top 2% amp SSD ≤0?	RT SAD ≤90th centile?	Joint SAD ≤90th centile?	Amp MAD ≤90th centile?	Top 50% amp MAD ≤90th centile?	Top 10% amp MAD ≤90th centile?	Top 2% amp MAD ≤90th centile?	RT MAD ≤90th centile?	Joint MAD ≤90th centile?
…	…	…	…	…	…	…	…	…	…	…	…	…	…	…
Yes	Yes	Yes	Yes	Yes	Yes	Yes	Yes	Yes	Yes	Yes	No	No	No	Yes
Yes	Yes	Yes	Yes	Yes	Yes	Yes	Yes	Yes	Yes	Yes	Yes	Yes	Yes	Yes
Yes	Yes	Yes	Yes	Yes	Yes	Yes	Yes	Yes	Yes	Yes	Yes	Yes	Yes	Yes
Yes	Yes	Yes	Yes	Yes	Yes	Yes	Yes	Yes	Yes	Yes	Yes	Yes	Yes	No
Yes	Yes	Yes	Yes	Yes	Yes	Yes	Yes	Yes	Yes	Yes	Yes	Yes	No	No
Yes	Yes	Yes	Yes	Yes	Yes	Yes	Yes	Yes	Yes	Yes	Yes	Yes	Yes	Yes
…	…	…	…	…	…	…	…	…	…	…	…	…	…	…

Table 2: Using 90th SAD centile as a basis for the combined '15-score 50th centile'.

The table shows another example where the 15 SAD, SSD, and MAD scores are arranged in columns and rows correspond to different two-file comparisons. SAD, SSD, and MAD scores are calculated by subtracting one file distribution from another (see the text for a detailed explanation). Now *three* of the six file pairings (*half* of them: green; rows shaded in grey) satisfy the condition of having *all* their between-file SAD, SSD, and MAD scores equal or below their respective 90th centiles (across all comparison pairs - a unique number applying all the way down each column). Therefore, the 90th percentile works as the basis for the combined '15-score 50th centile'. Higher than 90 leads to more than half and lower than 90 leads to fewer than half of possible file pairs 'passing' all 15 tests simultaneously.

1143 # Supplementary Figures

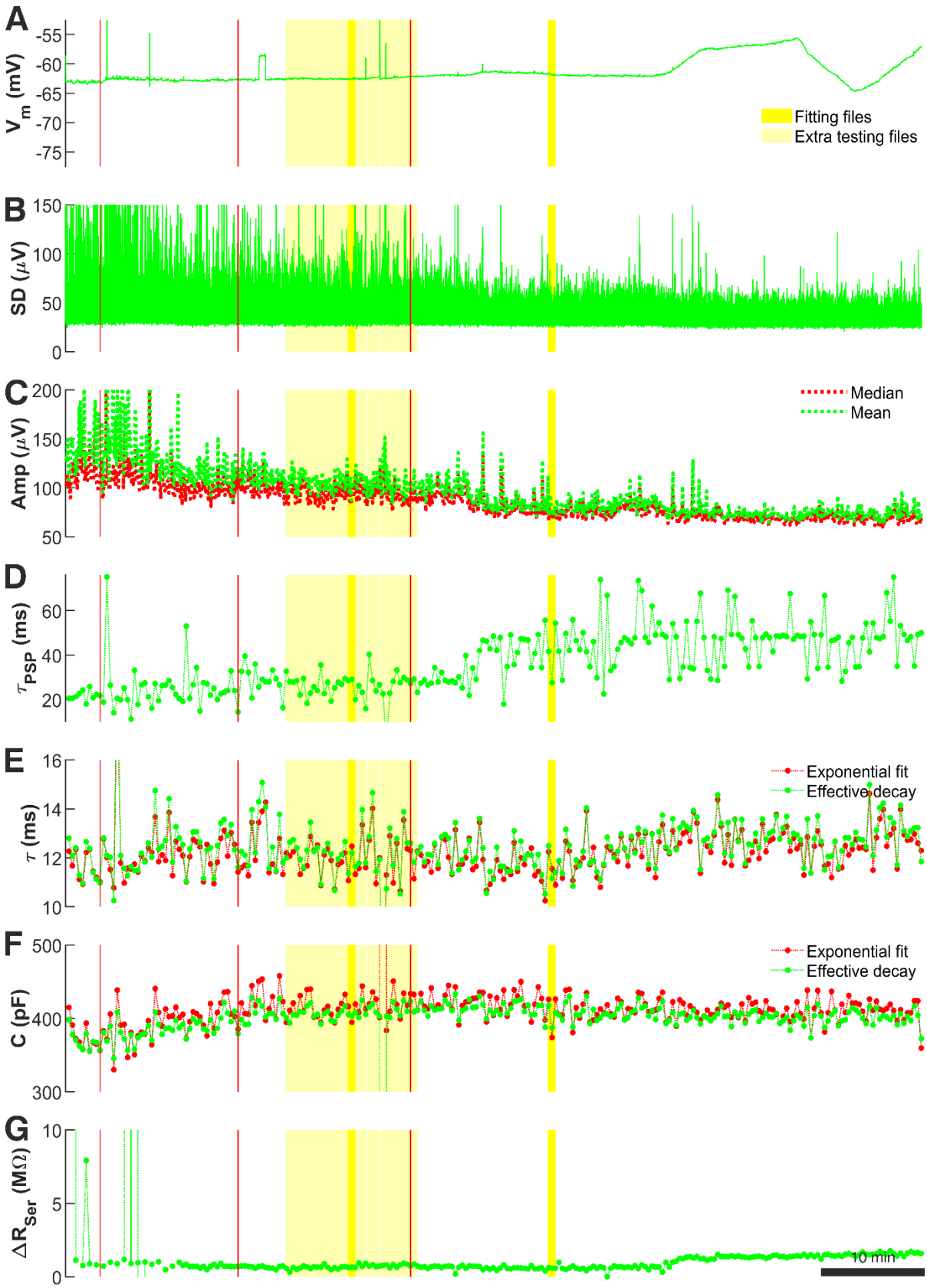

Supplementary Figure 1: Cell p106b (layer 5). Recording quality measures used to select 'noise with minis' and 'noise-alone' sweeps.

1147 (A) Baseline V_m across entire recording (excluding stimulation pulse periods); duration 4960 s. Red

1148 lines and shaded yellow regions and Panels B-G as for Figure 2.

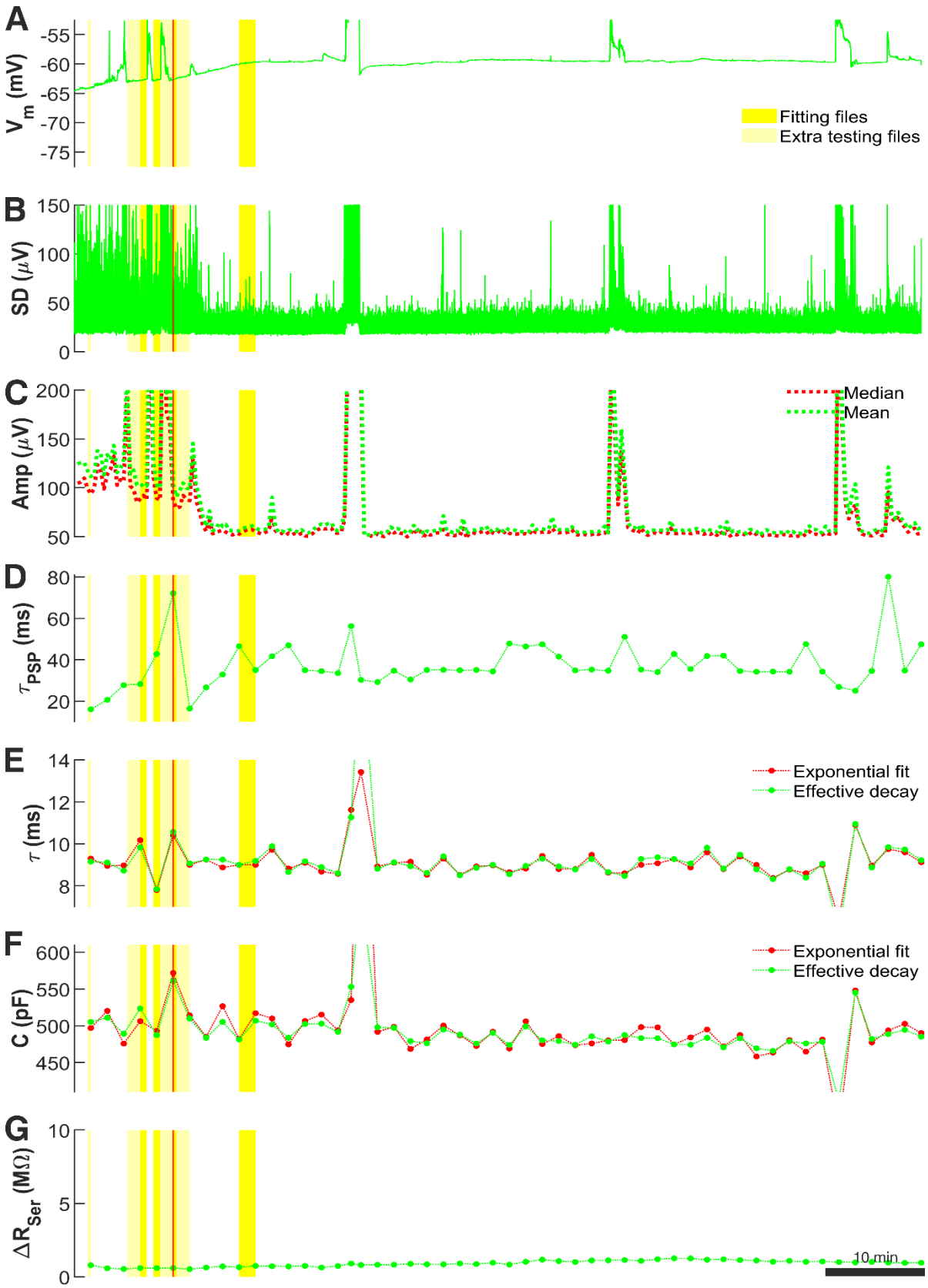

Supplementary Figure 2: Cell p108a (layer 5). Recording quality measures used to select 'noise with minis' and 'noise-alone' sweeps.

1152 Panels A-G as for Figure 1 except for data being averaged over 100-second-long windows (5
1153 recording sweeps of 20 s each) in panels D-G. The figure shows only part of the recording following
1154 the blockade of APs with only a single red vertical time marker visible indicating the time when
1155 pharmacological EPSP blockers were infused. The total duration of the recording shown in the figure
1156 was 5140 s. Some episodes with transient recording instabilities (noise glitches) were removed from
1157 the 'noise with minis' epoch (white gaps).
1158

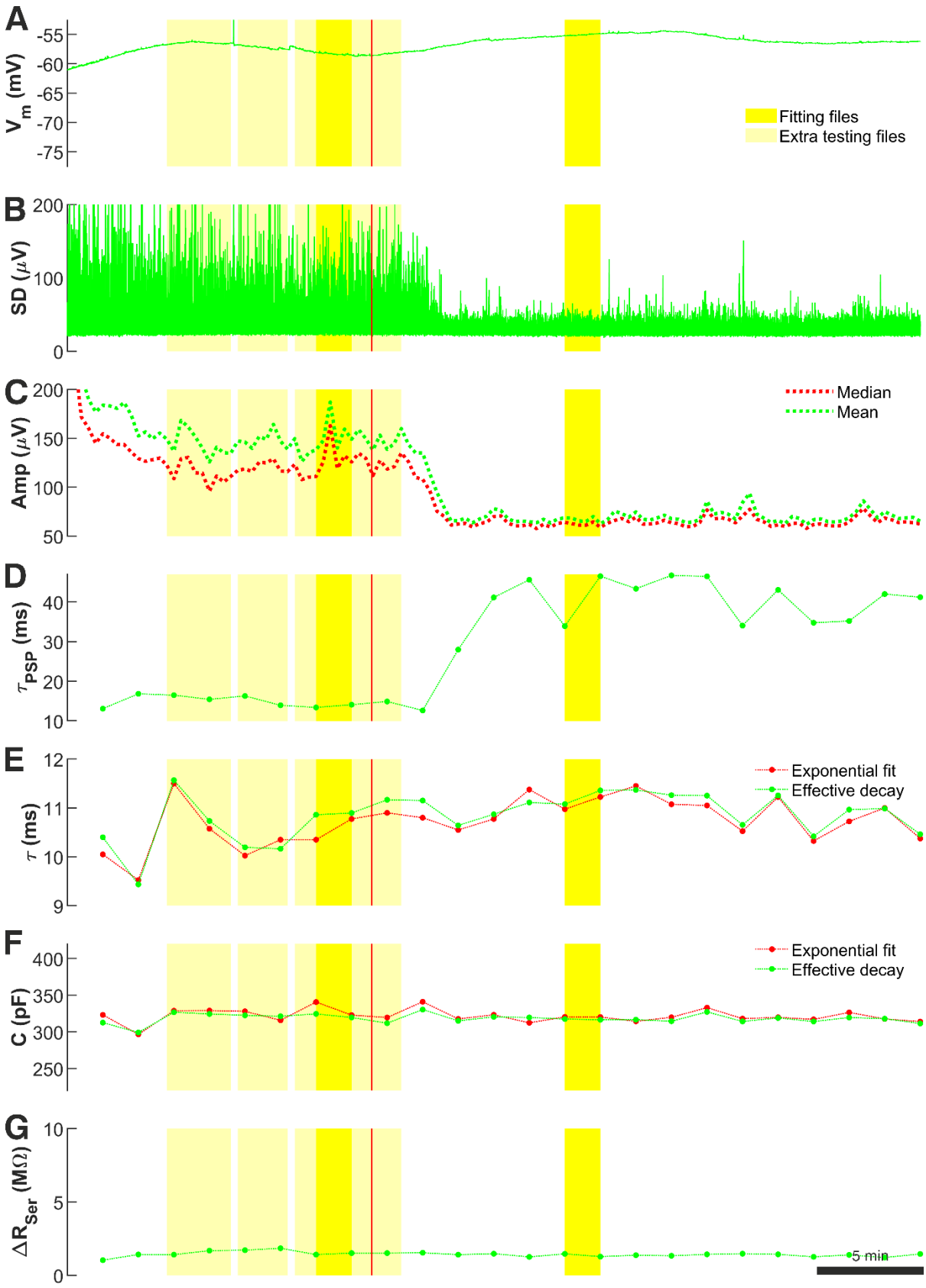

Supplementary Figure 3: Cell p108b (layer 5). Recording quality measures used to select 'noise with minis' and 'noise-alone' sweeps.

1162 Panels A-G as for Figure 2 and Supplementary Figure 2. Data were averaged over 100-second-long

1163 windows (5 recording sweeps of 20 s each) in panels D-G; duration 2400 s.

1164

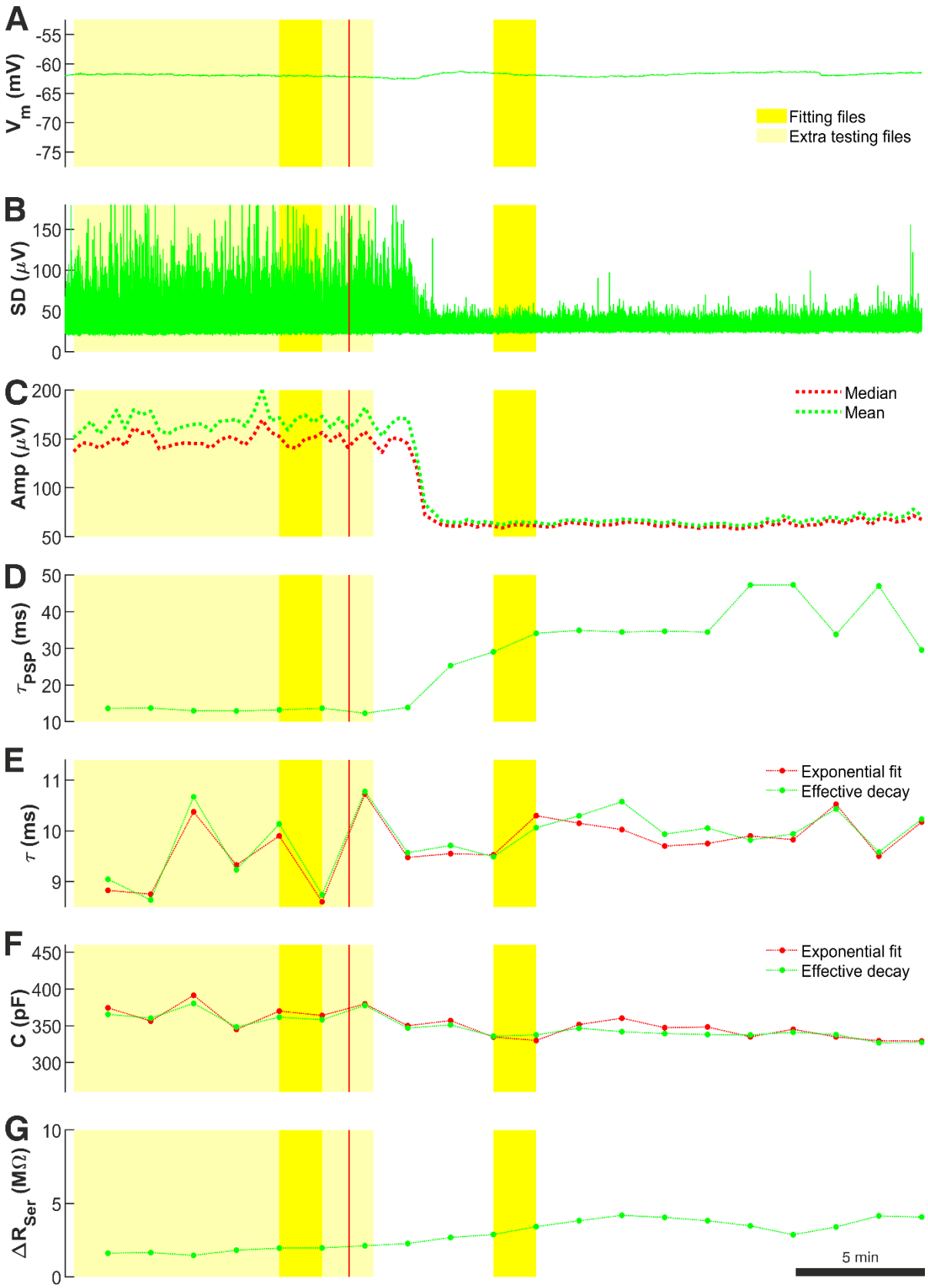

Supplementary Figure 4: Cell p108c (layer 5). Recording quality measures used to select 'noise with minis' and 'noise-alone' sweeps.

1168 Panels A-G as for Figure 2 and Supplementary Figure 2. Data were averaged over 100-second-long

1169 windows (5 recording sweeps of 20 s each) in panels D-G; duration 2000 s.

1170

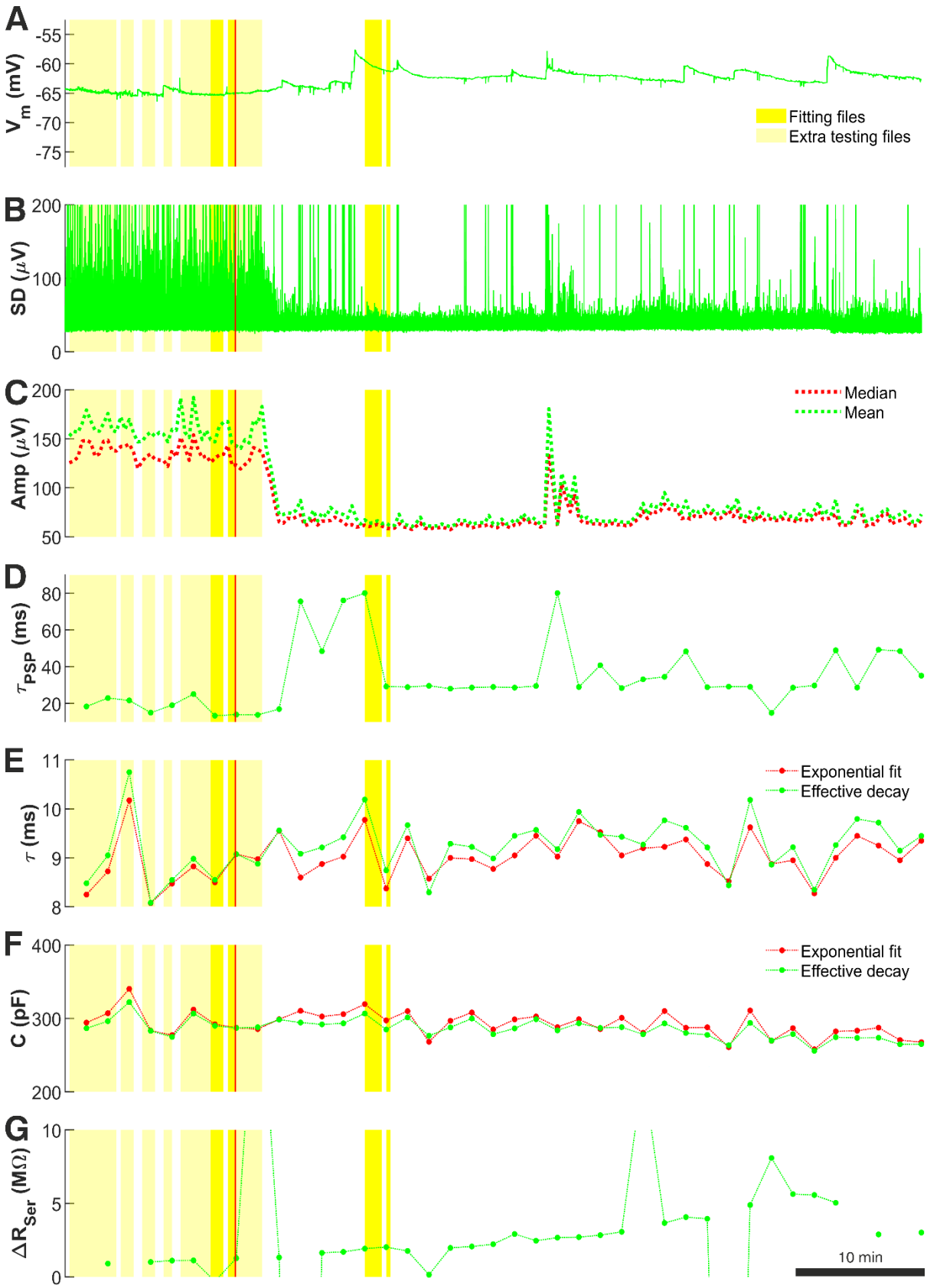

Supplementary Figure 5: Cell p120b (layer 2/3). Recording quality measures used to select 'noise with minis' and 'noise-alone' sweeps.

Panels A-G as for Figure 2 and Supplementary Figure 2. Data were averaged over 100-second-long windows (5 recording sweeps of 20 s each) in panels D-G; duration 4000 s. Some transient ‘glitchy’ extra noisy periods (due to transient recording instability) were manually excluded from the ‘noise with minis’ and ‘noise-alone’ epochs (white gaps).

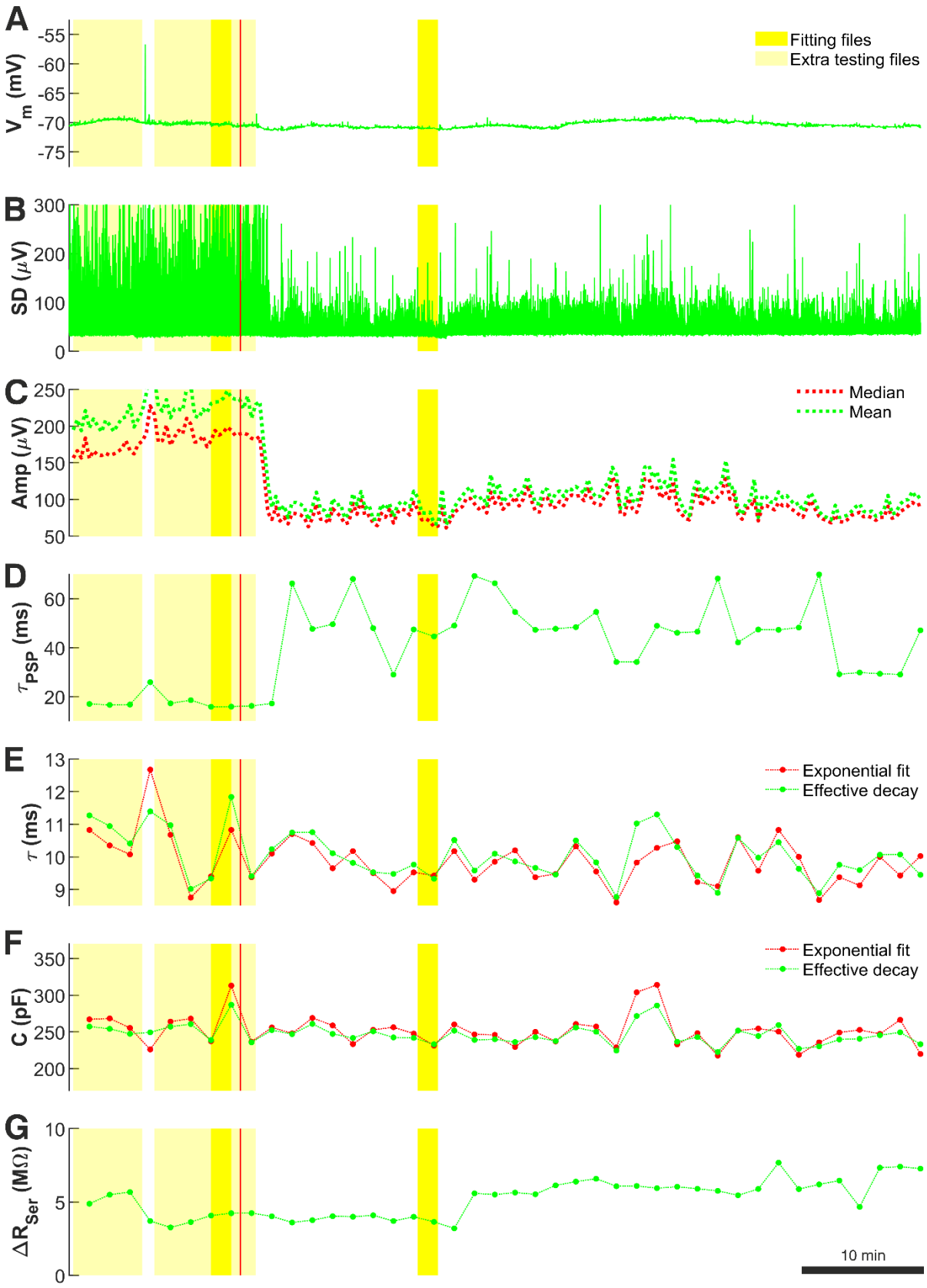

Supplementary Figure 6: Cell p122a (layer 2/3). Recording quality measures used to select 'noise with minis' and 'noise-alone' sweeps.

1182 Panels A-G as for Figure 2 and Supplementary Figure 2. Data were averaged over 100-second-long

1183 windows (5 recording sweeps of 20 s each) in panels D-G; duration 4200 s.

1184

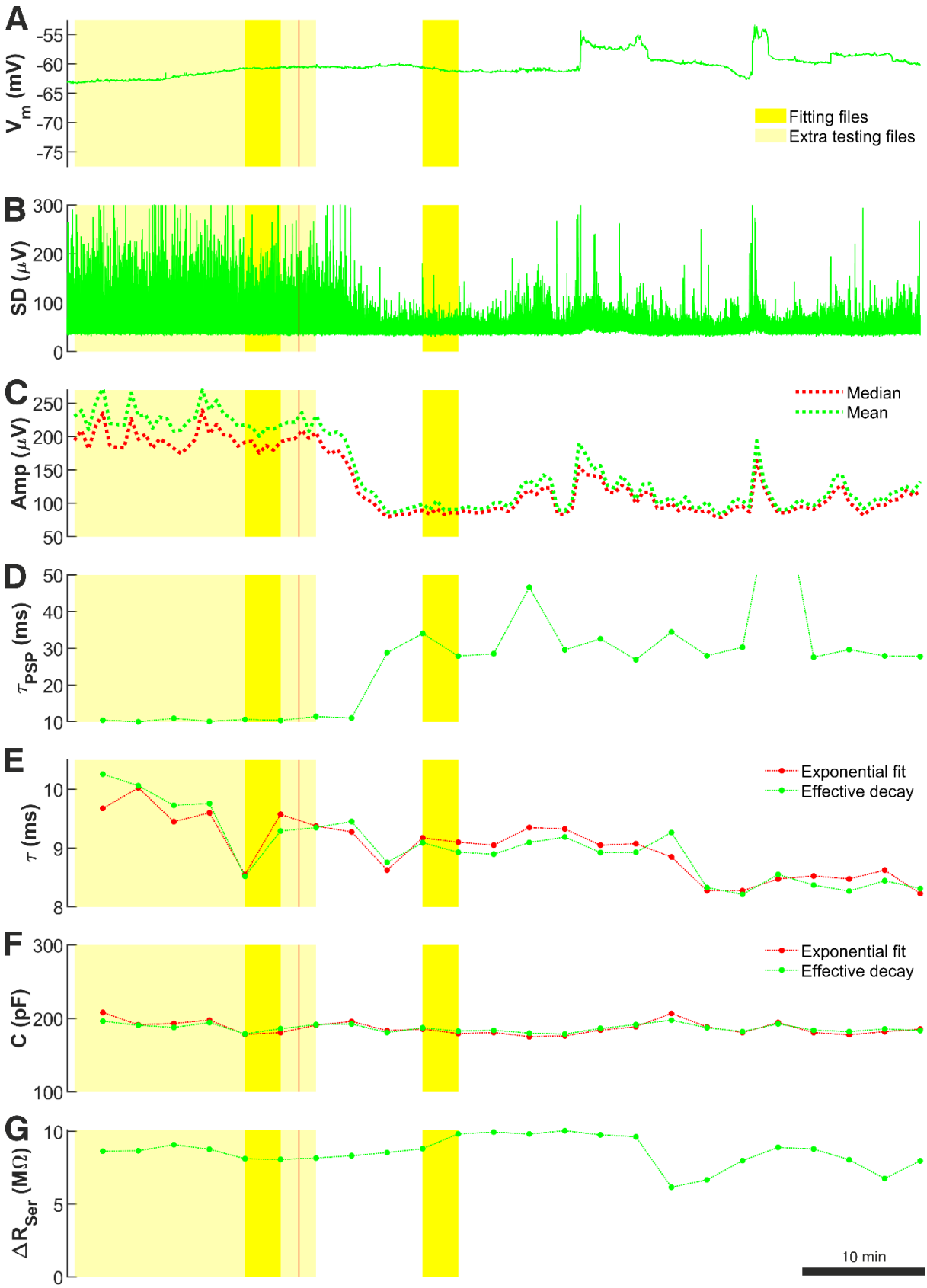

Supplementary Figure 7: Cell p124b (layer 5). Recording quality measures used to select 'noise with minis' and 'noise-alone' sweeps.

1188 Panels A-G as for Figure 2 and Supplementary Figure 2. Data were averaged over 100-second-long

1189 windows (5 recording sweeps of 20 s each) in panels D-G; duration 2400 s.

1190

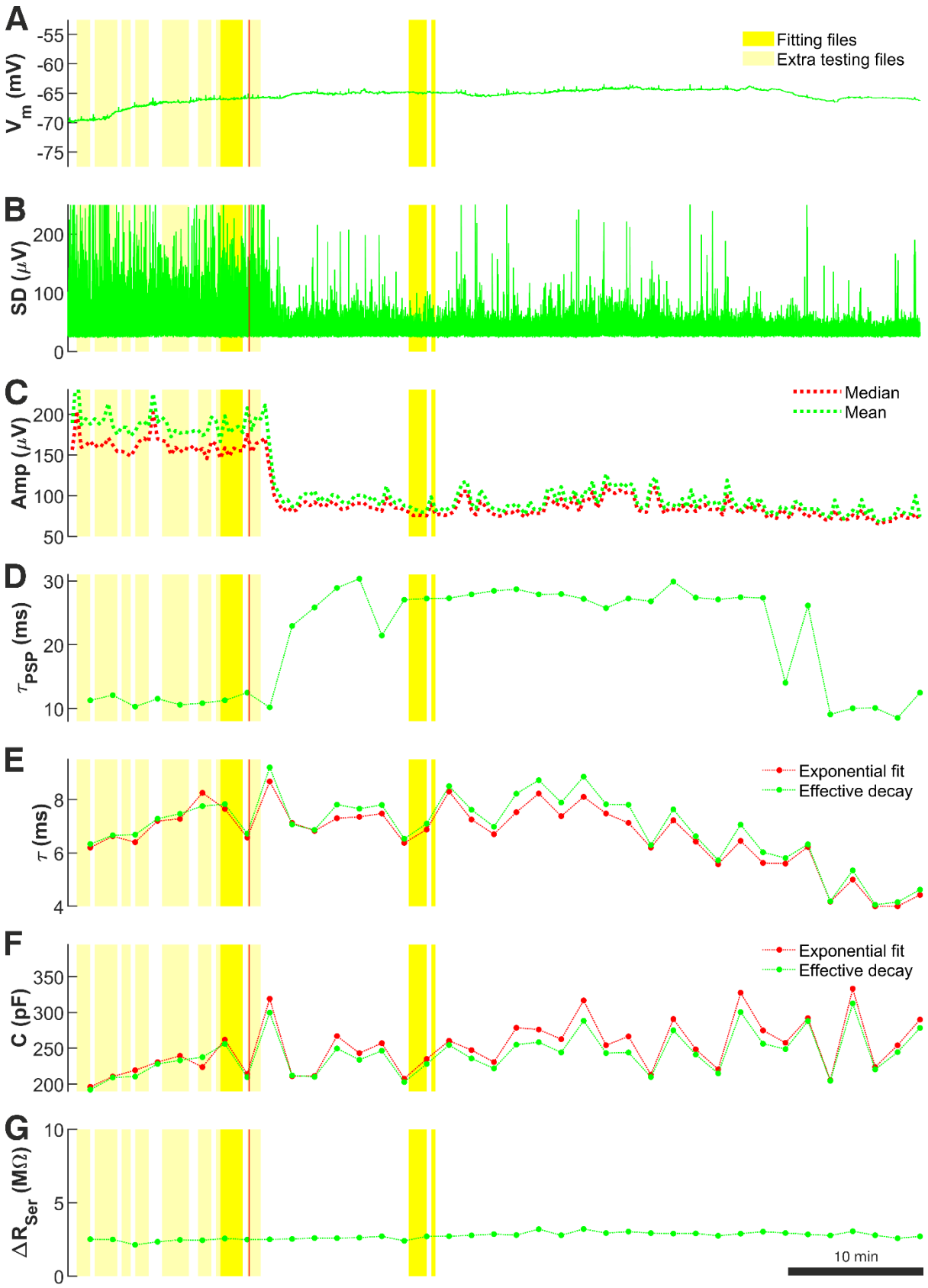

Supplementary Figure 8: Cell p125a (layer 2/3). Recording quality measures used to select 'noise with minis' and 'noise-alone' sweeps.

1194 Panels A-G as for Figure 2 and Supplementary Figure 2. Data were averaged over 100-second-long

1195 windows (5 recording sweeps of 20 s each) in panels D-G; duration 3800 s. Some transiently extra

1196 noisy data due to temporary recording instability were excluded from the ‘noise-alone’ epoch.

1197

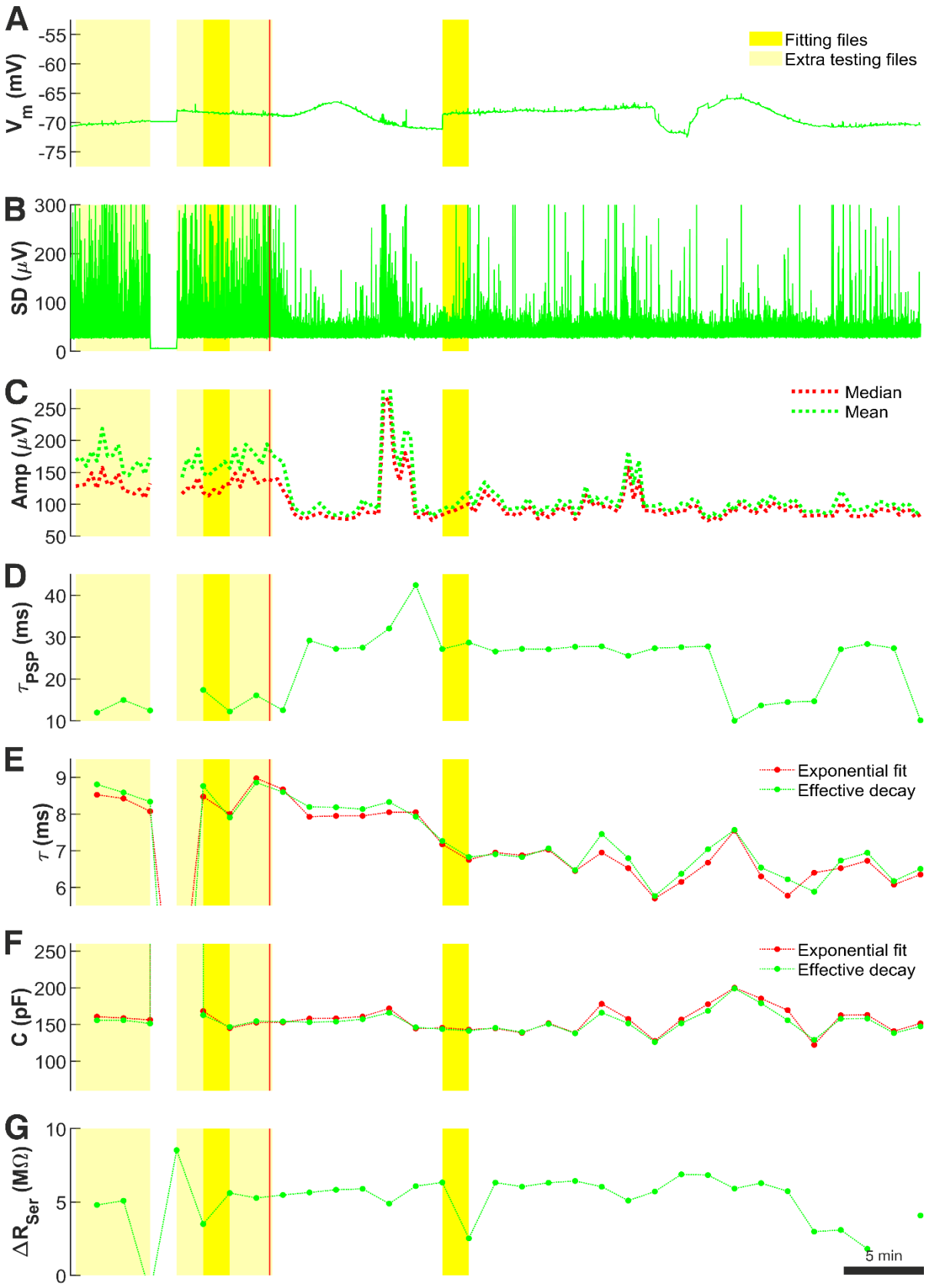

1198

1199 **Supplementary Figure 9:** Cell p127c (layer 2/3). Recording quality measures used to select 'noise

1200 with minis' and 'noise-alone' sweeps.

1201 Panels A-G as for Figure 2 and Supplementary Figure 2. Data were averaged over 100-second-long

1202 windows (5 recording sweeps of 20 s each) in panels D-G; duration 3200 s.

1203

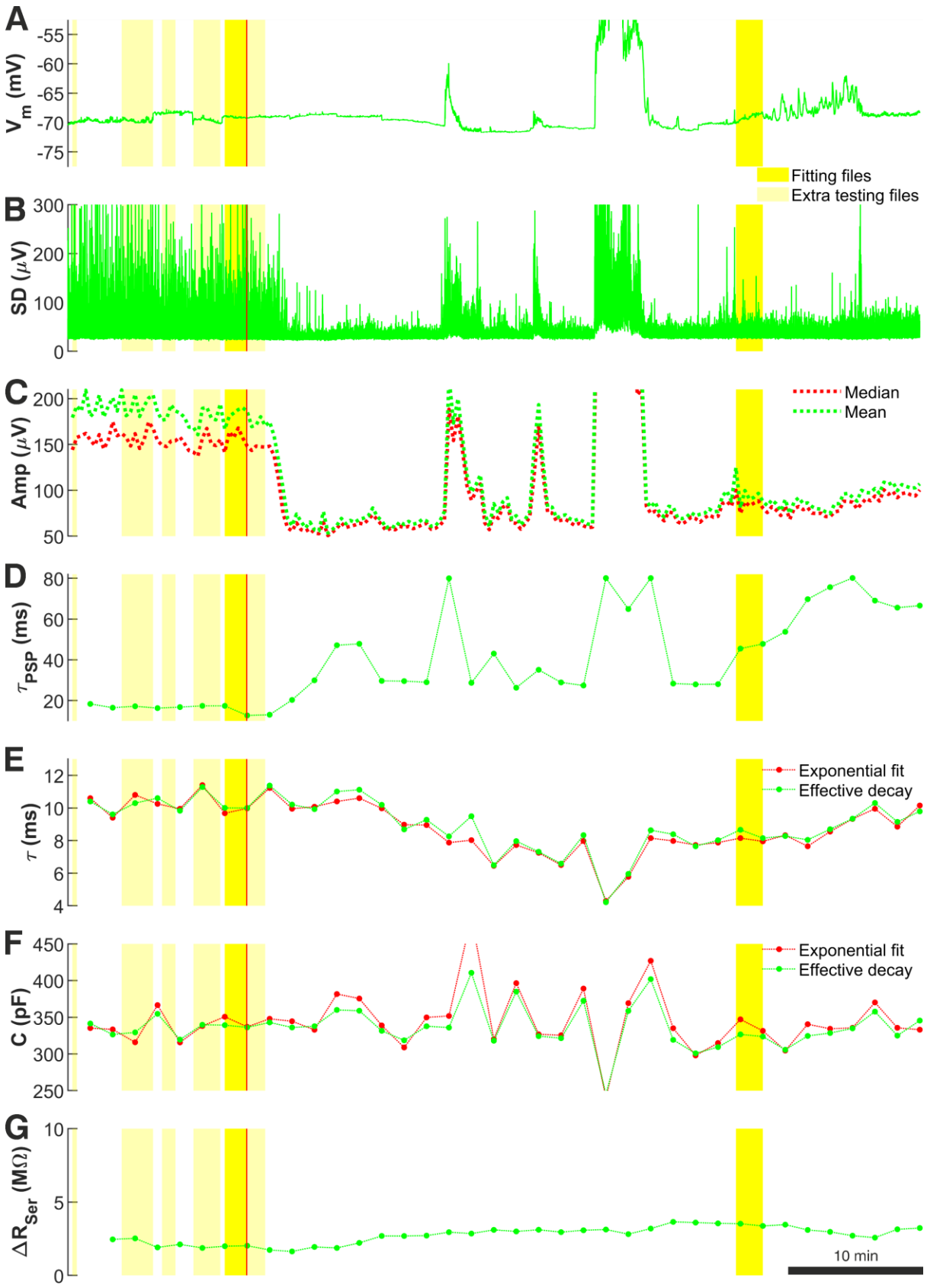

Supplementary Figure 10: Cell p128c (layer 2/3). Recording quality measures used to select 'noise with minis' and 'noise-alone' sweeps.

1207 Panels A-G as for Figure 2 and Supplementary Figure 2. Data were averaged over 100-second-long

1208 windows (5 recording sweeps of 20 s each) in panels D-G; duration 3800 s.

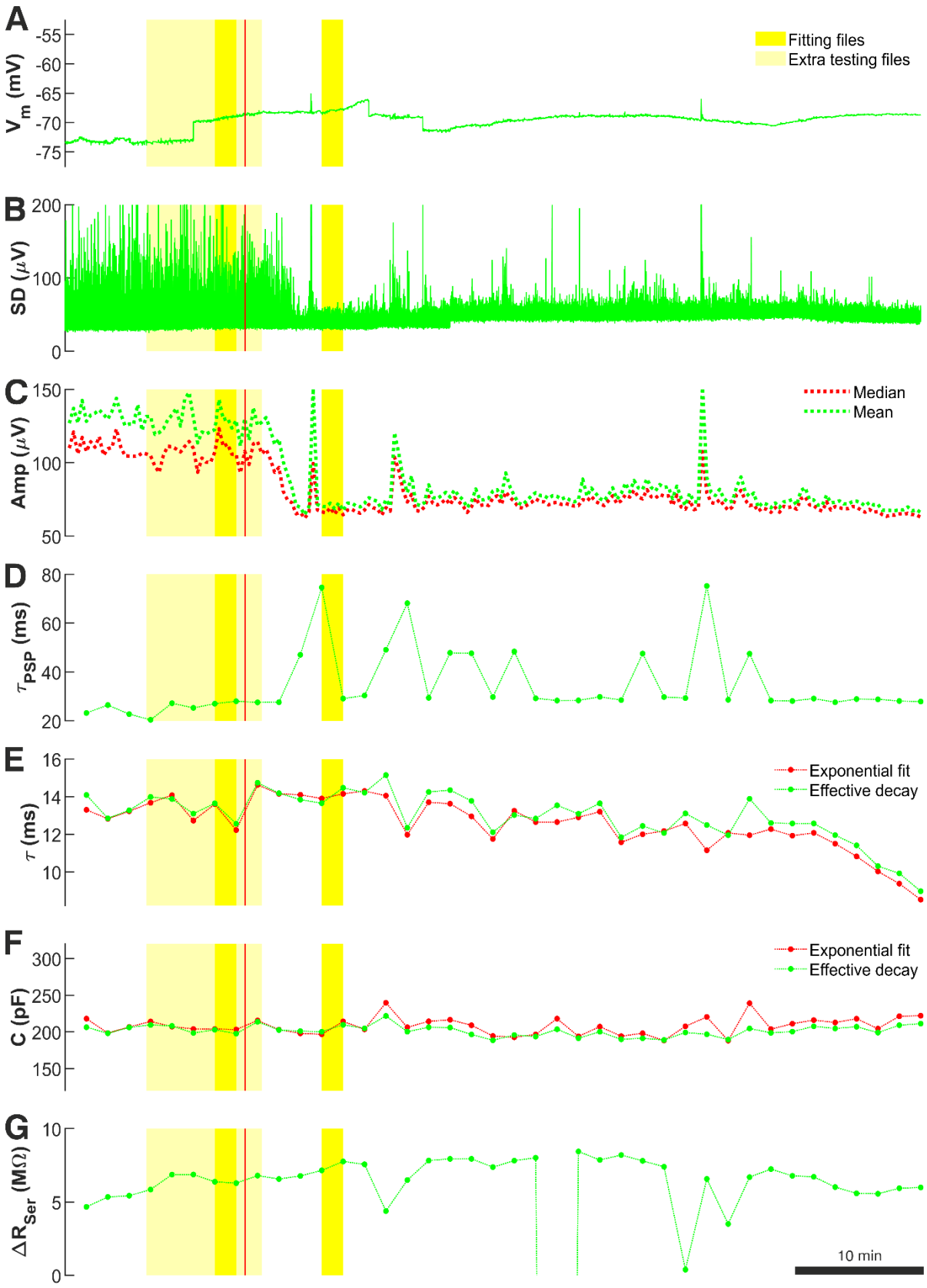

1209

1210 **Supplementary Figure 11:** Cell p129a (layer 5). Recording quality measures used to select 'noise with

1211 minis' and 'noise-alone' sweeps.

1212 Panels A-G as for Figure 2 and Supplementary Figure 2. Data were averaged over 100-second-long

1213 windows (5 recording sweeps of 20 s each) in panels D-G; duration 4000 s.

1214

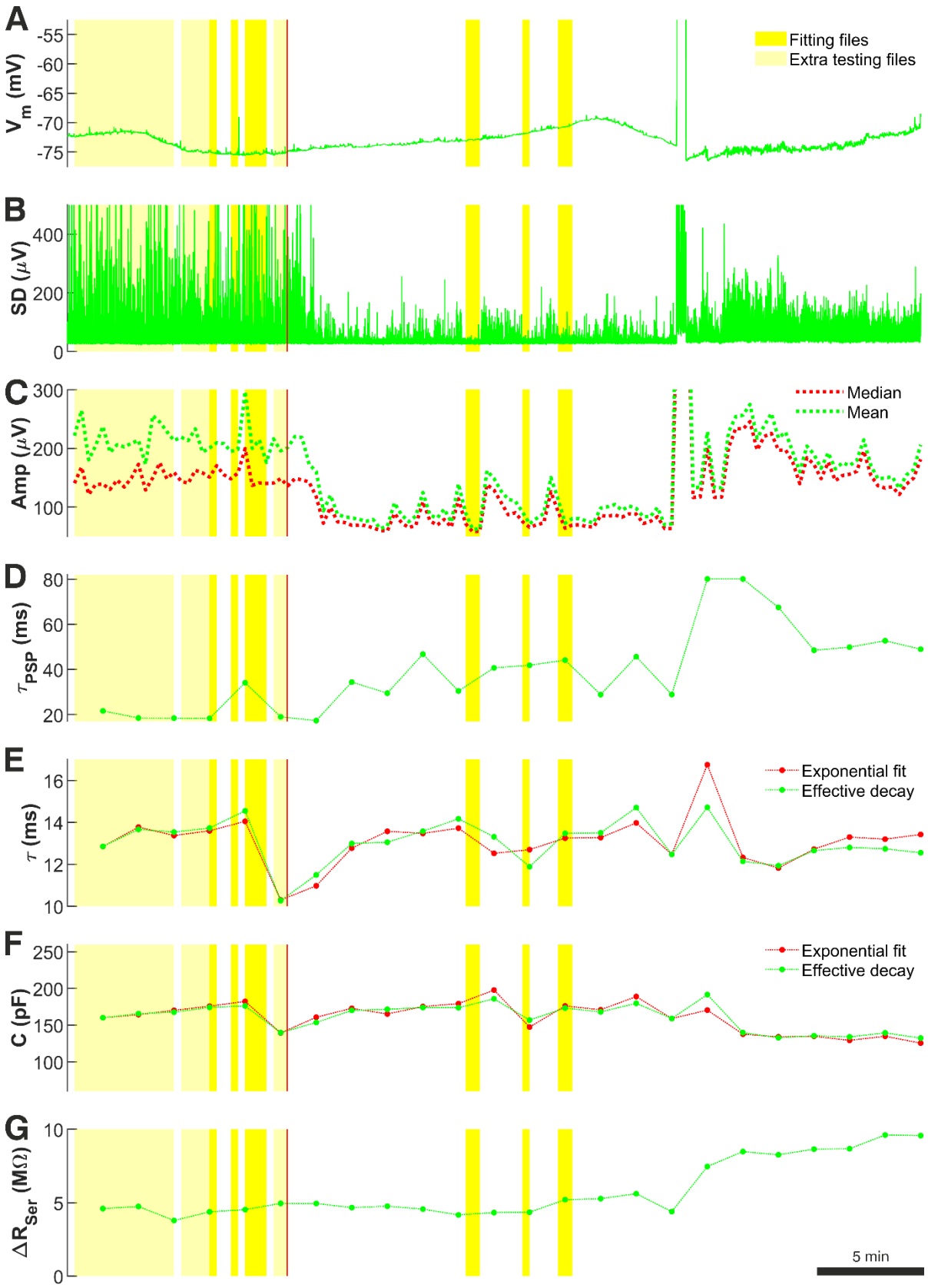

Supplementary Figure 12: Cell p131a (layer 2/3). Recording quality measures used to select 'noise with minis' and 'noise-alone' sweeps.

1218 Panels A-G as for Figure 2 and Supplementary Figure 2. Data were averaged over 100-second-long

1219 windows (5 recording sweeps of 20 s each) in panels D-G; duration 2400 s. Fit epoch is fragmented

1220 due to noisy segments, with transient recording instability, being excluded.

1221

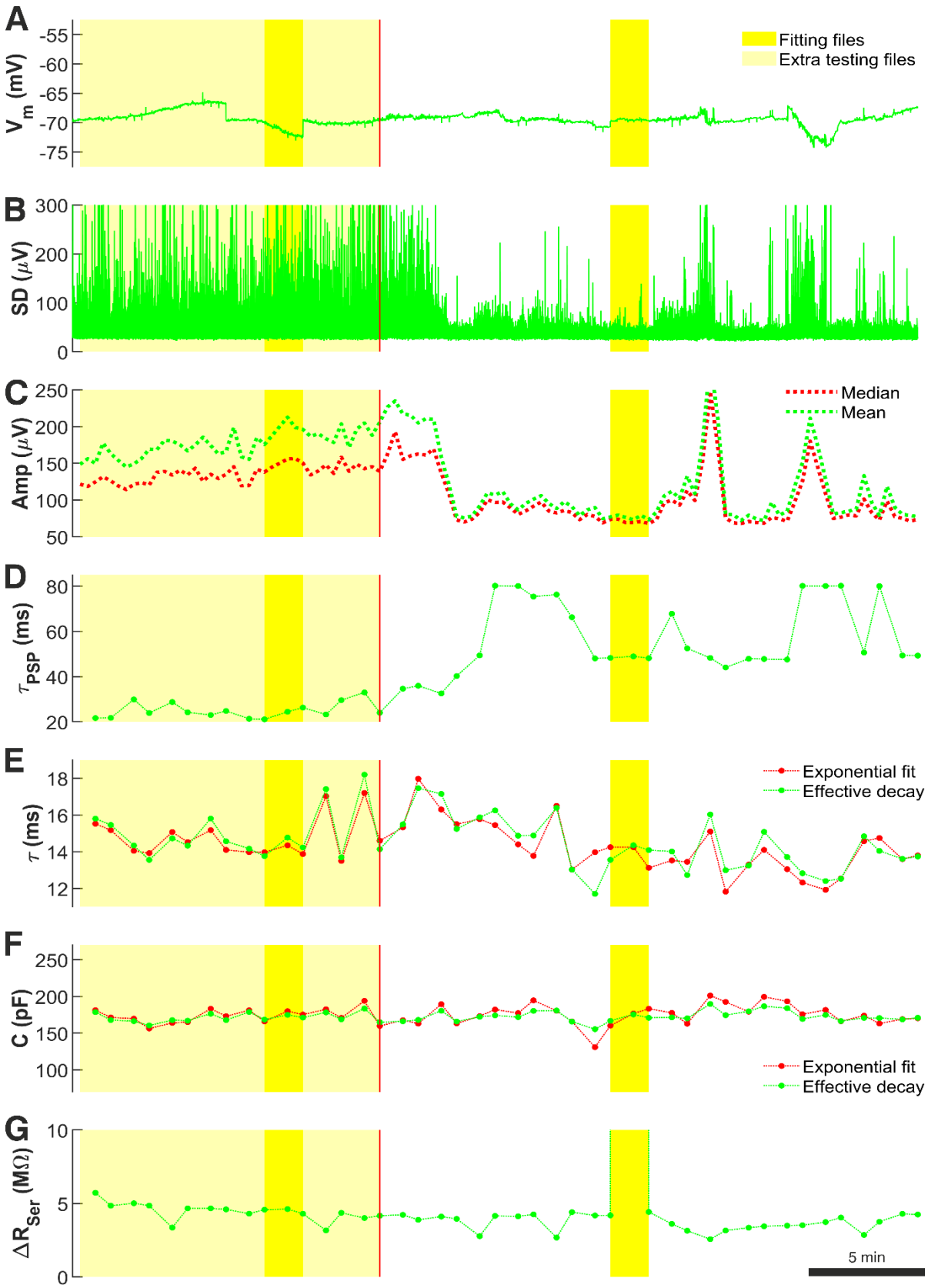

Supplementary Figure 13: Cell p131c (layer 2/3). Recording quality measures used to select 'noise with minis' and 'noise-alone' sweeps.

1225 Panels A-G as for Figure 2 and Supplementary Figure 2. Data were averaged over 100-second-long

1226 windows (5 recording sweeps of 20 s each) in panels D-G; duration 2200 s.

1227

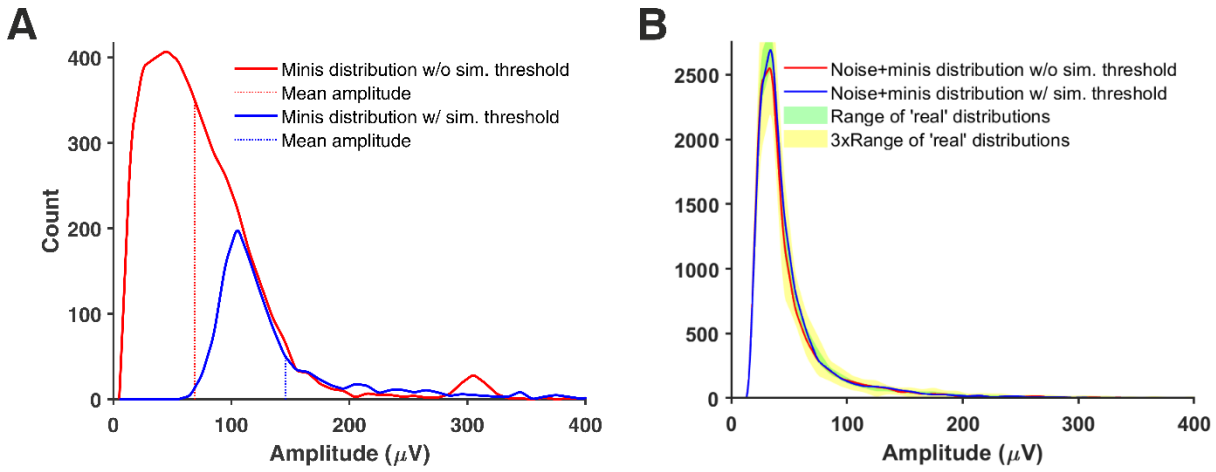

Supplementary figure 14: Non-uniqueness of simulated minis distributions.

(A) Two amplitude distributions of simulated minis events generated by the GA using a lower limit on simulated amplitudes of 10 µV (red histogram; termed as without simulation threshold) or 60 µV simulation threshold (blue histogram).

(B) Distributions of mini-like events detected in a ’noise with simulated minis’ voltage traces corresponding to the two minis source distributions in (A). Event histograms are shown superimposed on the full range of ‘real’ (‘noise with real minis’) distributions. The two distributions clearly fall within the range of ‘real’ distributions albeit being generated by two very different source distributions. Recordings obtained from cell p131c (layer 2/3).

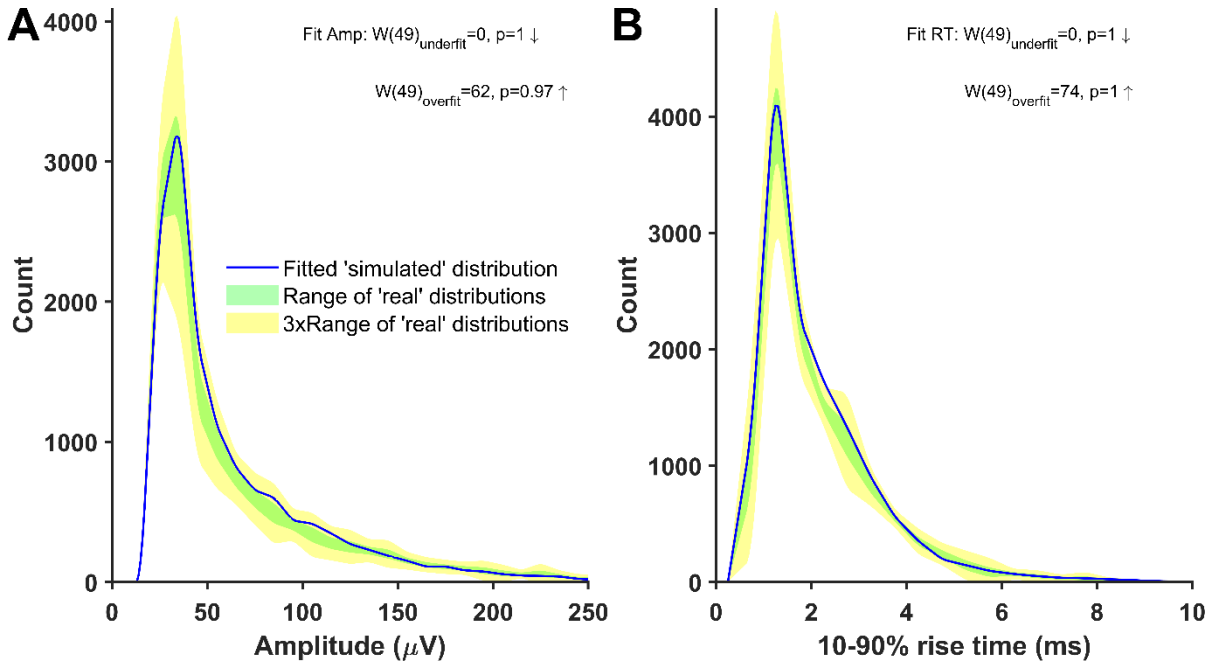

Supplementary figure 15: Distributions of mini-like events detected in a ’noise with simulated minis’ voltage trace that closely matched ‘noise with real minis‘ recordings and passed statistical good fit tests, i.e. did not ‘fail’ the poor fit (underfit) unidirectional tests (it could not be ‘picked out’ either objectively or ‘double-blind’ from the ‘noise with real minis’ distributions found with the same detection parameters).

Parameters of simulated minis were controlled by the GA; ’noise-alone’ recording obtained from cell p103a (layer 5). Downward arrows indicate ‘simulated’ SAD < ‘real’ SAD. Upward arrows indicate ‘simulated’ SAD > ‘real’ SAD. The ‘underfit’ (poor fit) unidirectional test (top) involves a comparison with the ‘worst-performing’ (highest between-file) ‘real’ SAD file (most discrepant from the others; the null hypothesis is ‘simulated’ SAD does not exceed ‘real’ SAD). The ‘overfit’ unidirectional test (bottom) involves a comparison with the ‘best-performing’ (lowest between-file) ‘real’ SAD (least discrepant from the others; the null hypothesis is ‘simulated’ SAD is not smaller than ‘real’ SAD), but ‘failure’ of this test ($p < 0.05$ Bonferroni-corrected, difference not by chance) does not indicate a fit rejection.

(A) Amplitude and (B) 10-90% rise time distributions of mini-like events detected in a ’noise with simulated minis’ voltage trace (blue curve).

1256

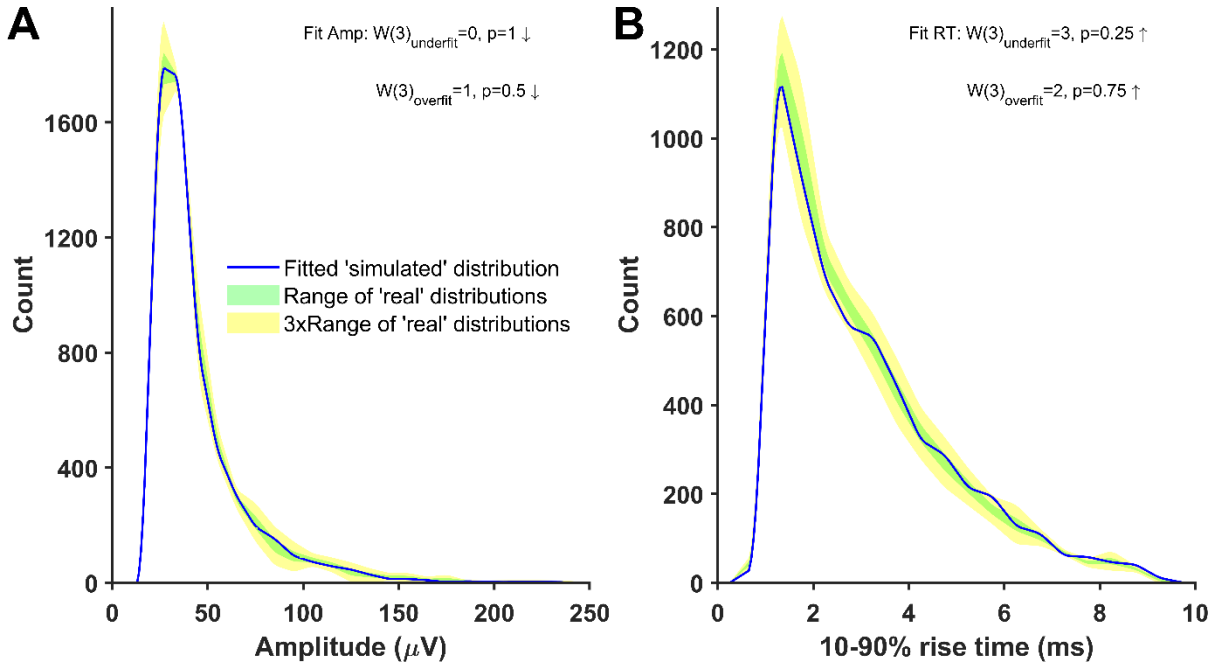

1257

1258 **Supplementary Figure 16:** Cell p108a (layer 5), distributions of mini-like events detected in a ’noise

1259 with simulated minis’ voltage trace that closely matched ‘noise with real minis‘ recordings.

1260 Parameters of simulated minis controlled by GA. Down arrow: ‘simulated’ SAD < ‘real’ SAD (up:

1261 ‘simulated’ > ‘real’; Suppl. Fig. 15).

1262

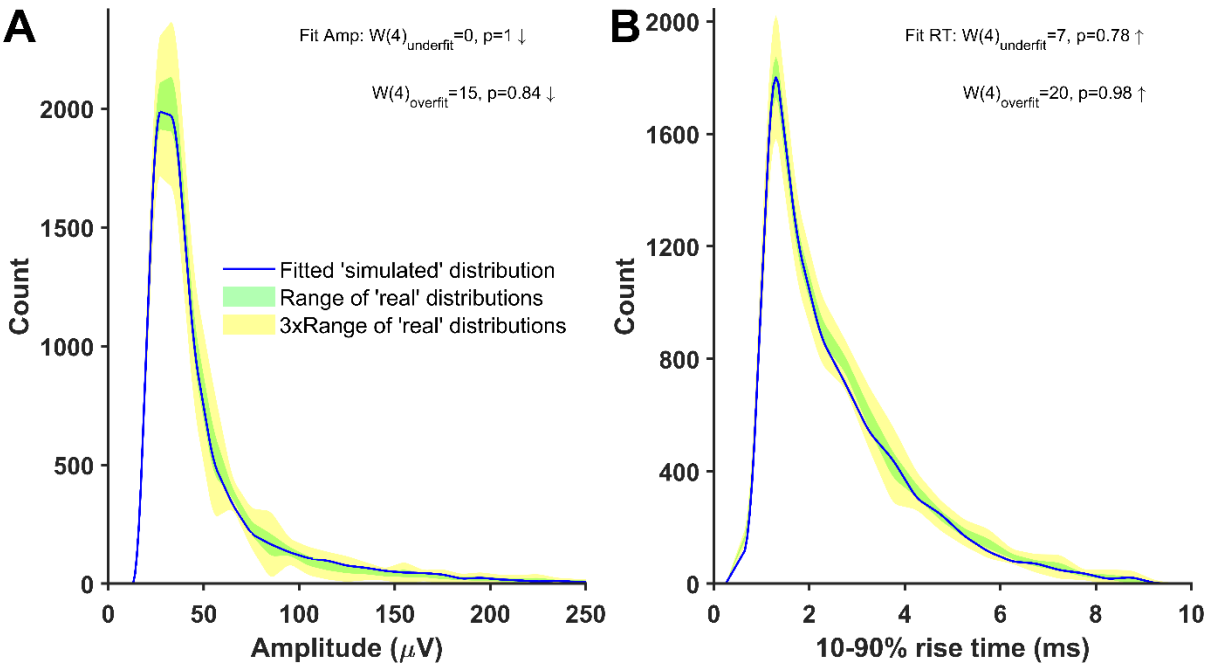

Supplementary Figure 17: Cell p108b (layer 5), distributions of mini-like events detected in a 'noise with simulated minis' voltage trace that closely matched 'noise with real minis' recordings. Parameters of simulated minis controlled by GA. Down arrow: 'simulated' SAD < 'real' SAD (up: 'simulated' > 'real'; Suppl. Fig. 15).

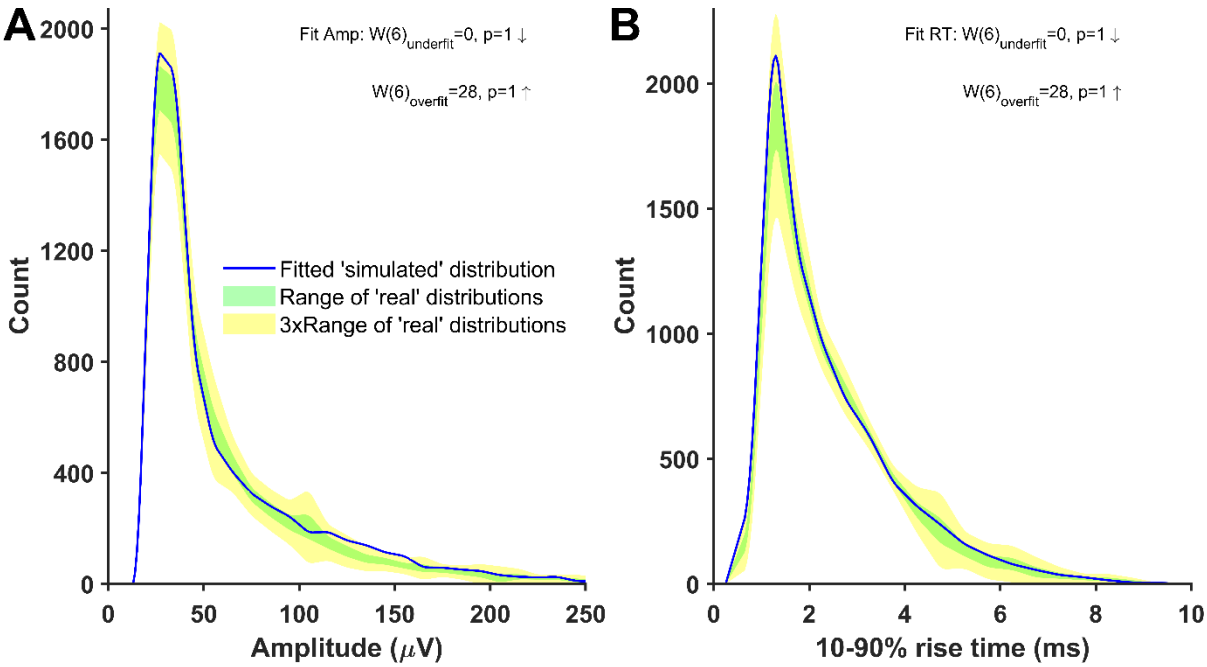

Supplementary Figure 18: Cell p108c (layer 5), distributions of mini-like events detected in a 'noise with simulated minis' voltage trace that closely matched 'noise with real minis' recordings. Parameters of simulated minis controlled by GA. Down arrow: 'simulated' SAD < 'real' SAD (up: 'simulated' > 'real'; Suppl. Fig. 15).

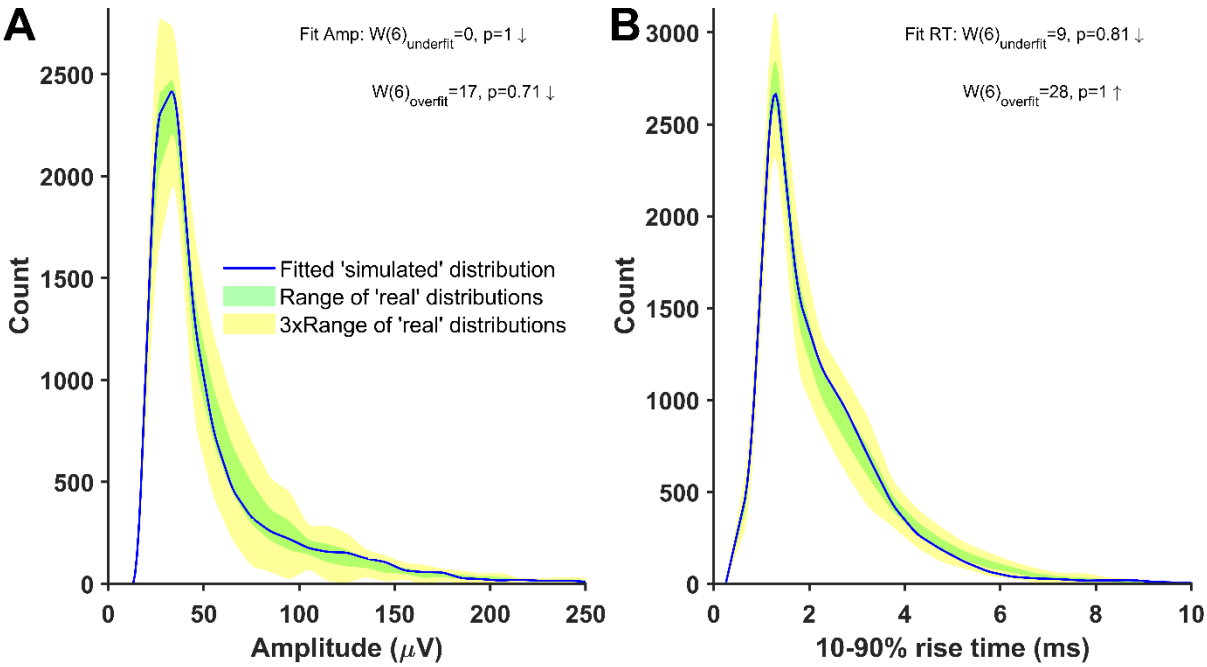

Supplementary Figure 19: Cell p120b (layer 2/3), distributions of mini-like events detected in a 'noise with simulated minis' voltage trace that closely matched 'noise with real minis' recordings. Parameters of simulated minis controlled by GA. Down arrow: 'simulated' SAD < 'real' SAD (up: 'simulated' > 'real'; Suppl. Fig. 15).

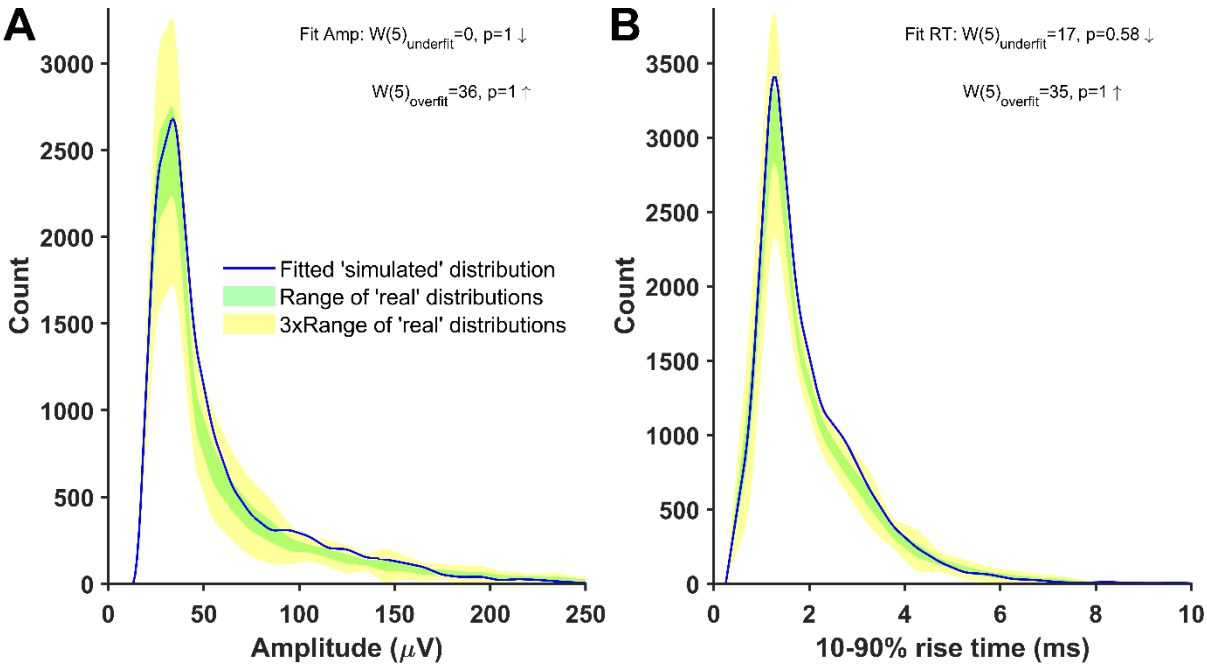

Supplementary Figure 20: Cell p122a (layer 2/3), distributions of mini-like events detected in a 'noise with simulated minis' voltage trace that closely matched 'noise with real minis' recordings. Parameters of simulated minis controlled by GA. Down arrow: 'simulated' SAD < 'real' SAD (up: 'simulated' > 'real'; Suppl. Fig. 15).

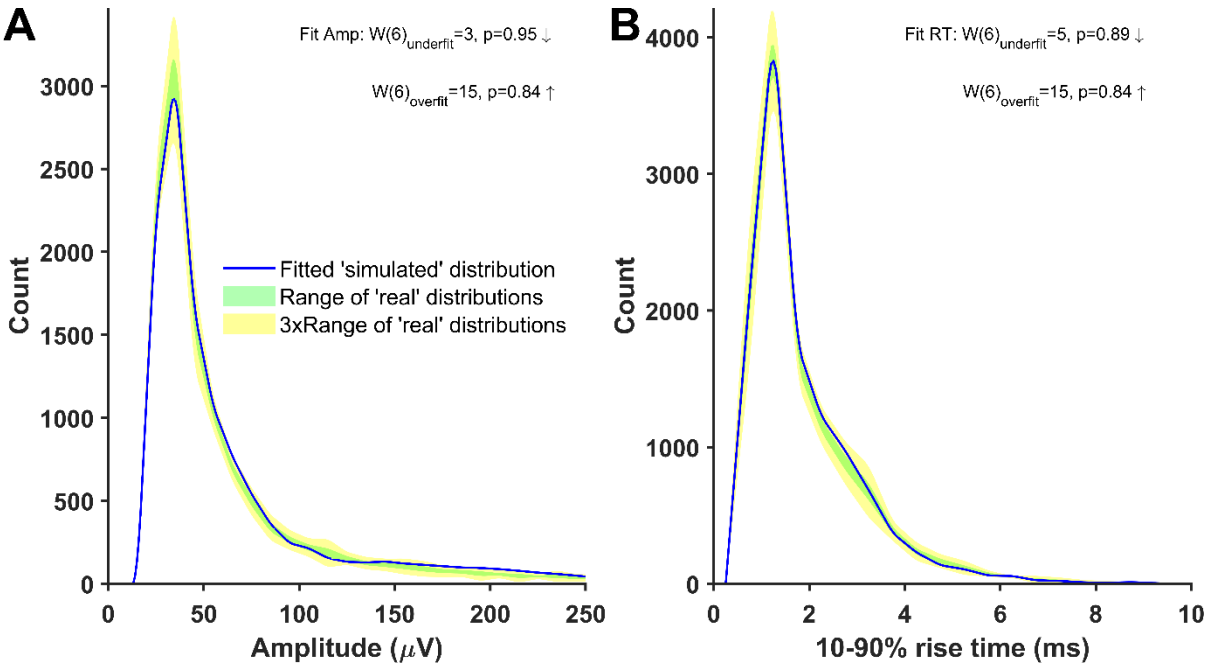

Supplementary Figure 21: Cell p124b (layer 5), distributions of mini-like events detected in a ’noise with simulated minis’ voltage trace that closely matched ‘noise with real minis‘ recordings. Parameters of simulated minis controlled by GA. Down arrow: ‘simulated’ SAD < ‘real’ SAD (up: ‘simulated’ > ‘real’; Suppl. Fig. 15).

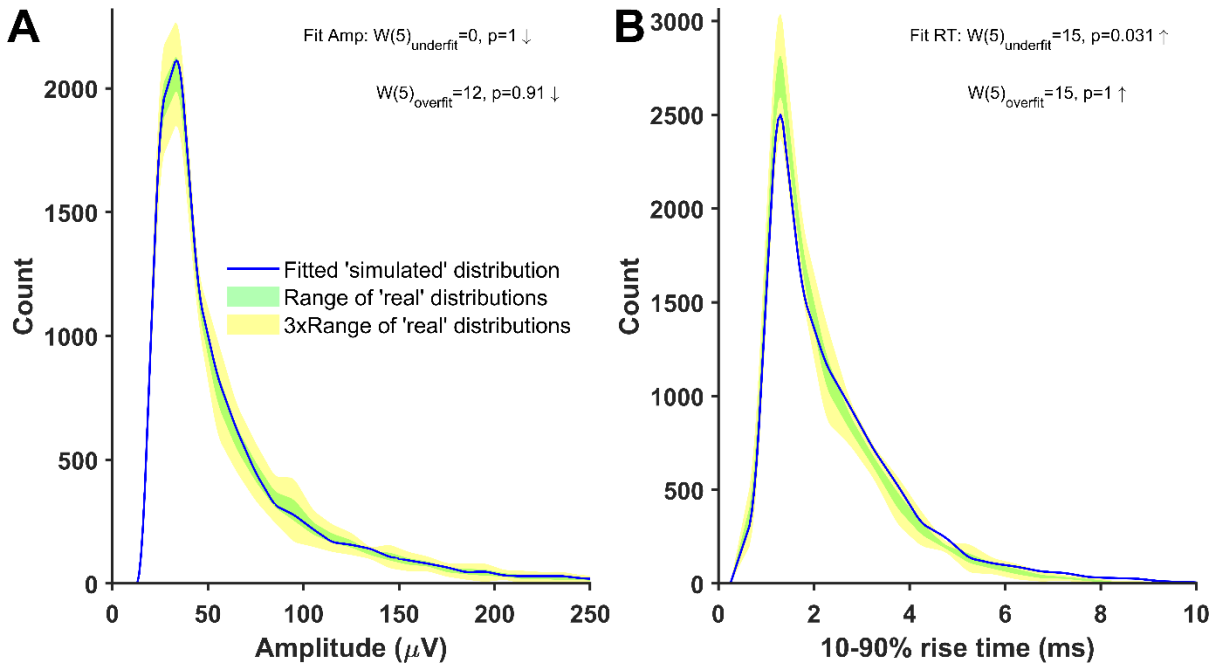

Supplementary Figure 22: Cell p125a (layer 2/3), distributions of mini-like events detected in a 'noise with simulated minis' voltage trace that closely matched 'noise with real minis' recordings. Parameters of simulated minis controlled by GA. Down arrow: 'simulated' SAD < 'real' SAD (up: 'simulated' > 'real'; Suppl. Fig. 15).

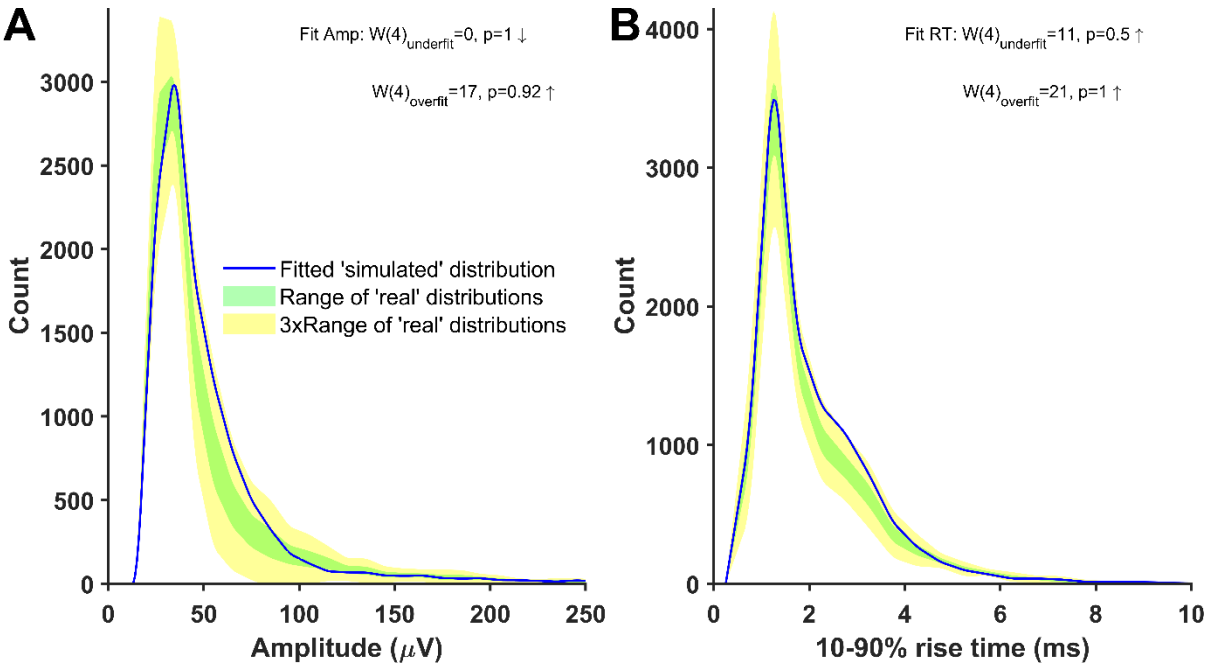

Supplementary Figure 23: Cell p127c (layer 2/3), distributions of mini-like events detected in a 'noise with simulated minis' voltage trace that closely matched 'noise with real minis' recordings. Parameters of simulated minis controlled by GA. Down arrow: 'simulated' SAD < 'real' SAD (up: 'simulated' > 'real'; Suppl. Fig. 15).

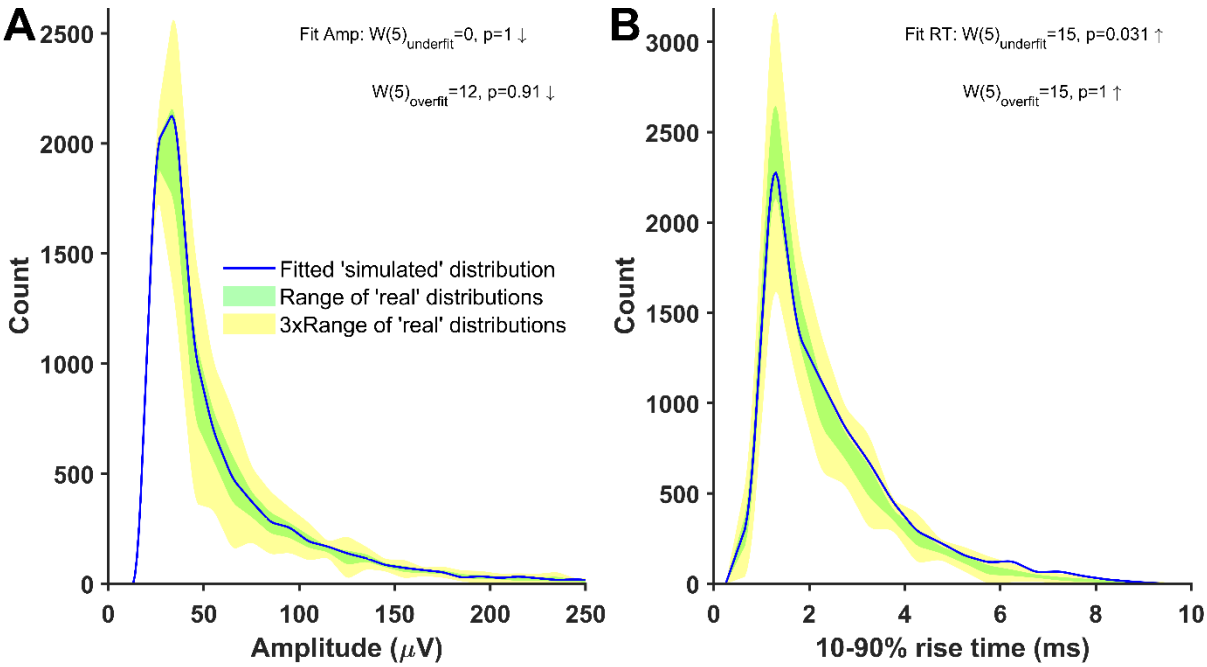

Supplementary Figure 24: Cell p128c (layer 2/3), distributions of mini-like events detected in a 'noise with simulated minis' voltage trace that closely matched 'noise with real minis' recordings. Parameters of simulated minis controlled by GA. Down arrow: 'simulated' SAD < 'real' SAD (up: 'simulated' > 'real'; Suppl. Fig. 15).

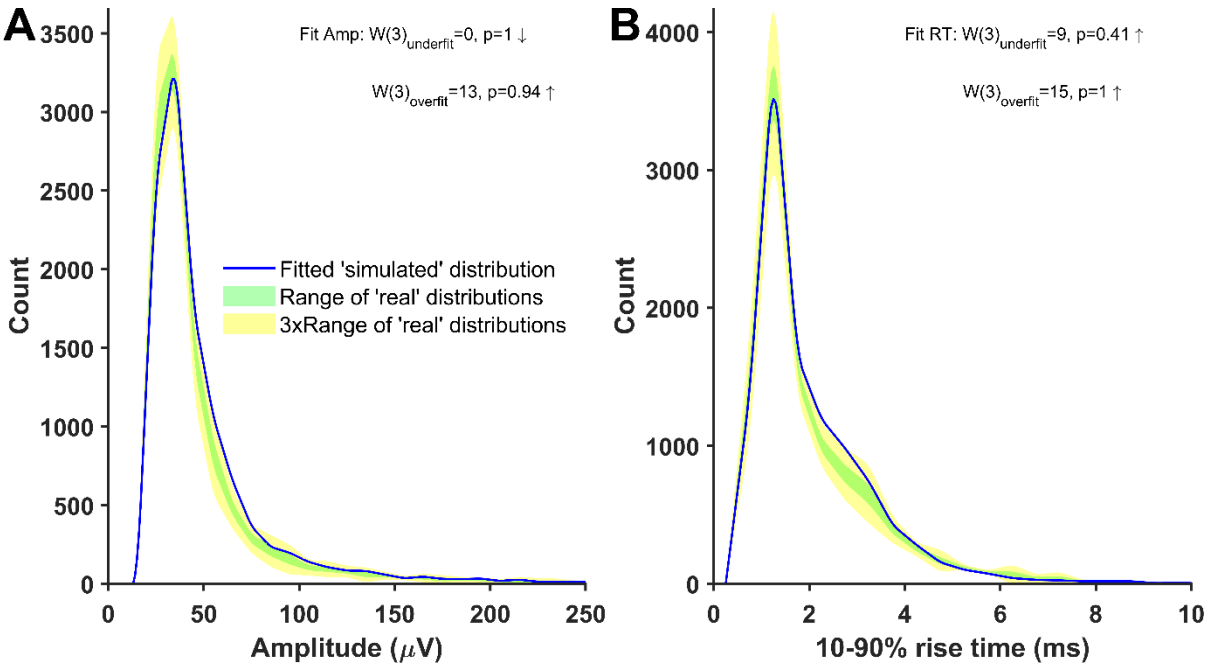

Supplementary Figure 25: Cell p129a (layer 5), distributions of mini-like events detected in a ’noise with simulated minis’ voltage trace that closely matched ‘noise with real minis‘ recordings. Parameters of simulated minis controlled by GA. Down arrow: ‘simulated’ SAD < ‘real’ SAD (up: ‘simulated’ > ‘real’; Suppl. Fig. 15).

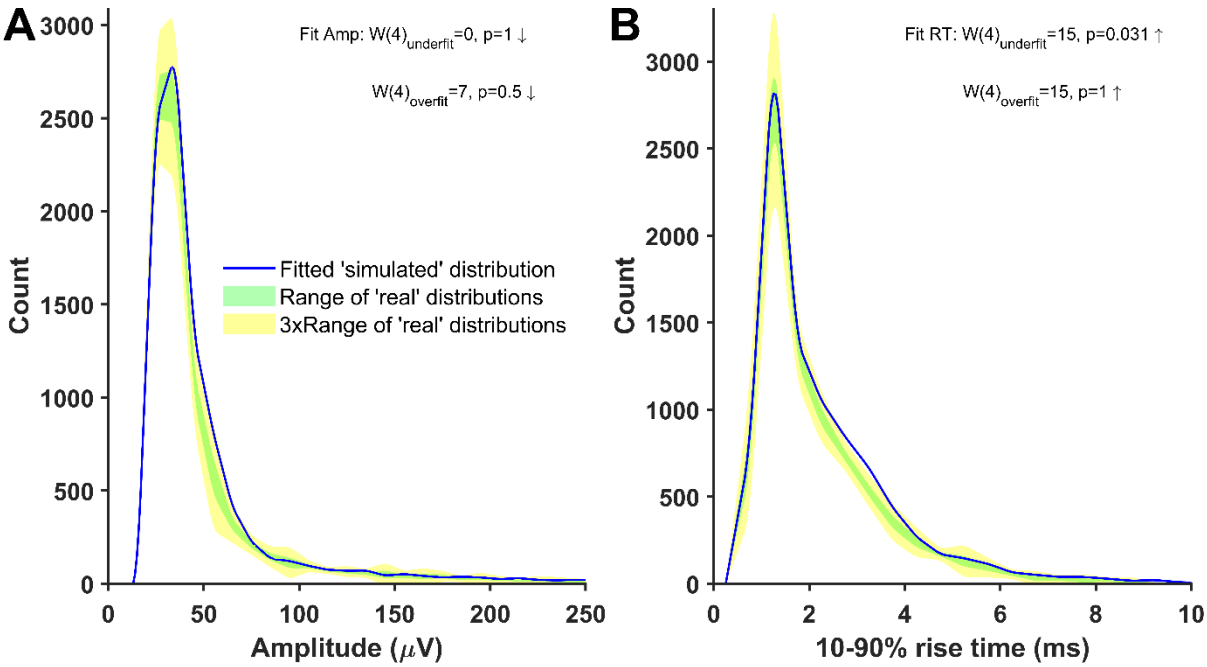

Supplementary Figure 26: Cell p131a (layer 2/3), distributions of mini-like events detected in a 'noise with simulated minis' voltage trace that closely matched 'noise with real minis' recordings. Parameters of simulated minis controlled by GA. Down arrow: 'simulated' SAD < 'real' SAD (up: 'simulated' > 'real'; Suppl. Fig. 15).

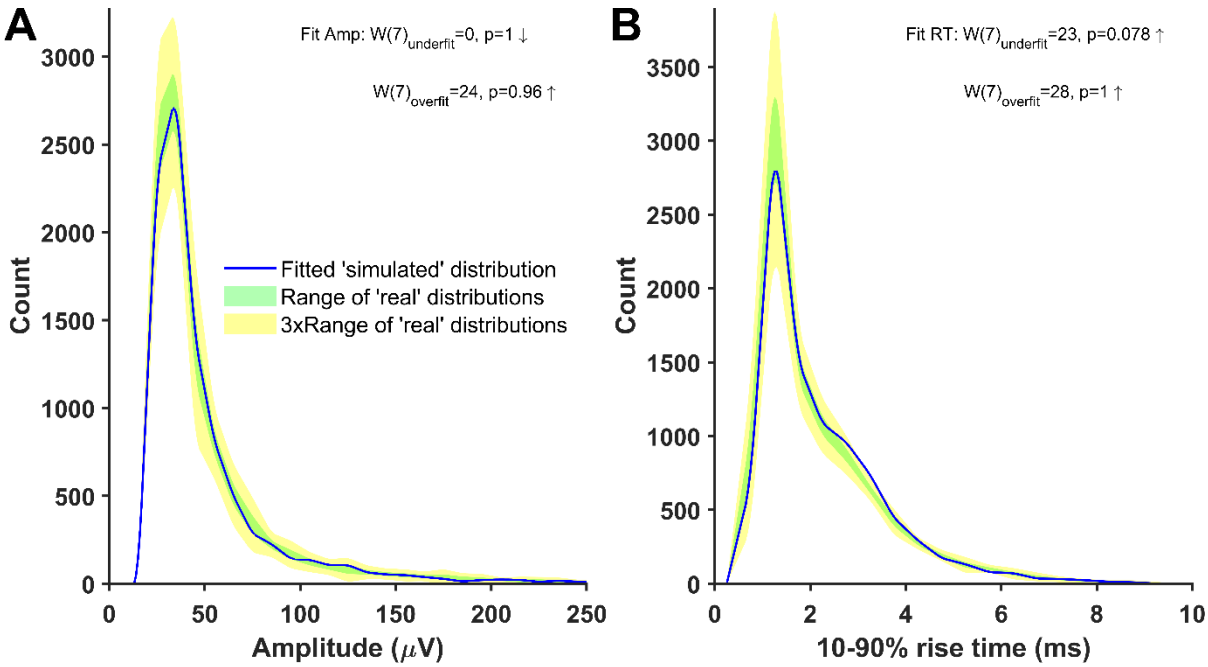

Supplementary Figure 27: Cell p131c (layer 2/3), distributions of mini-like events detected in a 'noise with simulated minis' voltage trace that closely matched 'noise with real minis' recordings. Parameters of simulated minis controlled by GA. Down arrow: 'simulated' SAD < 'real' SAD (up: 'simulated' > 'real'; Suppl. Fig. 15).

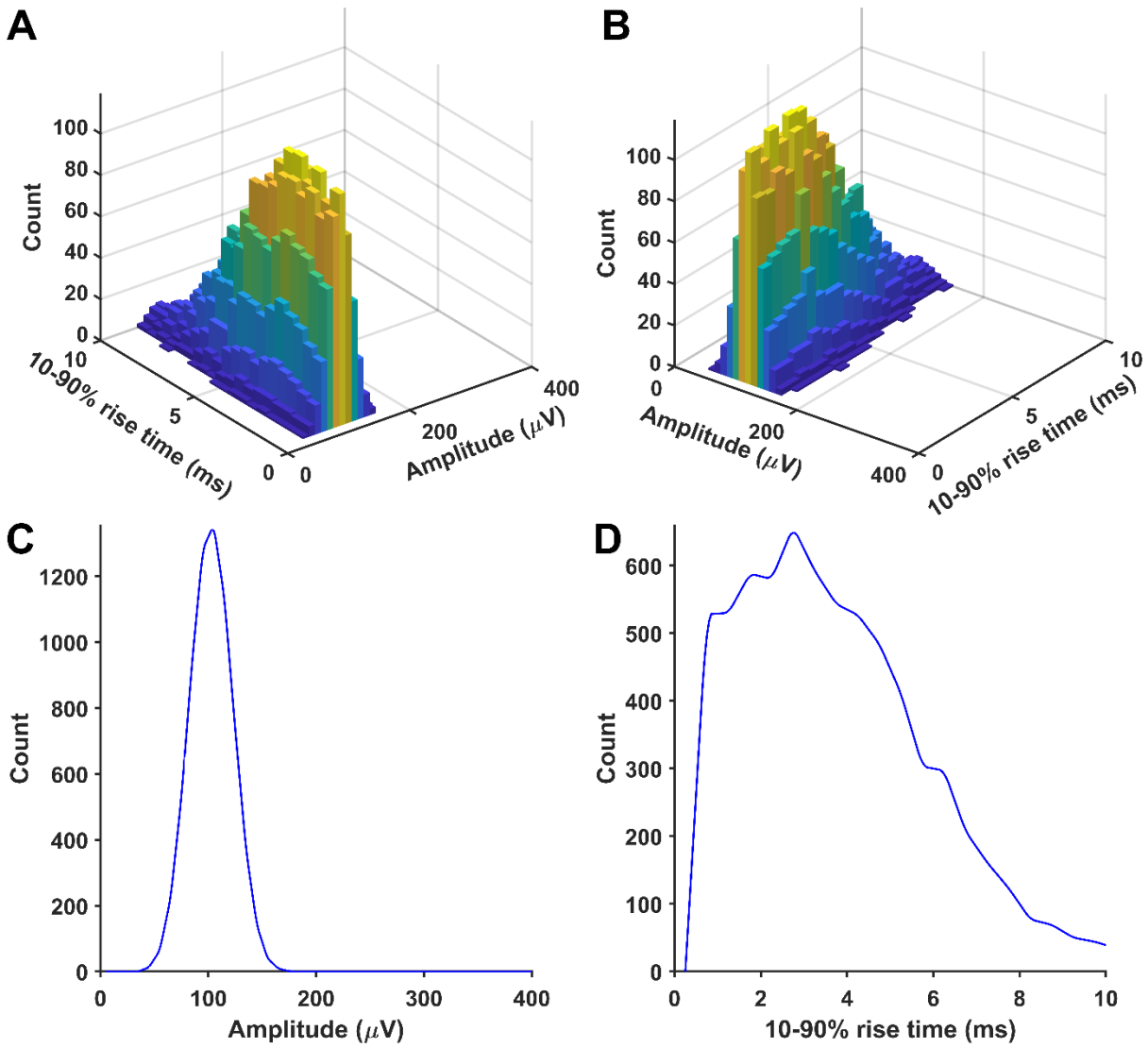

Supplementary Figure 28: An example of a distribution of randomly selected simulated minis that was used to produce a close match between distributions of mini-like events detected in a 'noise with simulated minis' voltage trace (40 µV lower limit on simulated amplitudes) and a 'noise with real minis' recording for cell p103a (layer 5).

(A) and (B) Joint amplitude and 10-90% rise time distribution of simulated minis (two views).

(C) 'Marginal' amplitude and (D) 10-90% rise time distributions (all 2-D bins projected onto that axis).

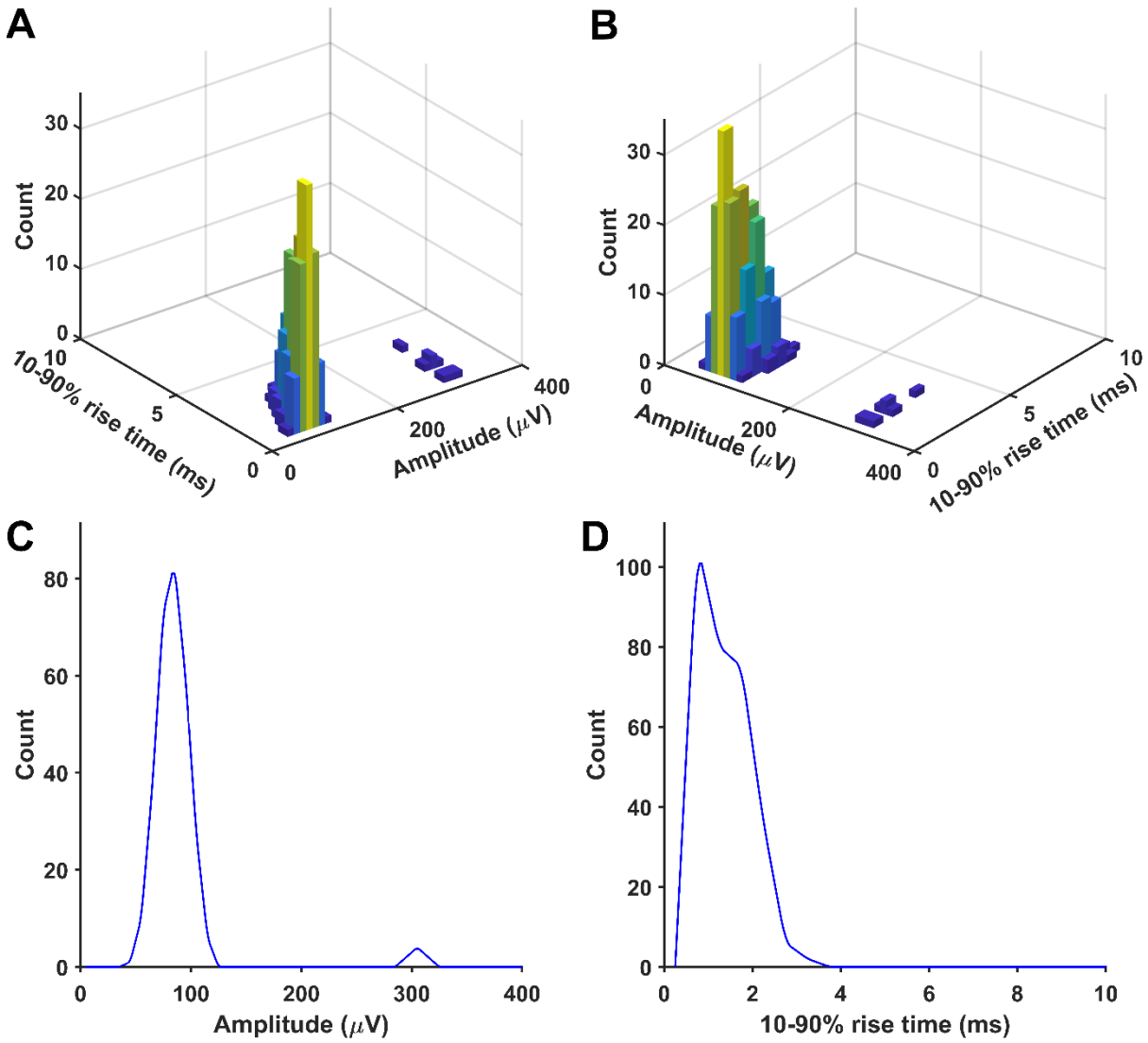

1336

1337 **Supplementary Figure 29:** An example of a distribution of randomly selected simulated minis that

1338 was used to produce a close match between distributions of mini-like events detected in a 'noise

1339 with simulated minis' voltage trace (40 µV lower limit on simulated amplitudes) and a 'noise with

1340 real minis' recording for cell p106b (layer 5).

1341 Panels as for Supplementary Figure 28.

1342

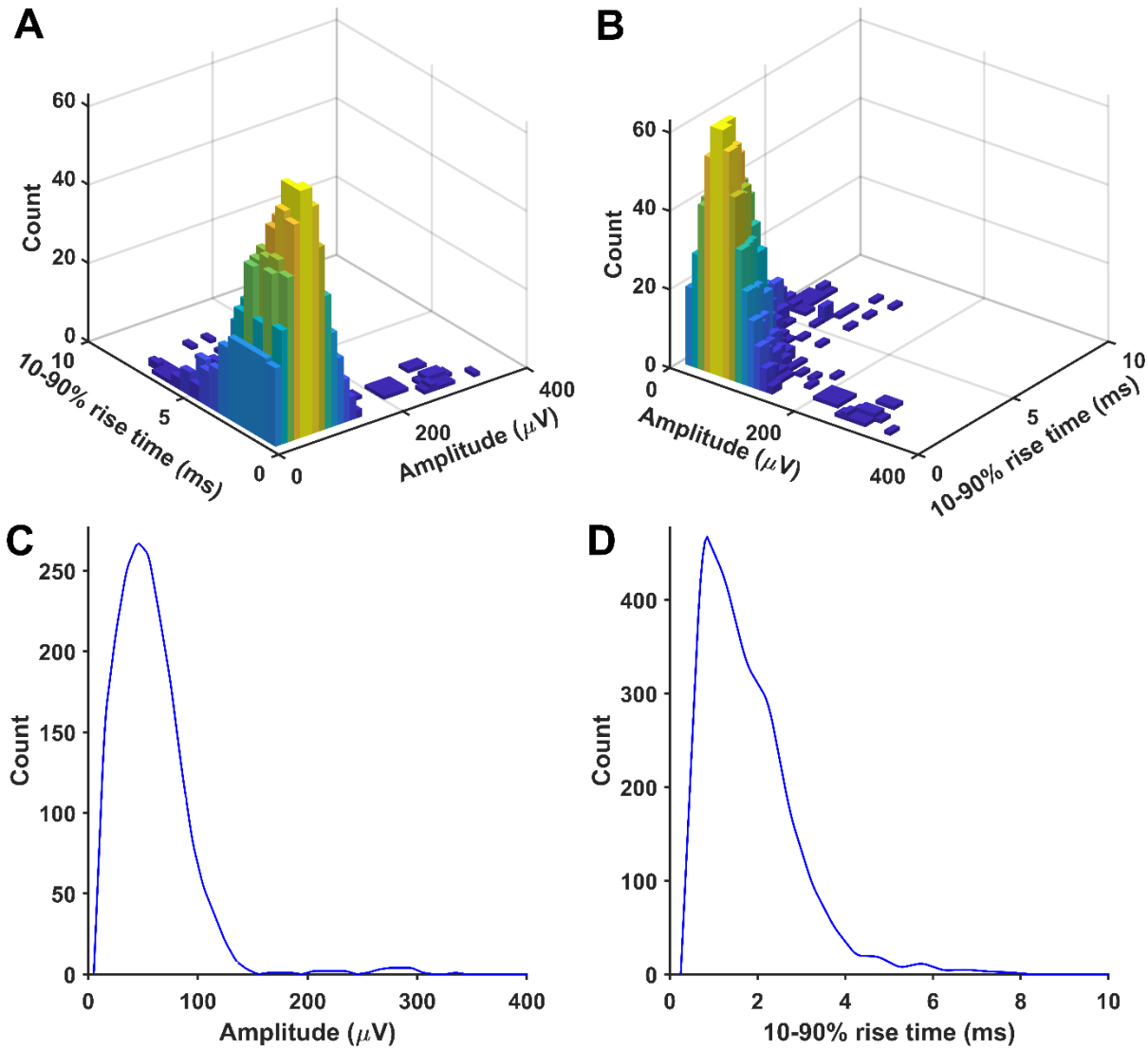

1343

1344 **Supplementary Figure 30:** An example of a distribution of randomly selected simulated minis that

1345 was used to produce a close match between distributions of mini-like events detected in a 'noise

1346 with simulated minis' voltage trace (10 µV lower limit on simulated amplitudes) and a 'noise with

1347 real minis' recording for cell p108a (layer 5).

1348 Panels as for Supplementary Figure 28.

1349

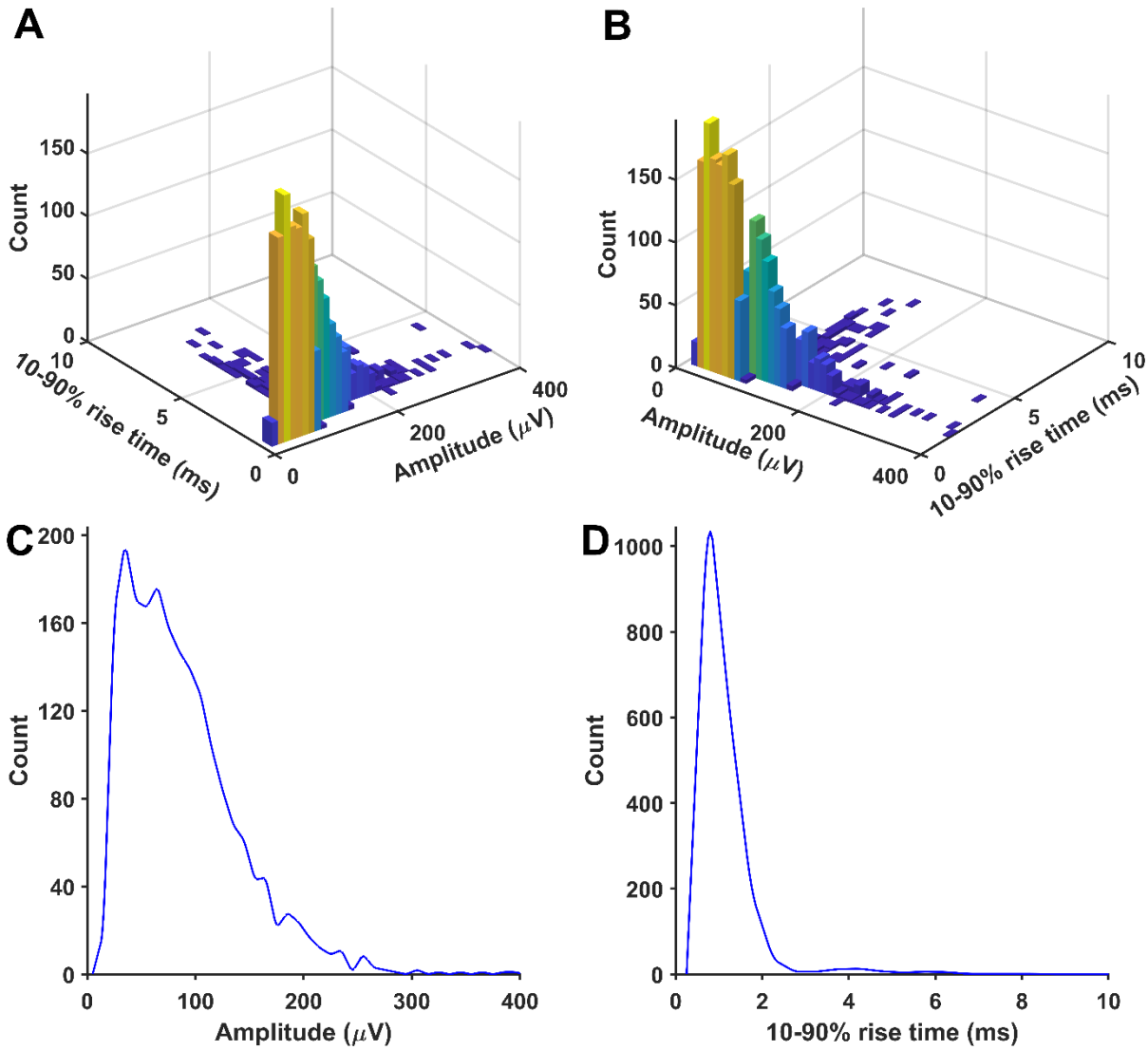

Supplementary Figure 31: An example of a distribution of randomly selected simulated minis that was used to produce a close match between distributions of mini-like events detected in a 'noise with simulated minis' voltage trace (10 µV lower limit on simulated amplitudes) and a 'noise with real minis' recording for cell p108b (layer 5).

Panels as for Supplementary Figure 28.

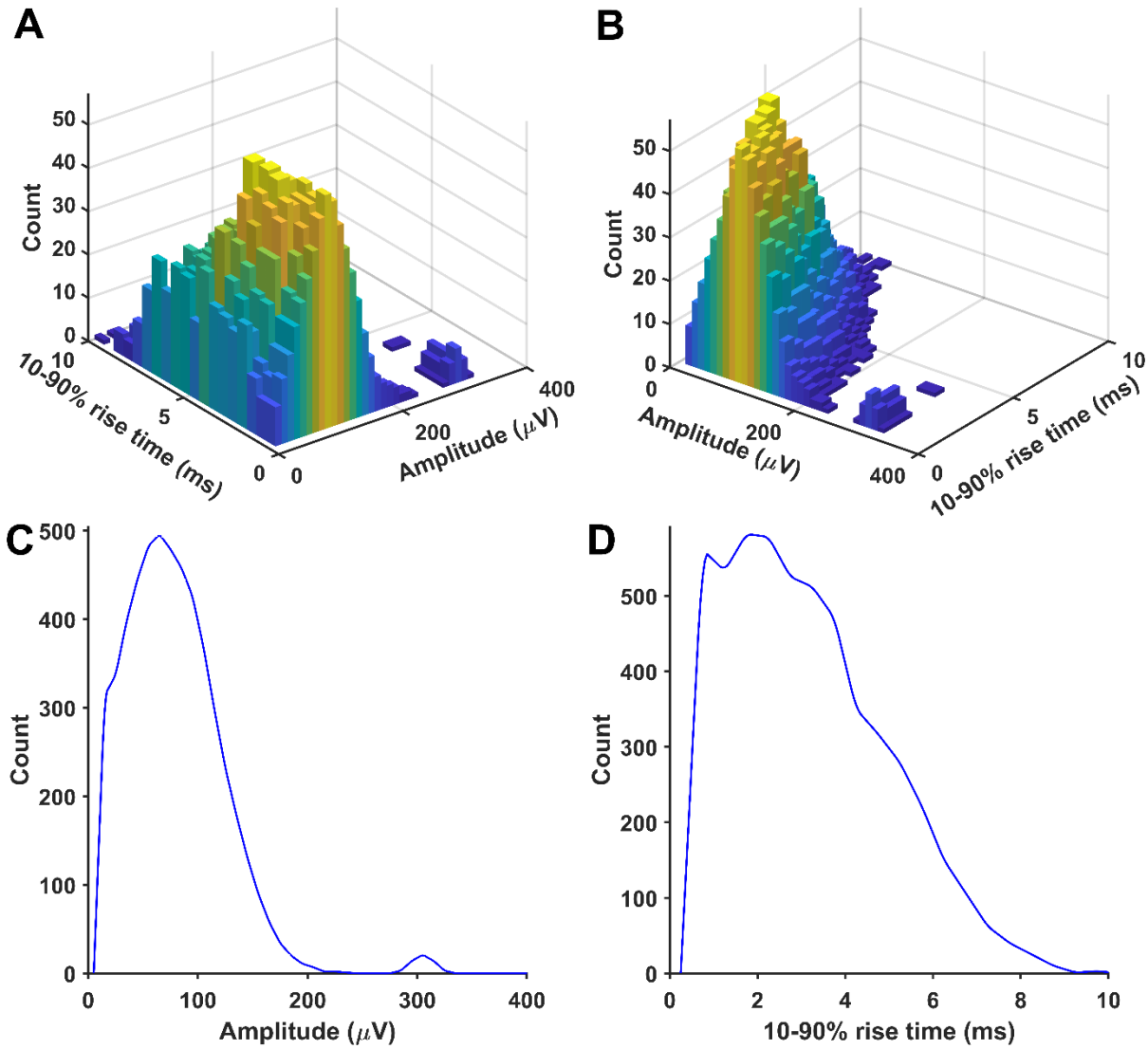

Supplementary Figure 32: An example of a distribution of randomly selected simulated minis that was used to produce a close match between distributions of mini-like events detected in a 'noise with simulated minis' voltage trace (10 µV lower limit on simulated amplitudes) and a 'noise with real minis' recording for cell p108c (layer 5).

Panels as for Supplementary Figure 28.

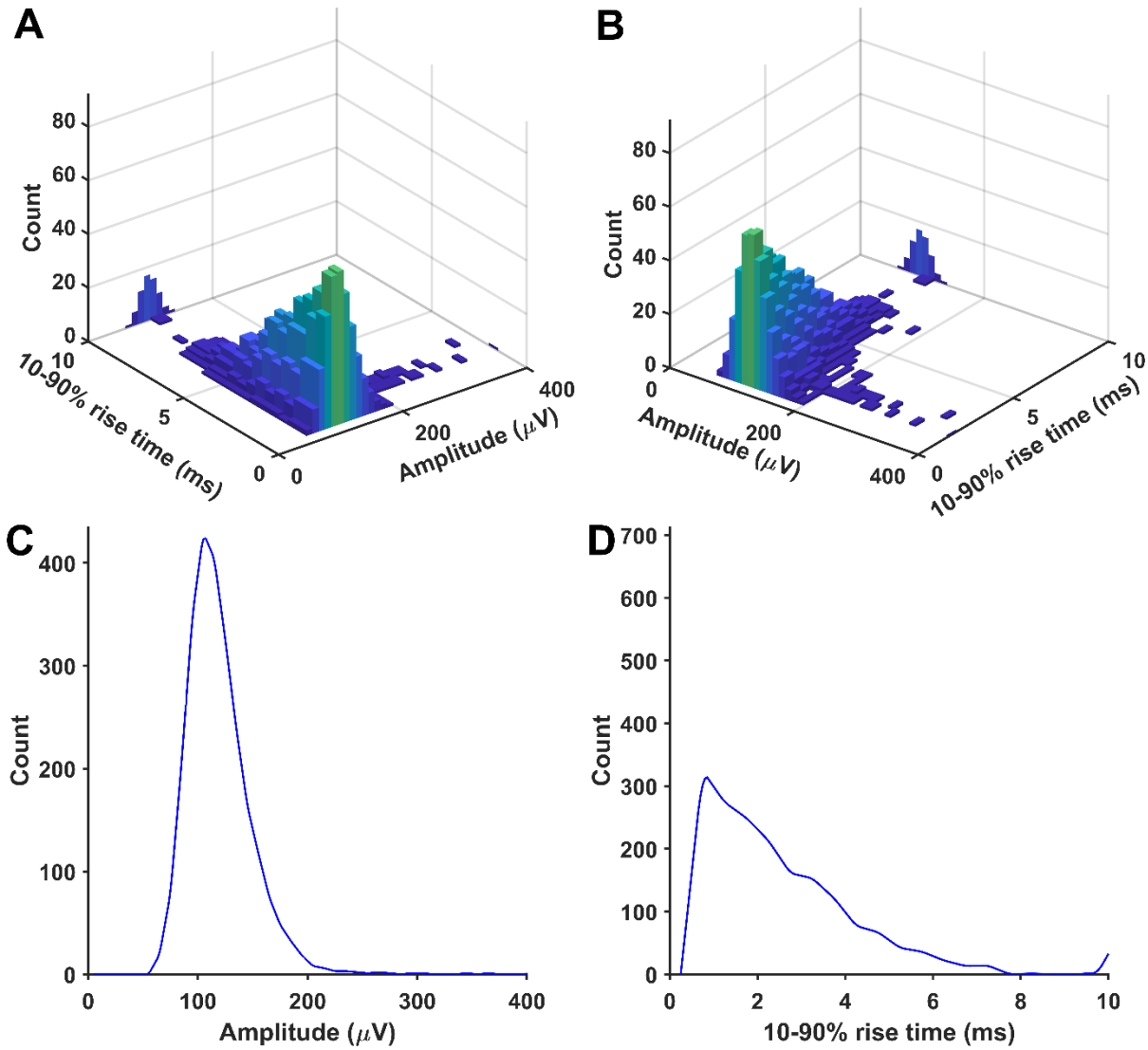

Supplementary Figure 33: An example of a distribution of randomly selected simulated minis that was used to produce a close match between distributions of mini-like events detected in a 'noise with simulated minis' voltage trace (60 µV lower limit on simulated amplitudes) and a 'noise with real minis' recording for cell p120b (layer 2/3).

Panels as for Supplementary Figure 28.

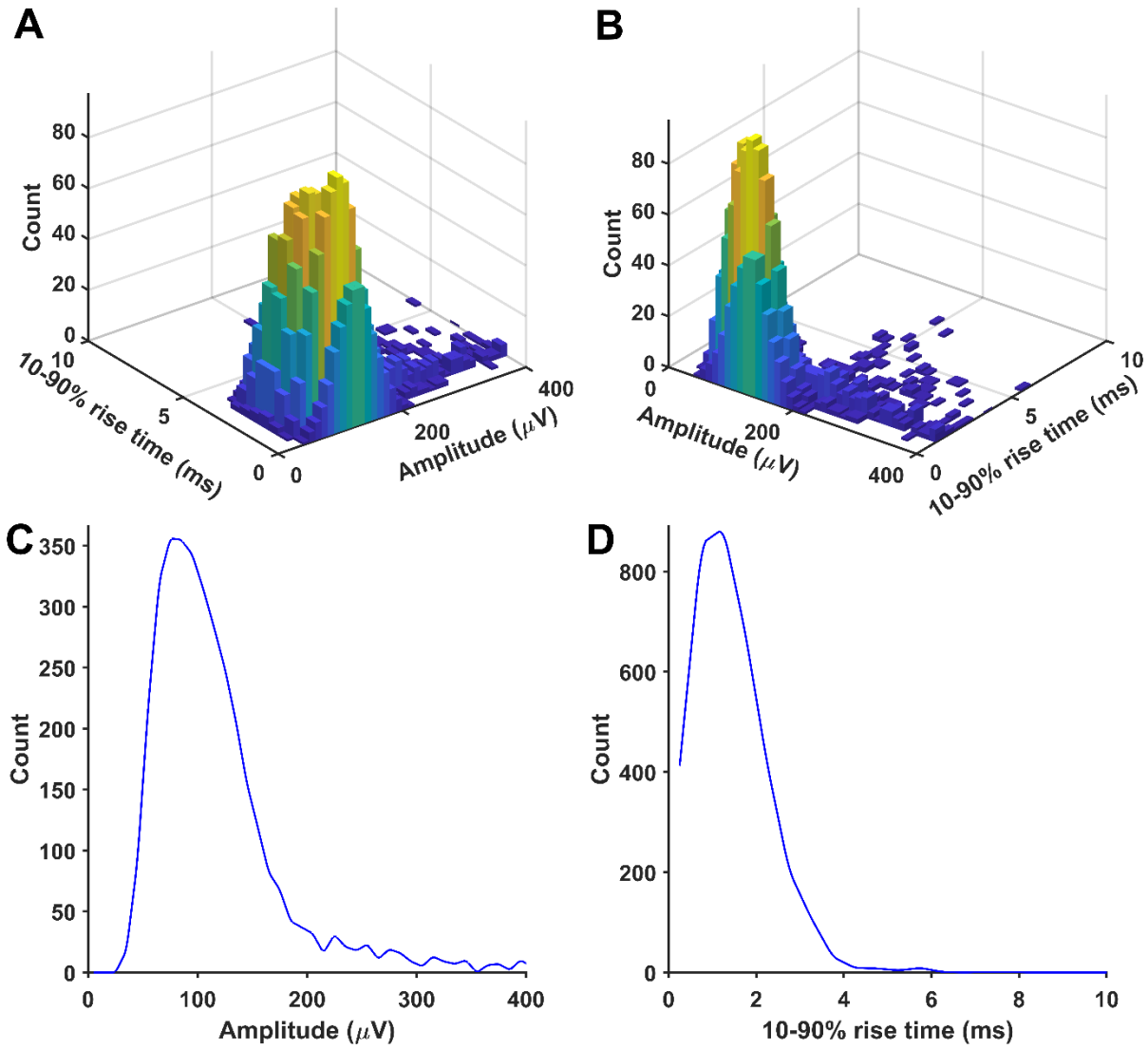

Supplementary Figure 34: An example of a distribution of randomly selected simulated minis that was used to produce a close match between distributions of mini-like events detected in a 'noise with simulated minis' voltage trace (30 µV lower limit on simulated amplitudes) and a 'noise with real minis' recording for cell p122a (layer 2/3).

Panels as for Supplementary Figure 28.

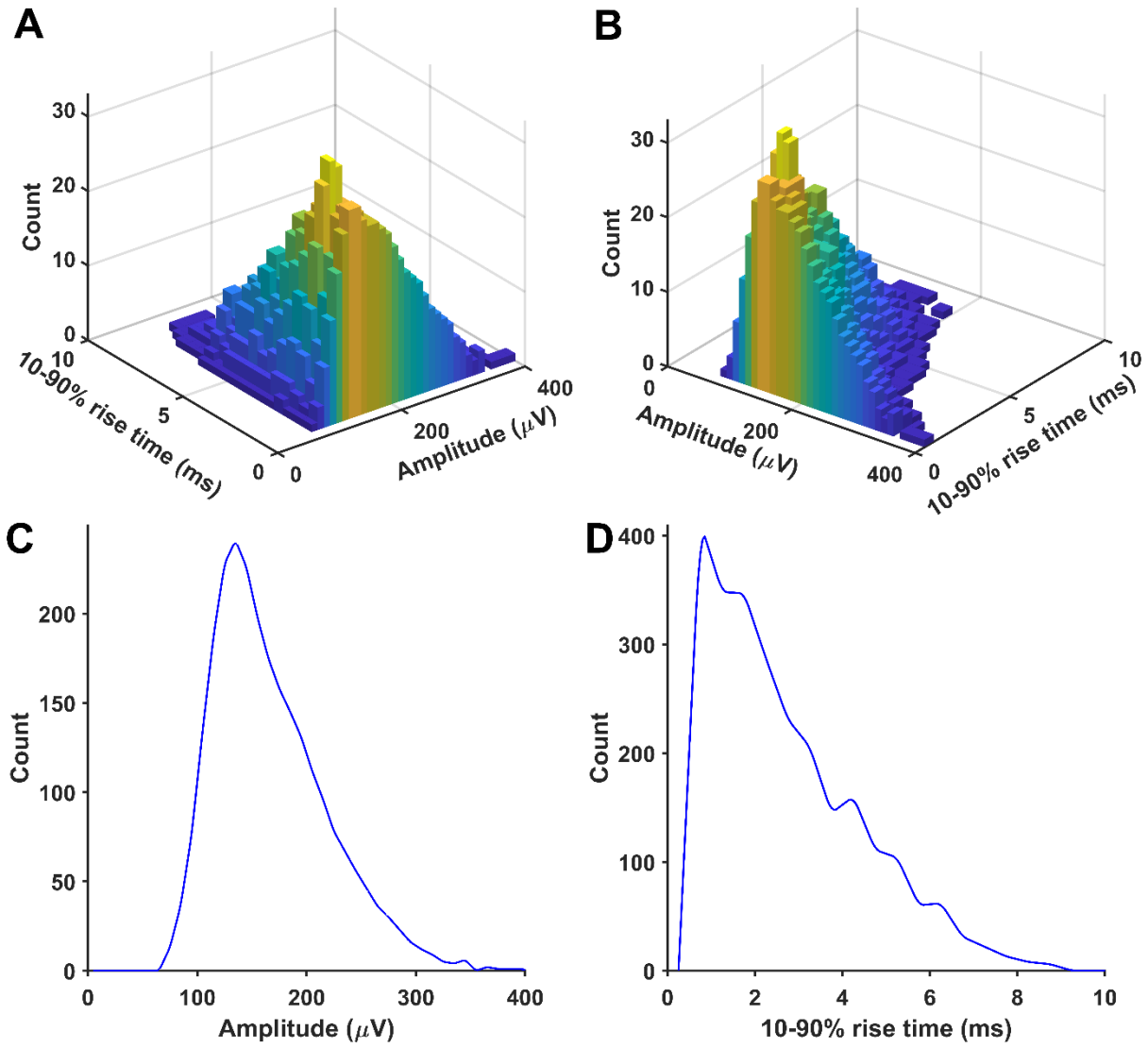

Supplementary Figure 35: An example of a distribution of randomly selected simulated minis that was used to produce a close match between distributions of mini-like events detected in a 'noise with simulated minis' voltage trace (40 µV lower limit on simulated amplitudes) and a 'noise with real minis' recording for cell p124b (layer 5).

Panels as for Supplementary Figure 28.

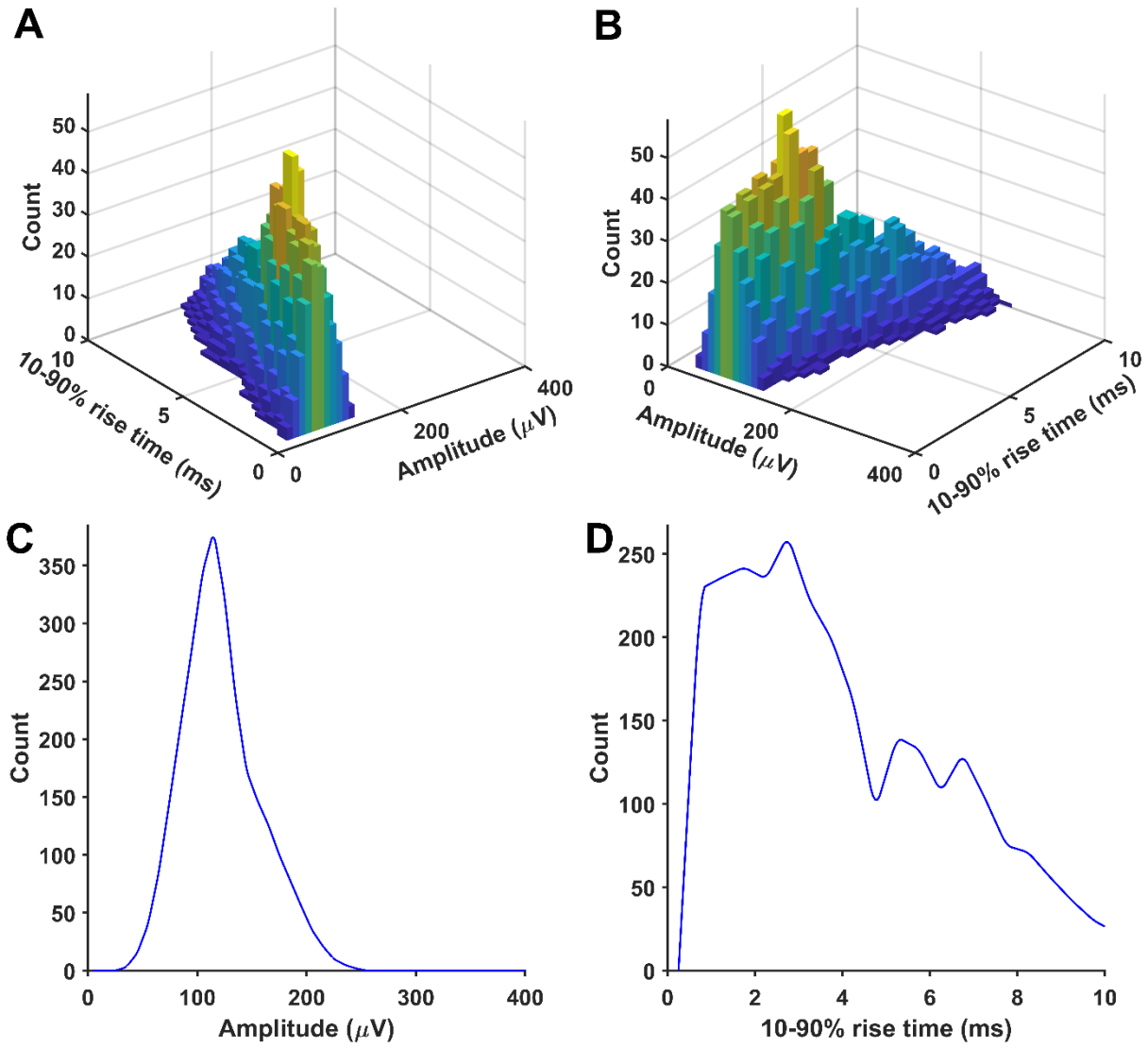

Supplementary Figure 36: An example of a distribution of randomly selected simulated minis that was used to produce a close match between distributions of mini-like events detected in a 'noise with simulated minis' voltage trace (30 µV lower limit on simulated amplitudes) and a 'noise with real minis' recording for cell p125a (layer 2/3).

Panels as for Supplementary Figure 28.

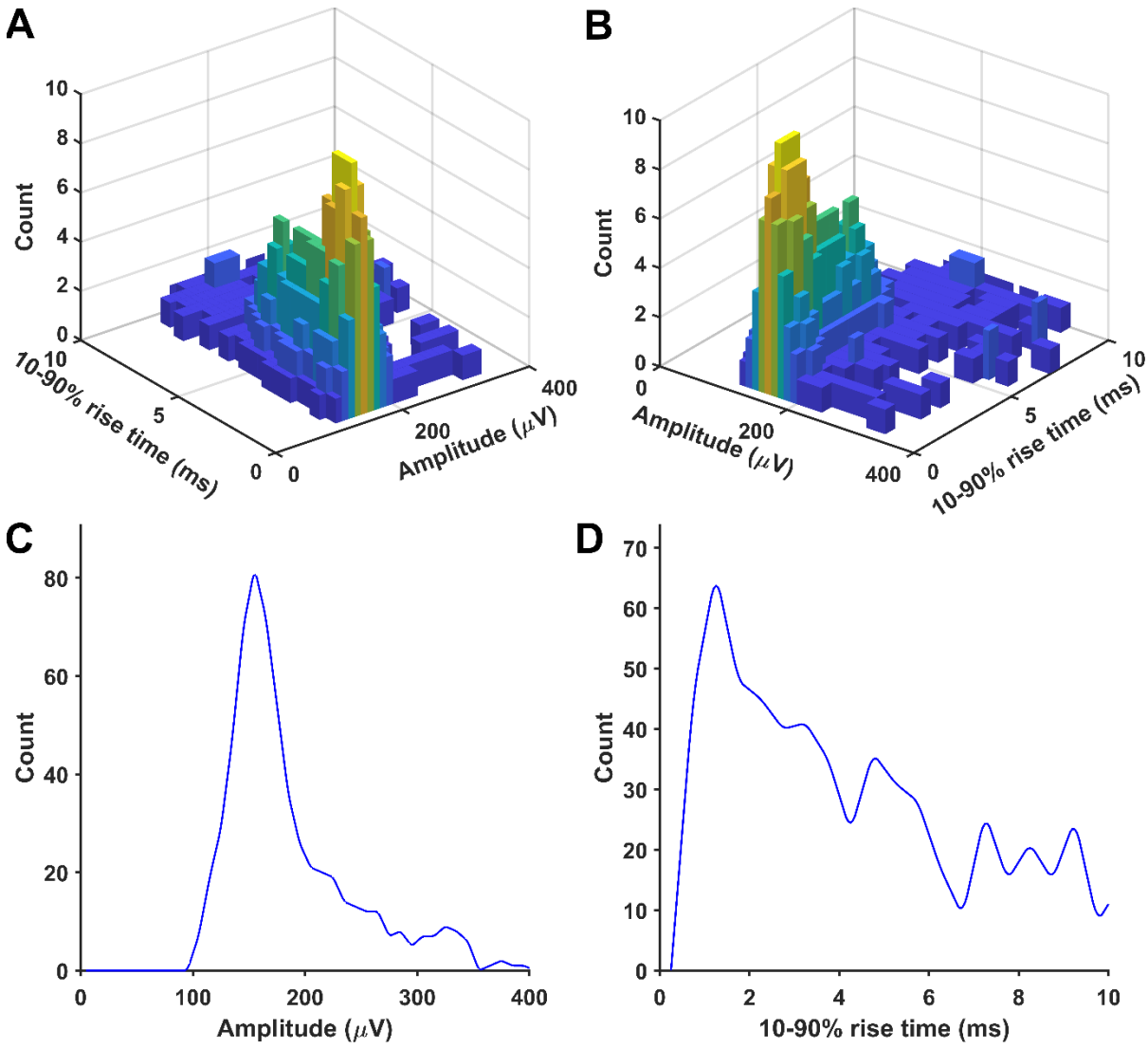

Supplementary Figure 37: An example of a distribution of randomly selected simulated minis that was used to produce a close match between distributions of mini-like events detected in a 'noise with simulated minis' voltage trace (100 µV lower limit on simulated amplitudes) and a 'noise with real minis' recording for cell p127c (layer 2/3).

Panels as for Supplementary Figure 28.

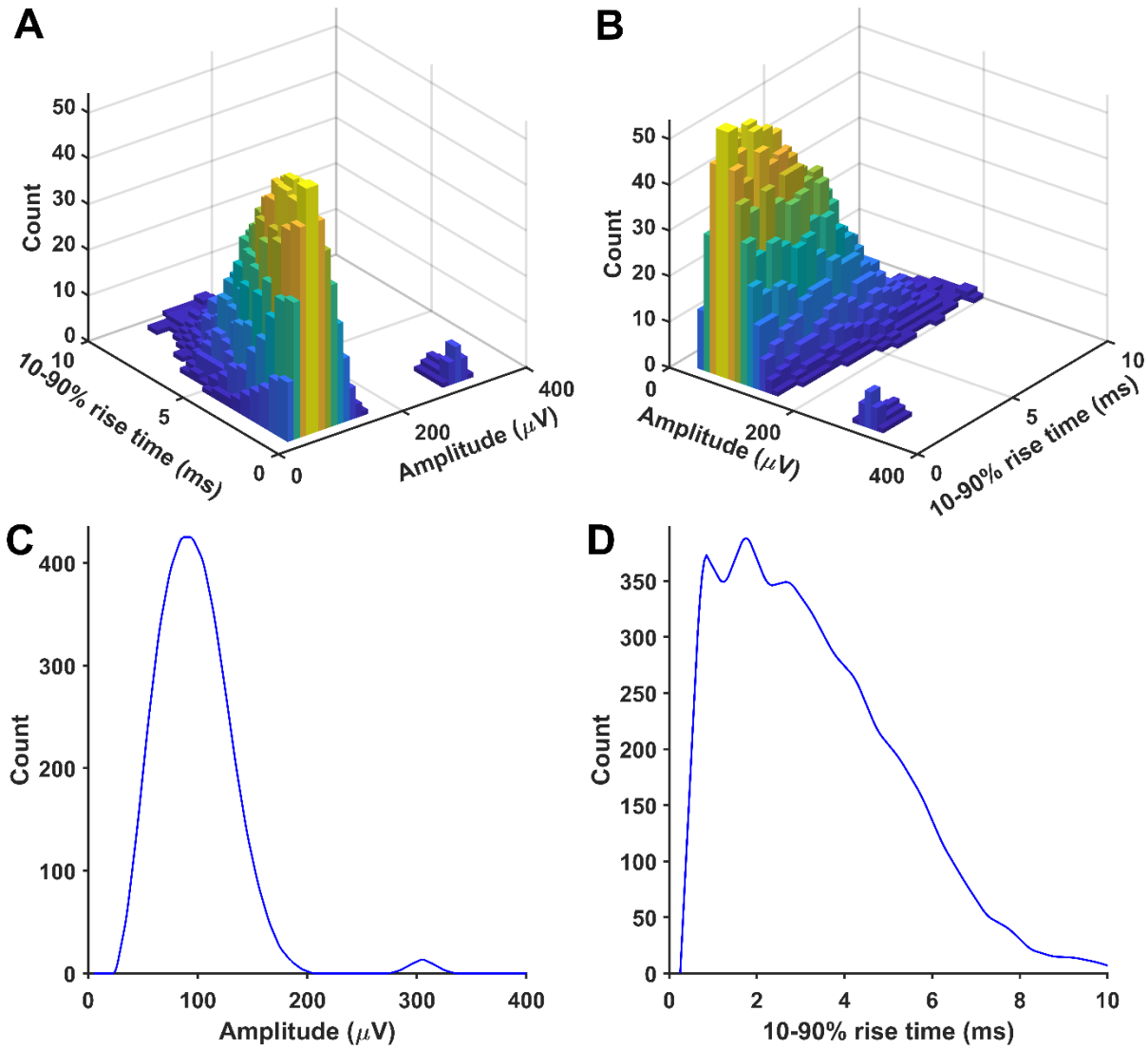

Supplementary Figure 38: An example of a distribution of randomly selected simulated minis that was used to produce a close match between distributions of mini-like events detected in a 'noise with simulated minis' voltage trace (30 µV lower limit on simulated amplitudes) and a 'noise with real minis' recording for cell p128c (layer 2/3).

Panels as for Supplementary Figure 28.

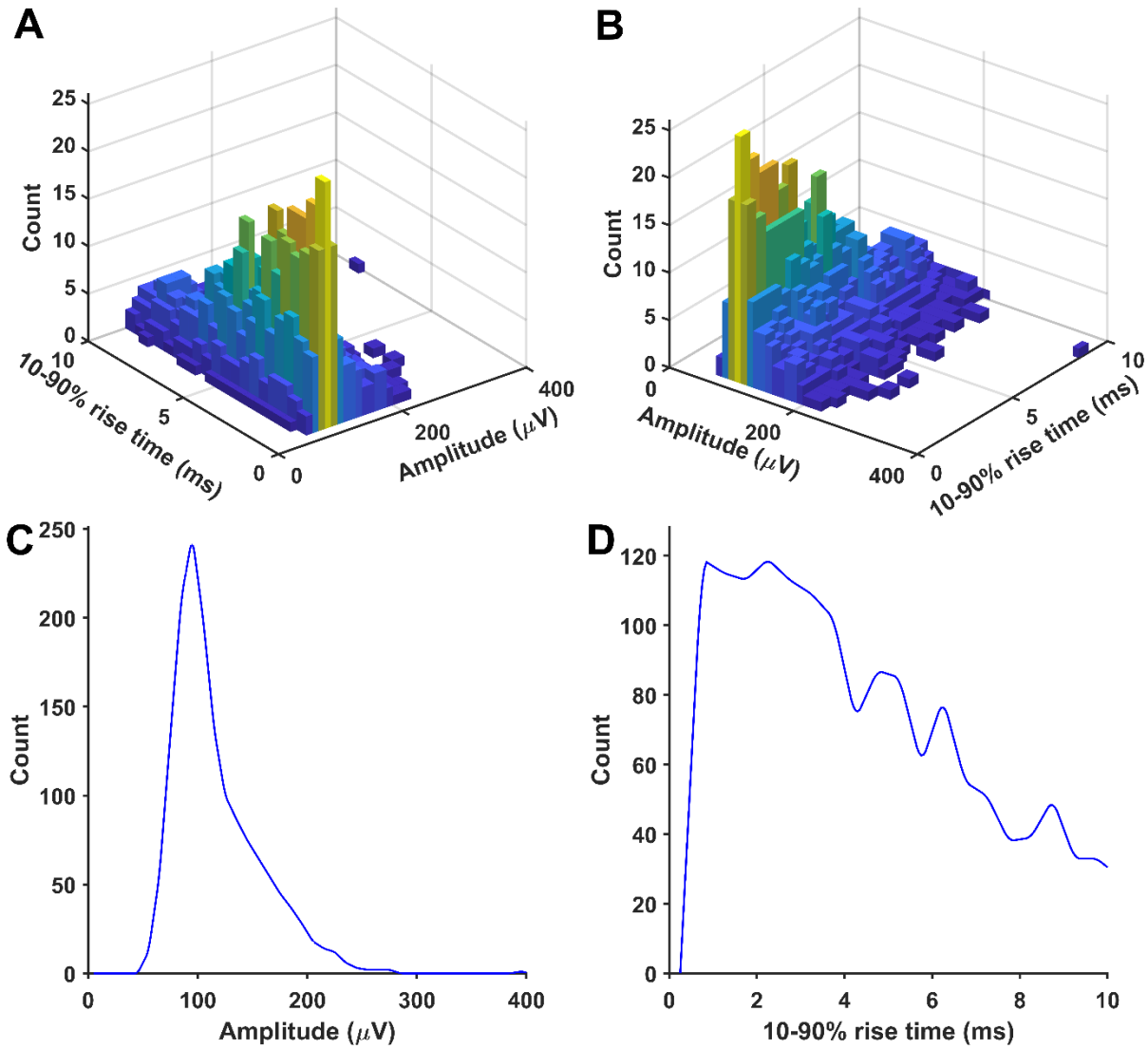

Supplementary Figure 39: An example of a distribution of randomly selected simulated minis that was used to produce a close match between distributions of mini-like events detected in a 'noise with simulated minis' voltage trace (50 µV lower limit on simulated amplitudes) and a 'noise with real minis' recording for cell p129a (layer 5).

Panels as for Supplementary Figure 28.

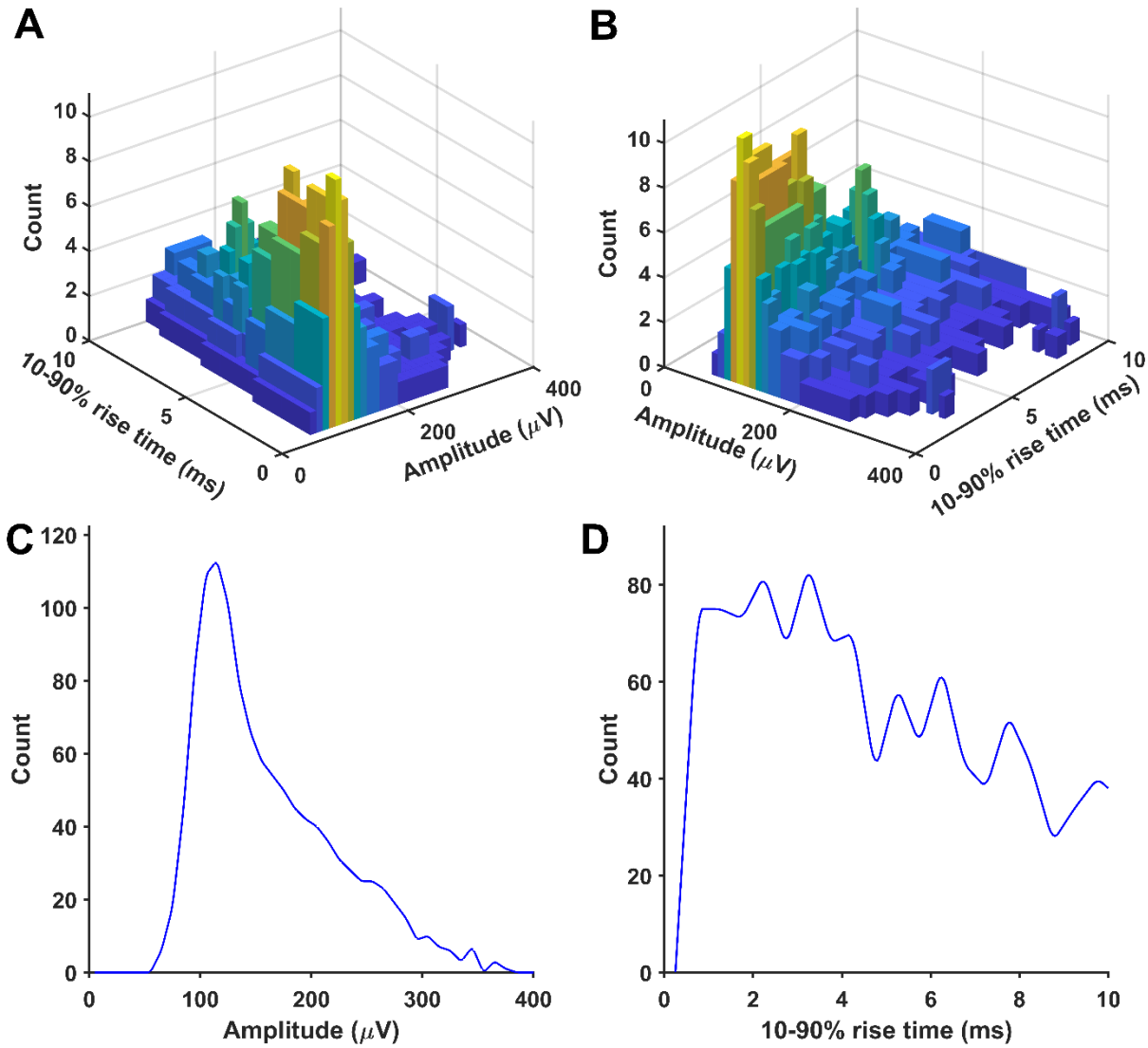

Supplementary Figure 40: An example of a distribution of randomly selected simulated minis that was used to produce a close match between distributions of mini-like events detected in a 'noise with simulated minis' voltage trace (60 µV lower limit on simulated amplitudes) and a 'noise with real minis' recording for cell p131a (layer 2/3).

Panels as for Supplementary Figure 28.